AUTOMATED AND INTEGRATED MICROSYSTEMS FOR HIGH-THROUGHPUT AND HIGH-RESOLUTION IMAGING, SORTING, AND LASER ABLATION OF *C. ELEGANS*

A Dissertation
Presented to
The Academic Faculty

by

Kwanghun Chung

In Partial Fulfillment
of the Requirements for the Degree
Doctor of Philosophy in the
School of Chemical & Biomolecular Engineering

Georgia Institute of Technology
December 2009

AUTOMATED AND INTEGRATED MICROSYSTEMS FOR HIGH-THROUGHPUT AND HIGH-RESOLUTION IMAGING, SORTING, AND LASER ABLATION OF *C. ELEGANS*

Approved by:

Dr. Hang Lu, Advisor
School of Chemical & Biomolecular Engineering
Georgia Institute of Technology

Dr. Mark Prausnitz
School of Chemical & Biomolecular Engineering
Georgia Institute of Technology

Dr. Victor Breedveld
School of Chemical & Biomolecular Engineering
Georgia Institute of Technology

Dr. Todd Streelman
School of Biology
Georgia Institute of Technology

Dr. Dennis Hess
School of Chemical & Biomolecular Engineering
Georgia Institute of Technology

Date Approved: July 30, 2009

To my parents

ACKNOWLEDGEMENTS

First, I would like to thank my advisor Prof. Hang Lu for her advice, mentoring, and dedication. She always encouraged me to think independently and provided valuable guidance throughout my doctoral studies. This work would not have been possible without her support. I would further like to thank my thesis committee members: Prof. Breedveld, Prof. Hess, Prof. Prausnitz, and Prof. Streelman, for reviewing my work and providing constructive feedback.

I would like to thank all the members of the Dr. Lu's group. They have helped me in so many ways. Specifically, I express my gratitude toward Matthew Crane, Hyewon Lee, Jeffrey Stirman, and Edward Park who I worked with on the projects in this dissertation. I am also thankful to Jaekyu Cho in Dr. Victor Breedveld's group for his contribution on the temperature measurement experiment.

I would like to recognize my parents and brother. My family has made my academic pursuits possible. I am forever indebted to my parents for their unconditional love, sacrifices, and constant encouragement. I also want to acknowledge my friends in both the U.S. and South Korea, who made my life in Atlanta very memorable.

Finally, I am thankful to the School of Chemical & Biomolecular Engineering for providing an excellent infrastructure and research environment.

TABLE OF CONTENTS

LIST OF TABLES

LIST OF FIGURES

SUMMARY

The objective of this research is to develop automated and integrated microsystems for high-resolution imaging and high-throughput phenotyping / laser ablation of *C. elegans*. These microsystems take advantage of microfluidic technology for precisely handling animals and computer-aid automation for high-throughput processing. We demonstrated automated and high-throughput imaging / sorting and laser ablation of *C. elegans.* This thesis work is divided into four parts: development of a microsystem for imaging and sorting, development of a microsystem for laser cell ablation, development of a novel temperature measurement method, and development of pressure measurement method in microchannels.

First, a microsystem was developed for high-throughput microscopy at high resolution and sorting. The microfluidic chip integrates novel microfluidic components to trap, position, immobilize, and sort/release animals. To characterize device operation and aid design of the device numerical models were developed. The experimental results demonstrate that the device operates robustly in a completely automatable manner. Additionally, a sophisticated control algorithm developed by Matthew Crane (Dr. Hang Lu's lab) automates the entire process of image acquisition, analysis, and sorting, which allows the system to operate without human intervention. This microsystem sorted worms based on their fluorescent expression pattern with over 95% accuracy per round at a rate of several hundred worms per hour.

Secondly, the technologies developed for the imaging/sorting system were adapted and further improved to develop a microsystem for high-throughput cell laser ablation of *C. elegans*. The multiplex ablation module combined with the embryo trap

module enables robust manipulation of embryos/L1-stage *C. elegans*. In addition, software for image processing and automation was developed to allow high-throughput cell ablations. This system performed ablation of a large number of animals and demonstrated accurate ablation by showing behavioral defects of the ablated worms in a chemotaxis avoidance assay.

Thirdly, to aid future development of the microdevices, a novel *in situ* method for three-dimensionally resolved temperature measurement in microchannels was developed. This method uses video-microscopy in combination with image analysis software (developed by Jaekyu Cho in Dr. Victor Breedveld's group) to measure Brownian diffusion of nanoparticles that is correlated to temperature. This method offers superior reproducibility and reduced systematic errors. In addition, we demonstrated that this method can be used to measure spatial temperature variations in three dimensions *in situ*.

Lastly, a method for pressure measurement in microdevices was also developed through collaboration with Hyewon Lee (Dr. Hang Lu's lab) to aid further device optimization. These micro pressure-sensors are composed of two flow layers with a polydimethylsiloxane (PDMS) membrane in between. The membrane deforms as a function of pressure and its deformation is quantified by a simple image-based method. These sensors offer high-precision pressure measurement in broad sensing ranges. In addition, a pressure transduction scheme combined with imaging-based method enables multiplex pressure measurement for simultaneously detecting pressures in multiple locations in a microsystem.

Overall, the technologies developed in this thesis will establish a solid basis for continuous improvement of the microsystems for multi-cellular model organisms. This high-throughput technology will facilitate a broad range of biological and medical research.

CHAPTER 1

INTRODUCTION

1.1 *C. elegans* as a model system for biological study and drug discovery

Small multi-cellular organisms, such as the free-living soil nematode, *C. elegans,* and the zebrafish, *Danio rerio*, have been critical in providing new insights in understanding cell lineage, neurobiology, cell death and human diseases ranging from neurodegenerative disorders to cancer [1-5]. The recent development of high-throughput genetic techniques has become widely applied to these model organisms and revolutionized our understanding of biological phenomena [3, 6-8]. Among these multi-cellular organisms, *C. elegans* has unique advantages. Not only is its genome fully sequenced [9, 10] and well-studied, but also its small size (length ~ 1 mm, width ~ 60 μm) allows complete anatomical description of the animal (by the electron microscopy), including a complete synaptic wiring diagram of the 302 neurons [5, 11]. It provides a unique opportunity to study and define neuronal mechanisms from sensory stimulus to behavior. Many knockout mutants are available for ~19,000 predicted genes and the discovery and availability of RNAi gene knockdowns has facilitated a broad range of genetic studies [7, 8, 12]. Its transparent body and nearly invariant cell lineage, coupled with fluorescent protein technology, enable precise cell-by-cell analysis of biological phenomena throughout development [6]. Although there are important physiological differences between nematodes and mammals, the conservation of many genes and fundamental cellular processes between nematodes and mammals make *C. elegans* an attractive organism to be used in drug screening [1, 2]. Many biotechnology companies, as well as pharmaceutical companies, now employ *C. elegans* in their drug discovery processes. Another great advantage of *C. elegans* is ease of maintenance in the laboratory. Their small bodies and short generation time (3 days at room temperature)

allow worms to be cultured by the thousands in small plates with *Escherichia coli* (*E. coli*) as a food source. These unique advantages of *C. elegans* combined with high-throughput genetic tools make *C. elegans* readily adaptable for automation and high-throughput experiments.

1.2 The need for high-throughput imaging, sorting, and laser ablation methods

Major conventional experimental methods, such as *in vivo* microscopy, visual phenotyping, and laser ablation technology, have been broadly used for biological researches in *C. elegans*[2, 5, 13-19]. However, lack of technologies that could reduce experimental time and human intervention in these methods becomes a limitation in these studies [6, 16]. For example, *in vivo* microscopy is one of the most important tools for biological studies. It is becoming more important to image large number of samples with high resolution since large-scale genetic studies are becoming feasible, thanks to recent progress in genetic technologies[12, 13, 20-22]. For instance, the completed genome sequence[9], coupled with the discovery of RNA interference (RNAi)[7, 8, 20, 23] and the development of fluorescent proteins, enables global studies of gene function and expression in *C. elegans* [6]. This kind of genome-wide promoter activity analysis often requires high-resolution microscopy and examination of a large number of individual animals[13]. However, in order to image animals with conventional microscopy, a technician needs to immobilize samples with anesthetics, manually mount the samples on a slide glass, locate each individual, and image them[16, 19]. This painstaking manual handling not only significantly limits the experimental throughput, but also increases noise due to variation in sample-to-sample handling[16, 24].

Another example is visual phenotyping and screening [2, 25]. Forward genetics by screening mutagenized populations has long been a powerful technique[2]. In addition, reverse genetic approaches such as RNAi knockdown have recently become prevalent in

the study of small genetic model organisms especially in large-scale genomic studies of cell biology and development[8, 21, 25, 26]. For these screens, a technician is required to record the orientation and position of the mounted animals on the slide, examine each individual, and rescue the mutant of interest by sliding the coverslip off and transferring the animal back onto a culture dish. This process takes at least 5 min/worm. Therefore, a mutant screen that typically requires examination of over 50,000 individuals takes over a month. This low-throughput nature of the manual method has been the current bottleneck for large-scale genetic studies.

The manual sample handling also remains a bottleneck in the laser ablation of cells[16]. Laser microsurgery is broadly used in ablating cells *in vivo* to study cell-cell interaction during development and how neuronal circuits result in behavior. For instance, a fundamental question in neuroscience is how cells in a neural circuit and their connectivity to other cells contribute to the behavior of the organism. In these behavior studies, individual neurons are often ablated by a focused laser beam and animals' behavior changes are examined to infer the function of neurons[17, 18, 27]. Although powerful due to its specificity as opposed to genetic ablation[15], laser ablation has drawbacks in that the difficulty of performing ablation significantly limits the throughput and also introduces large sample-to-sample variation[16]. For example, successful ablation typically occurs at a rate of a few animals per hour, rendering it impossible to acquire the hundreds of age-synchronized animals required for many population behavior assays. As the number of neurons required to be ablated increases, both the success rate and the throughput suffer. Because the ablated animals often show subtle abnormalities and many assays are inherently noisy, often many animals are required in order to identify reliably the phenotypical changes[4, 17, 28]; the low-throughput and difficult-to-use nature of the laser ablation limits its use and the pace of discovery, especially in combination with methods requiring large number of animals (e.g. behavior and RNAi).

Therefore, for both high-resolution microscopy / phenotyping and laser ablation, automated sample handling and digitized image analysis will greatly improve experimental throughput and data quality. It will facilitate the investigation of a vast array of fundamental biological mechanisms that govern development, cell-cell communication, synaptogenesis and disease mechanisms.

1.3 Advantages of using microfluidic systems

Microfluidics is the science and technology of systems that manipulate small (10^{-9} to 10^{-18} liters) amounts of fluids, using channels with dimensions of a few to hundreds of microns[29-34]. Microfluidic systems have distinctive physical characteristics compared to macroscopic systems[29, 32, 34, 35]. In a microchannel when two fluid streams come together, the flow is laminar (usually at very low Reynolds number) and the dominant mixing mechanism is the result of diffusion of molecules across the interface between the fluids[29, 32, 34, 36, 37]. This unique behavior of liquids at the microscale allows greater control of concentration of chemicals, culturing environment of cells, and even multi-cellular organisms[30, 31, 38-46]. The large surface-area-to-volume ratio and small thermal mass facilitate rapid heat transfer in microfluidic systems and enable precise spatial-temporal temperature control[47-49]. Additionally, many electrical components can be integrated on chip and allow the microsystems to perform complex functions[33, 50-52].

Much of the research in microfluidic systems has been carried out in a polymer, PDMS[31, 53-58]. It is 1,000,000 times more flexible than silicon and easy to fabricate the components required for microanalytical systems, such as valves and pumps[55, 59]. Recent development of new methods of complex multilayer microfabrication in PDMS enables high degree of integration[54, 55, 60, 61]. This material is optically transparent, so it can be used with conventional optical methods of detection. In addition, its bio-compatibility makes this elastomer particularly suitable for work with living cells and organisms[62, 63].

From single-cell assays to cell sorting, many micro devices have been developed and have revolutionized throughput of experiments in broad area of single cell studies[22, 31, 62]. However, its impact on multicelluar organisms has not yet been realized mostly because of difficulties of handling live moving multi-cellular organisms.

1.4 Other technologies for handling genetic organisms

Despite the wide application of these methods and their technical limitations, little has been done to automate imaging / phenotyping and laser ablation of multi-cellular organisms. The only commercially available system, Complex Object Parametric Analyzer and Sorter (COPAS™)[13, 64-66] from Union Biometrica, automates optical analysis and sorts living *C. elegans* on the basis of fluorescent protein expression patterns and other optical signatures, at rates up to about 100 organisms per second. It can provide quantitative digital data of GFP expression level along the anterior-posterior axis of *C. elegans*[13]. Although powerful, COPAS is significantly limited by its tissue-level, 1-D resolution capability, and low data-content per sample. When single-cell and subcellular imaging resolutions are required, which is likely to be the case for studying cell fate in development or synapse structure and function[25, 67-73], a new approach is required.

In parallel to this thesis work, a few microfluidic systems have been developed to study fly development[38], zebra fish embryo development[74], behavior of worms[75, 76], to image[77-83], and ablate worms[77, 78]. In particular, the microsystems for worm imaging have grown increasingly sophisticated in their design as well as in the quality and speed of data analysis. Heng *et al.* developed a microfluidics-based lensless imaging technique[83]. Using nanoaperture array they acquired worm images comparable to those obtained with a microscope (40X objective lens). However, it can image only a single focal plane (2D), and the technique cannot handle moving (live) organisms. Moreover, to

minimize sample movement, which is required for high-resolution imaging, euthanized worms were used and on average, approximately 45% of the acquired images were rejected due to sample rotation and nematode aggregation. Hulme *et al.* developed a network of microfluidic traps that is capable of immobilizing over 100 live worms in less than 15 min[81]. These wedge-shaped channels physically prevent the worms from moving and this immobilization process is gentle because it does not require gluing the worm or treating the organism with drugs. However, it proved to be inadequate for high magnification imaging and laser ablation due to the animals' inner body movement, such as pharyngeal pumping. Rohde *et al.* utilized an intricate sequence of valves and flow maneuvers to handle worms in a microfluidic device[80]. Although they demonstrated that the device can handle one worm at a time for imaging and sorting, the worm handling process uses a complex multistep loading mechanism that requires additional image acquisition, analysis, and valve actuation. This multistep process significantly limits throughput and makes it difficult to automate the worm handling process. In addition, mechanical immobilization using multiple aspiration channels is not sufficient to completely restrict worms' movement[77]. Two independent groups, Guo *et al.* and Zeng *et al.*, used a deformable membrane to compress a worm for immobilization and performed femtosecond-laser microsurgery[77, 78]. They proved that the valve compression effectively immobilizes animals for the duration of laser ablation. However, the worm handling process still includes complex steps that not only slow the entire process, but also make it difficult to automate. Thus far, no microsystems meet the specific requirements of automation for large-scale imaging, sorting, and laser ablation.

1.5 Thesis objective

The purpose of this thesis is to develop microsystems for high-resolution imaging and high-throughput sorting/laser ablation of *C. elegans* to overcome low-throughput nature of the major conventional methods. The specific research objectives of this thesis are (1) to develop a microfluidic device to route, trap, position, immobilize, and collect individual animals; (2) to develop automated high-throughput systems by integrating off-chip components (macro valves, x-y-z stage, EM CCD camera, a Peltier cooling system, and a laser) and using processing algorithm to automate the process; (3) to apply these systems to the imaging, sorting, and laser ablation of *C. elegans*. In the process of meeting the first objective, we developed novel microfluidic components (Chapter Two and Chapter Three). Proper operation of these components relies on precise pressure and temperature control in microsystems. In order to assist optimization of the microdevices in the future we also developed novel methods for measuring temperature (Chapter Four) and pressure (Chapter Five) in microfluidic devices.

1.6 Thesis outline

The thesis is divided into seven chapters. Chapter two presents the design of the automated microsystem for high-throughput imaging/sorting and its applications. Novel microfluidic components for handling worms as well as integration of the system are discussed. Next, Chapter Three addresses unique features of the automated microsystem for high-throughput laser ablation and how this system can be used for studying neuronal networks in *C. elegans*. Chapters Four and Five present temperature and pressure measurement methods in microsystems. Each of these two chapters contains motivation, relevant review, measurement mechanism, design of devices, and applications. Chapter Six presents an overall discussion to this dissertation. Finally, the last Chapter provides concluding remarks and suggestions for future work to improve the microsystems.

CHAPTER 2

AN AUTOMATED MICROSYSTEM FOR HIGH-THROUGHPUT IMAGING AND SORTING

2.1 Overview

This chapter describes an integrated and automated microsystem for performing high-throughput microscopy at high resolution and for sorting based on phenotype. Our PDMS microfluidic chip uses on-chip valves to control a suspension of nematodes and differs from previous work in the integration of several key design features that enable robust operation which is critical for high-throughput experiments. Additionally, a sophisticated control algorithm automates the entire process of image acquisition, analysis, and sorting, which allows the system to operate without human intervention. We implemented the classification and sorting of worms based on many characteristics, such as intensity and patterns of fluorescent markers. This microfluidics-enabled computer-automated approach can perform screens based on cellular and subcellular phenotypes with over 95% accuracy per round at a rate of several hundred worms per hour, and thus provides a means for high-throughput studies. This work is performed in collaboration with Matthew Crane in Dr. Lu's group. Matthew developed the automation and image processing software and part of the hardware. This chapter is adapted from Reference 79.

2.2 Integrated microsystem overview

Fig. 2.1a shows basic concept of the microsystem. In each experiment, a mixed population of worms are manipulated by a simple scheme of load, image, phenotype, and release or sort: first, a single worm is automatically loaded into the engineered microchip

by a constant pressure-driven flow; then the worm is briefly (and reversibly) immobilized while multidimensional images of the worms are acquired on-chip; then phenotyping and sorting take place, and images are stored for analysis. This cycle repeats automatically.

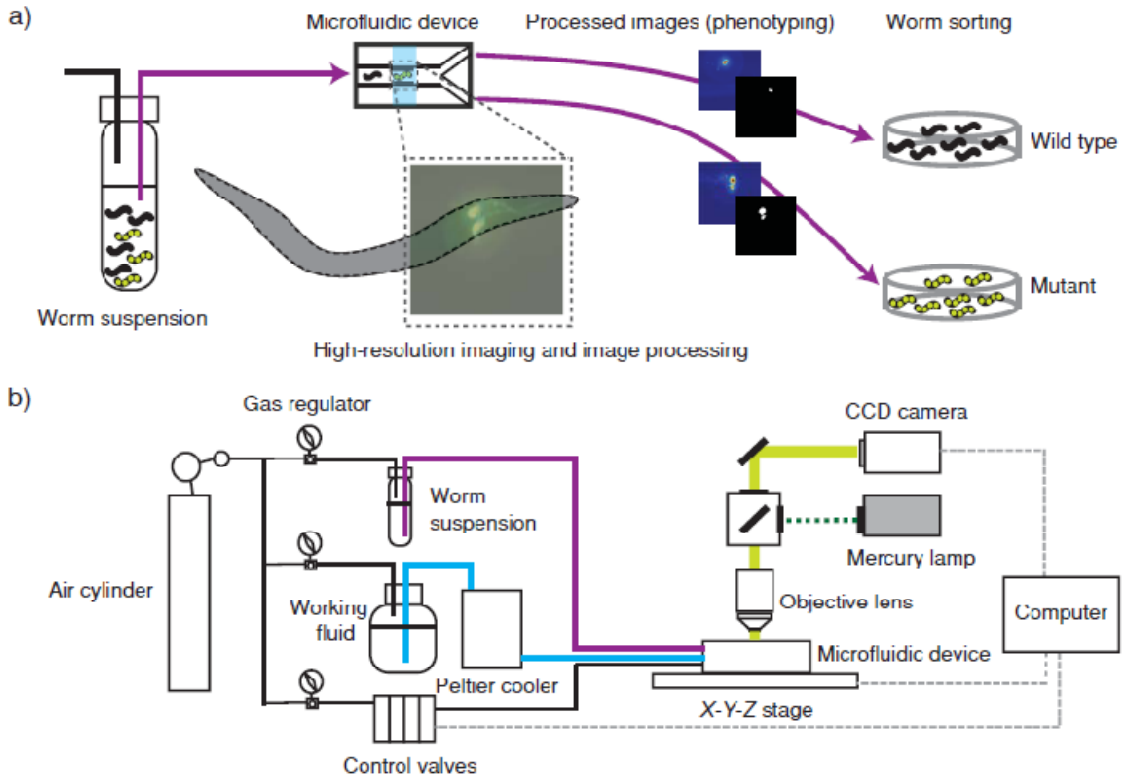

Figure 2.1. Schematics of the system. a) A mixed population of worms is injected into the device, worms are imaged, phenotyped and then sorted. b) System block diagram showing the on-chip and off-chip components.

The system consists of two components (Fig. 2.1b): one is the microfluidic device that routes, traps, positions, immobilizes, and sorts/collects *C. elegans*; the other is the external components for supporting the device and imaging samples including a compound microscope with CCD camera, x-y-z-stage, Peltier cooler, macrovalves, and pressure driven injection system (Appendix A). Animals suspended in a buffer solution are injected into the device by pressure driven flow. They travel through the channels and one animal at a time is positioned in the detection zone of the device. Microvalves integrated on chip are controlled by macrovalves actuated by a Matlab (the Mathworks,

Inc.) program to control the flow inside the device. The nematode is then rapidly immobilized by cooling. The Matlab program then acquires images from the CCD camera at a variety of focal planes by manipulating the x-y-z-stage. These 3D images are processed automatically to sort the worm.

2.3 Design process of the engineered microchip

2.3.1 Basic concepts of the microfluidic chip

The microfluidic chip performs the following tasks in order to route the worms to the desired position: 1) a trap structure in the entrance of the detection zone (Fig. 2.2d) regulates loading of a worm; 2) positioning channels guide the worm that passes the trap into the detection zone (Figure 2.2c); 3) cooling immobilizes the worm positioned in the detection zone (circle in Figure 2.2c) to completely immobilize it (Figure 2.2c). After image acquisition and image processing, the worm is removed through to one of the outlets.

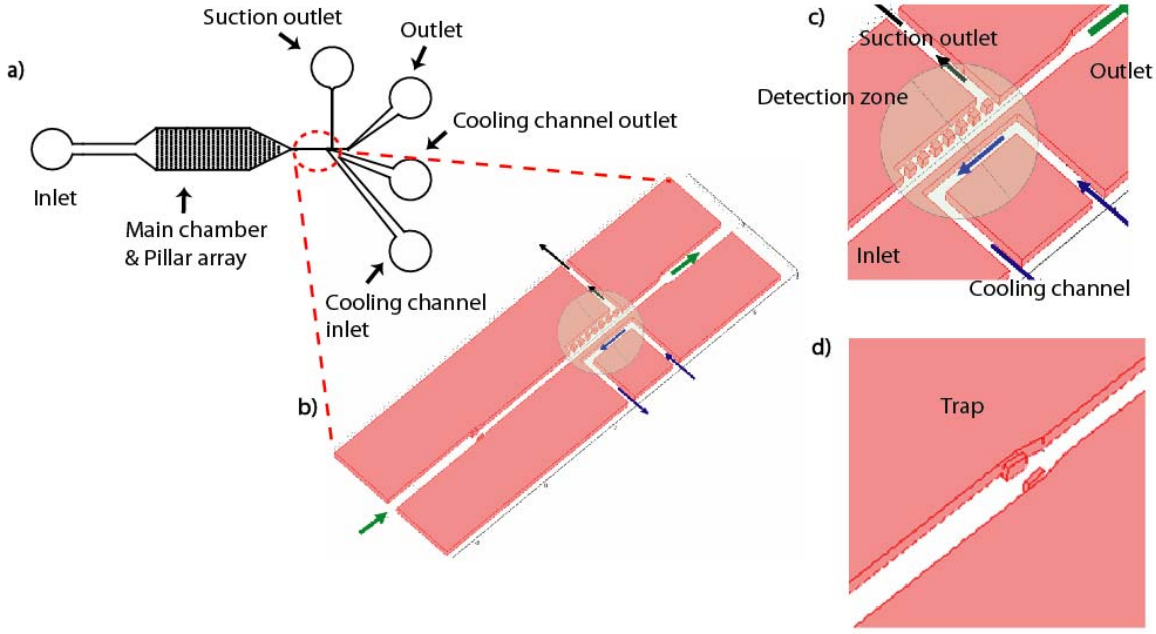

Figure 2.2 The first generation design of the microfluidic chip. a) PDMS microchip layout; b) Schematic of the trap and detection zone. Green arrow: sample, black arrow: suction, blue arrow: cooling flow; c**)** Detection zone; d) Trap for self-regulating loading of samples.

2.3.2 Integrated on-chip valves

The first generation device consists of a single-layer PDMS microfluidic chip bonded onto a glass coverslip. PDMS is a soft material with Young's modulus ~750 kPa, which can be deflected with small forces[84]. Structures with high aspect ratio, such as the worm loading chamber, are especially prone to deformation and storing energy when pressure is applied[85]. Once the pressure is removed, the deformed PDMS slowly return to the former state and release the stored energy. This mechanical compliance of the device causes flow fluctuation in the detection zone and thereby disturbance of a loaded worm.

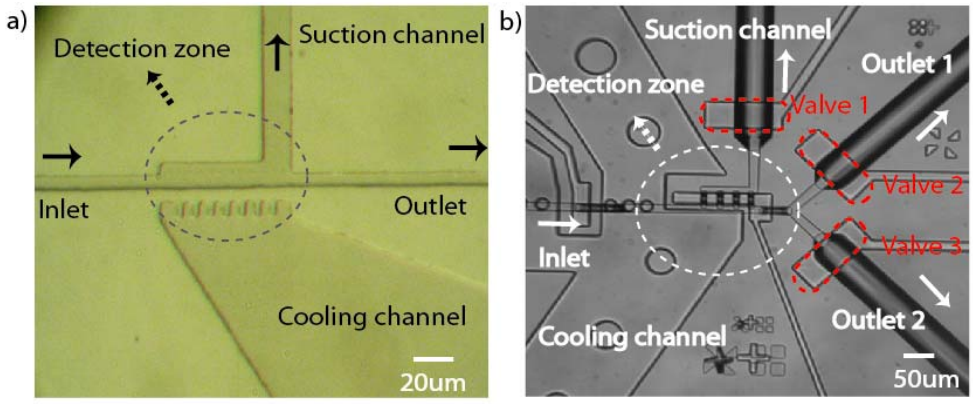

Figure 2.3. Optical micrographs of the a) 1st generation device and b) the current device. Valves are integrated and actuated to prevent flow fluctuation in the detection zone.

In order to address this issue, we fabricate on-chip valves using multilayer soft lithography and actuate them to eliminate flow fluctuation in the detection zone (Fig 2.3b)[55]. The device consists of two layers of PDMS: a worm loading layer and a valve control layer. The membrane of PDMS between the layers is engineered to be relatively thin (10 ~ 20 μm). When pressure is applied to the channel in the valve actuation layer, the membrane deflects toward the worm loading layer and closes the channel. Once the worm is positioned in the detection zone, the three valves located in the suction channel (valve 1) and two outlets (valve 2, valve 3) are closed to infinitely increase the hydrodynamic resistance of the channels. This prevents the rest of the deformed device from releasing stored energy and causing flow fluctuation. We demonstrated by tracking fluorescent particles that turning the valves on can effectively eliminate any flow fluctuation in the detection zone.

2.3.3 Novel fabrication method to improve optical resolution

The conventional on-chip valve requires an additional PDMS layer between the cover glass and worm loading layer. The additional layer contains channels for actuating on-chip valves and circulating cooling fluid. The materials in the layer have different

refractive indices (water of 1.33, air of 1.00 and PDMS of 1.45) and refractive index change along the path of light rays causes significant reflection (Fig 2.4a, blue arrows) and thereby lowers the optical resolution.

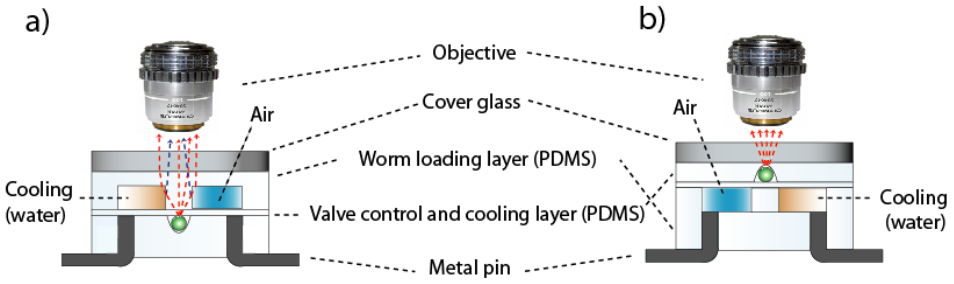

Figure 2.4. Schematics of cross-sectional view of the detection zone: a) Conventional valve device where actuation layer is next to the coverslip; b) Modified valve device. Blue arrow: reflected ray; red arrow: transmitted ray.

In order to improve the optical resolution, we developed a fabrication technique for a novel on-chip valve structure that enables the sample to be brought into close proximity with the cover glass (Fig 2.4b). This valve design eliminates the layer of materials between the cover glass and a worm, which minimizes changes in the refractive index of the imaging medium along the path of light lays. We demonstrated that this new design is capable of imaging subcellular structures, comparable to that of current standard optical microscopy.

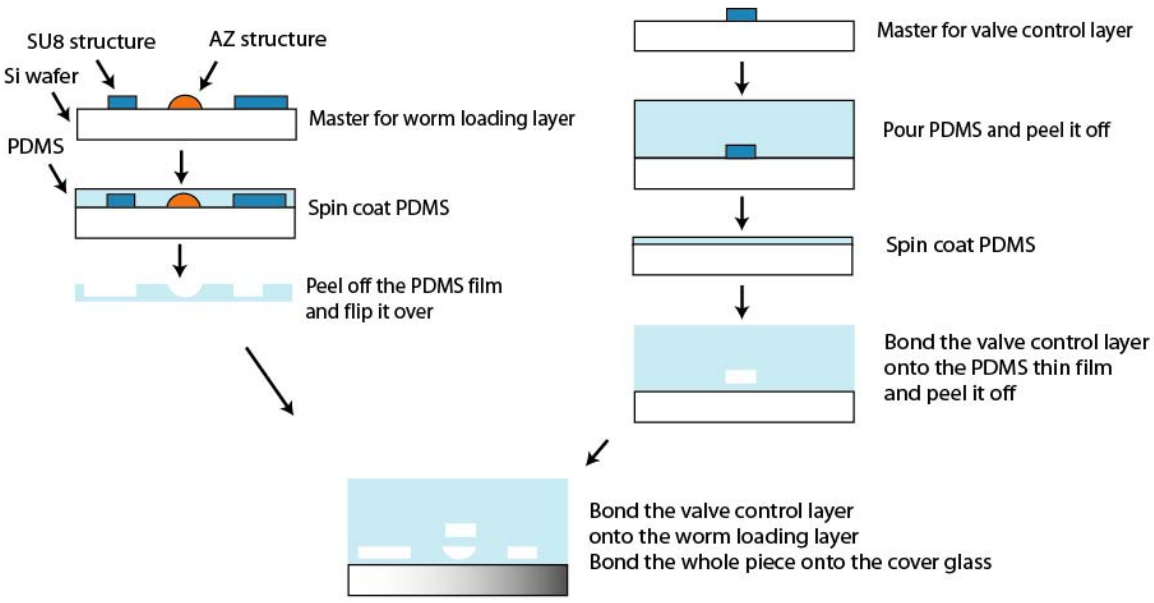

Figure 2.5. The fabrication process of the microchip.

The microfluidic device was fabricated using multi-layer soft lithography. Two different molds were first fabricated by photolithographic processes to create the worm loading layer and the control layer. The mold for the worm loading layer was made by a two-step photolithographic process. In the first step, a 30-µm-thick negative photoresist (SU8-2025, Microchem) was spin-coated onto a silicon wafer for the worm loading chamber and the detection channel (Appendix Ba). The loading regulator, side channels, and outlets (Appendix Bb) were then fabricated with a 25-µm layer of positive photoresist (AZ 50XT, AZ Electronic Materials) on the same wafer. After the positive photoresist was developed, the wafer was heated at 125 ºC for 5 min to allow the positive photoresist to reflow so that the channels form a smooth and rounded shape. The master for the control layer (Appendix Bc) was made of a 50-µm layer of negative photoresist (SU8-2050, Microchem) on a silicon wafer. The two molds and a blank wafer were treated with tridecafluoro-1,1,2,2-tetrahydrooctyl-1-trichlorosilane vapor (United Chemical Technologies) in a vacuum desiccator to prevent adhesion of PDMS during the molding process.

For fabricating the control layer polydimethylsiloxane (PDMS, Sylgard 184, Dow Corning A and B in 5:1 ratio) was poured onto the control-layer master to obtain a 5 mm-thick layer. Mixture of PDMS (A and B in 20:1 ratio) and THF in 2:1 ratio was spin-coated on a blank wafer to give a 20-μm-thick layer. Both were partially cured at 70 ºC for 20 min. The thick control layer was then peeled off from the master and holes were punched for access to the control and cooling channels. The control layer was then bonded to the thin PDMS membrane on the blank wafer. This assembled control layer was fully cured at 70 ºC for 2 hours. For the worm-loading layer, PDMS was spin-coated onto the master to give a 60-μm-thick layer. The worm-loading layer was fully cured in a convection oven at 70 ºC for 2 hours and was then peeled off from the master[86]. The layer was then turned upside down and bonded to the control layer using oxygen plasma treatment. Another set of holes were punched for access to the worm loading channel. These assembled layers were then bonded onto the cover glass to form the micro device.

2.4 Final design of the microdevice

After several generations of design and optimization, we finalized the device design that has 4 salient features that ensure a consistent and reliable operation for an extended period of time (Fig. 2.6): self-regulated loading, consistent positioning in the detection zone, on-chip cooling for immobilization, and no small features prone to clogging.

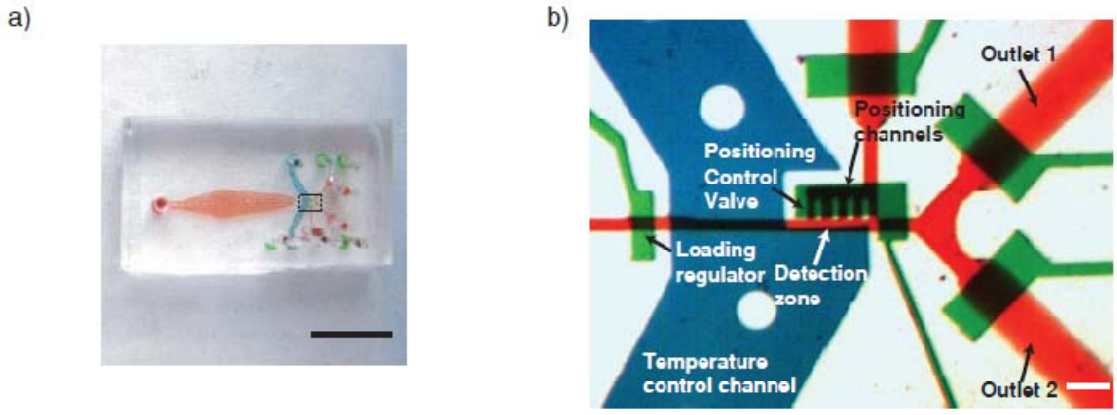

Figure 2.6. The finalized device. a) Photograph of the microdevice. Scale bar: 5 mm. b) Optical micrograph of the microchip's active region (boxed region in a). The channels were filled with dye to show specific features: blue, temperature control channel; green, valves; and red, sample-loading channel. Scale bar: 100 µm.

2.4.1 Self-regulated loading of worms

In order to prevent multiple worms from entering the detection zone, we designed a self-regulated loading scheme. Multiple worms in the detection zone can cause the following problems:

- Significant distortion of the shape and orientation of a worm of interest. We use transgenic animals that express fluorescent protein in a particular set of cells. Microscopy and visual screen rely on native morphology and relative position of cells. If multiple worms are present in the small detection zone, the animal's squeezable body can be easily distorted and cause errors in image processing.
- Fluorescence signals from other worms in the field of view can be mistakenly identified as from the worm of interest. It causes significant errors in sorting and laser ablation since the image processing program cannot recognize animal outlines if the images are taken in the fluorescent mode.
- Aggregation of worms causes clogging of the channel. Once the device is clogged, the system must be manually stopped to apply high pressure to the

device to flush out aggregated worms. In many cases, high pressures cause break-down of the devices.

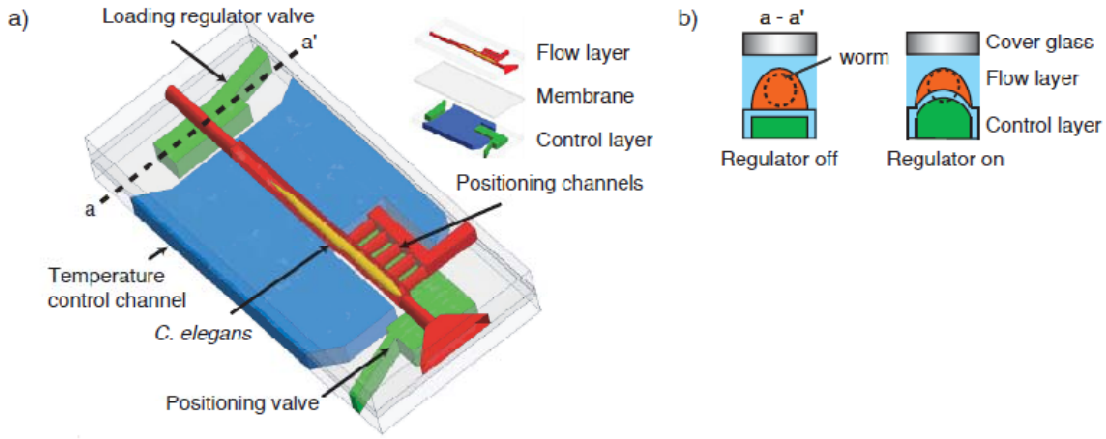

Figure 2.7. Three dimensional structure of the detection zone. a) Artist's rendering of the detection zone of the microchip showing device layers in 3-D. Inset: exploded view of the schematic illustration showing the individual layers. b) Schematics of cross-sectional view (a-a') of the self-regulated sample-loading valve in (a).

Therefore, to avoid these problems, we implemented the sample-loading regulator design by controlling the pressure on a partially closed valve (Fig. 2.7b). The scheme to load a worm at a time takes advantage of the squeezable body of the nematode and pressure drops created by a loaded worm. *C. elegans* is enclosed by an elastic cuticle layer. This layer is pushed outward by a high internal hydrostatic pressure relative to the ambient, which results in the nematode adopting a cylindrical tube structure. For a worm to pass through the trap that has a narrower channel width than the diameter of a worm, the elastic cuticle layer must be deformed against the hydrostatic pressure by the force generated by the pressure drop across the worm.

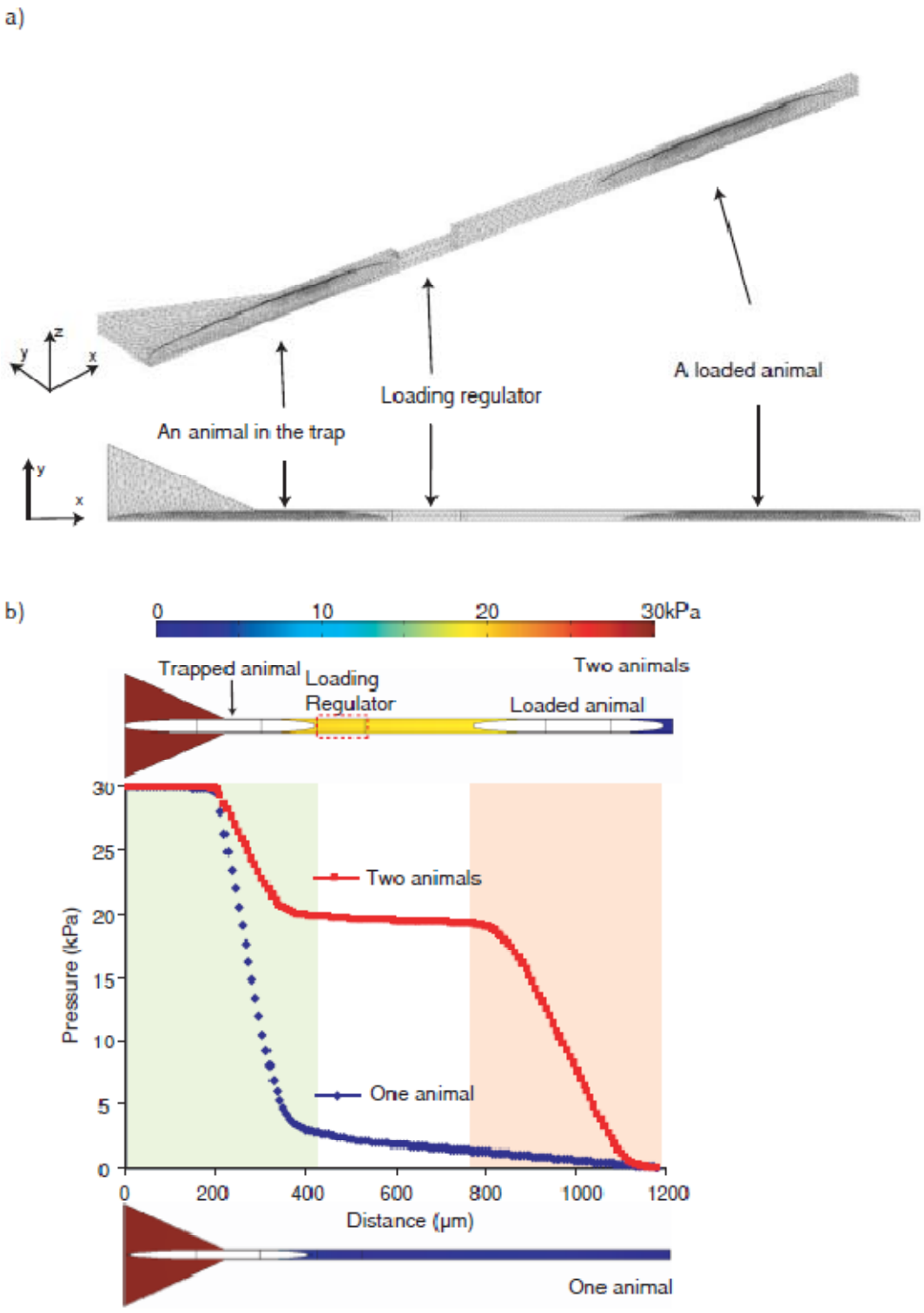

Figure 2.8. Mechanism of worm loading regulator. a) Geometry of the channels and finite element mesh used in numerical simulations. b) Pressure profile in the imaging chamber determined by 3-D numerical simulation in COMSOL. Top: top view of a two-animal model, showing pressure profile for a loaded animal in the imaging zone and a

second animal waiting behind the loading-regulator. Middle: line plot of the pressure profiles. Bottom: top view of a one-animal model, showing pressure profile for a single animal behind the loading regulator (and no animal in the imaging zone).

To aid the design of the loading regulator, we developed numerical simulations for characterizing the pressure distribution along the loading channel (Fig. 2.8). The simulations were performed using a commercial finite element package COMSOL (Stockholm, Sweden). The three-dimensional geometry of the loading channel, the loading regulator, and tubular-shape worms are shown Fig 2.8a. Because of the two fold symmetry of the device, the left half of the channel was drawn. The height of the partially closed loading regulator is assumed to be 20 μm. Incompressible steady-state Navier-Stokes equations were used to simulate flow in the channel. The pressure at the outlet was fixed at atmospheric pressure and the pressure at the inlet was set as 30 kPa. Boundary conditions for the channel walls and the surface of the worms were set as no slip.

When a worm is not loaded in the detection zone, over 90 % of the entire pressure drop occurs over the single worm in the trap, and this is great enough to deform the worm and push it into the detection zone (Fig 2.8b). In contrast, when an animal is present in the imaging chamber, the flow resistance is increased. The reduced flow rate lowers the pressure on a second animal. Now the pressure drop across the worm in the trap is too small (< 30 % of the entire pressure drop) to push the animal into the detection zone. Once a loaded worm leaves the detection zone, however, then the pressure drop across the trap becomes large enough to push the second worm into the detection zone.

Because of our ability to fine-tune the system pressure (5 - 10 psi) as well as the sample-loading regulator pressure (10 - 20 psi) we achieve great flexibility depending on the size of the animals for each application. This self-regulated loading scheme not only improves the accuracy of image processing by preventing the aggregation of worms in the detection zone, but also prevents clogging that could break down the device.

2.4.2 Consistent positioning of the worms in the detection zone

A worm that passes the trap is guided into the detection zone identically each time by the positioning channels so as to minimize the travel of the motorized stage to locate the worm. This feature greatly reduces the processing time and increases throughput. It is achieved naturally by the position of the worm relative to the positioning channels.

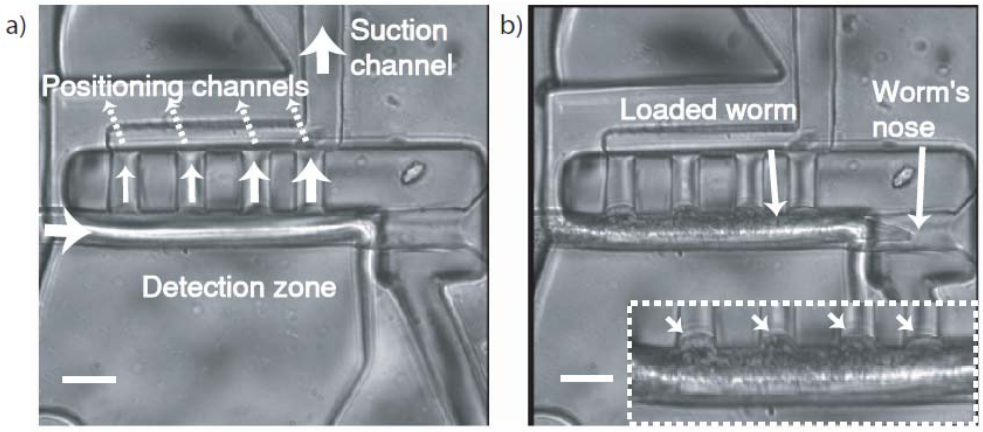

Figure 2.9. The working mechanism of positioning channels. a) Photograph of positioning channels. The thickness of white arrows represents the relative amount of flow. b) Photograph of a loaded worm in the detection zone. Small arrows point out the deformed body of the loaded worm because of the suction. The degree of the deformation of the body at each suction channel is similar.

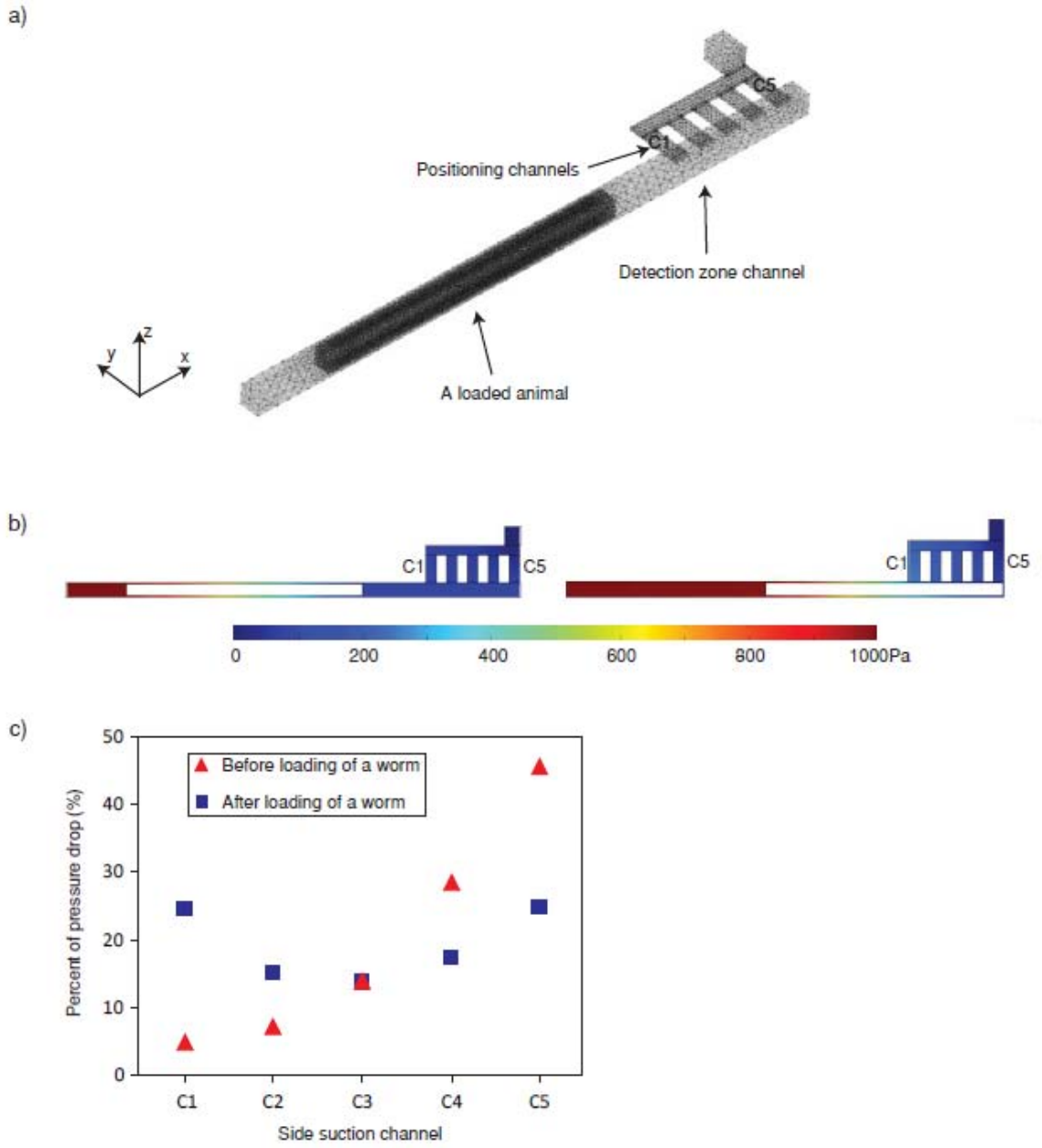

Figure 2.10. Mechanism of worm positioning. Pressure drop distribution along the positioning channels before and after a worm is loaded, determined by numerical simulations. a) Geometry of the channels and finite element mesh used in numerical simulations. Each positioning channel is labeled as C1-C5 from the left respectively. b) Pressure profile at the vertical middle plane of the positioning channel (2.5 μm from the bottom of the channel) before (Left) and after (Right) a worm is loaded. c) Plot of the fraction of pressure drop along each positioning channel before (triangle) and after (square) an animal is loaded.

Numerical simulations were developed to provide guide-lines for the design of positioning channels (Fig. 2.10). With these models we explored the pressure drop distribution along the positioning channels before and after a worm is loaded. To simplify the numerical simulations, a worm in the channel is assumed as a rectangular rod with 24-μm width and 500-μm length. The height of partially closed positioning channels is assumed as 5 μm. The width and height of the detection zone are 30 μm. The three-dimensional geometry of the detection zone and positioning channels are shown Fig 2.10a. Incompressible steady-state Navier-Stokes equations were used to simulate flow in the channel. Boundary conditions for the channel walls and the surface of the worms were set as no slip.

When no worm is loaded, the positioning channel closer to the main suction outlet has smaller hydrodynamic resistance and thereby has bigger suction force (Fig. 2.10b, c). This gradient of suction force of positioning channels drags the worm down to the end of the detection zone. Once the animal's nose or tail is positioned at the end of the detection zone, the hydrodynamic resistance of the positioning channels self-equalizes and thereby the pressure force is distributed (Fig. 2.10c). This distribution of the pressure force prevents the animal from being forced through the positioning channel and minimizes mechanical stress on the animal.

2.4.3 On-chip cooling to immobilize the nematode

The conventional microscopy and laser ablation method requires *C. elegans* to be immobilized by anesthetics. The potential adverse effects of the anesthetics (e.g. disruption of neuronal signaling and the induction of undesirable physiological changes) have limited experiments. To avoid using anesthetics, we have designed an integrated local temperature-control system whereby worms are cooled to ~4 ºC to immobilize them for imaging. Although mechanical immobilization of the worms by applying suction

reduced movement, it proved inadequate for high-magnification imaging with simple epifluorescence microscopy. The use of brief cooling, however, proved effective at stopping motion and we observed no discernible differences in the fluorescence pattern of cooled worms compared to those immobilized with sodium azide (Fig 2.11 c-e).

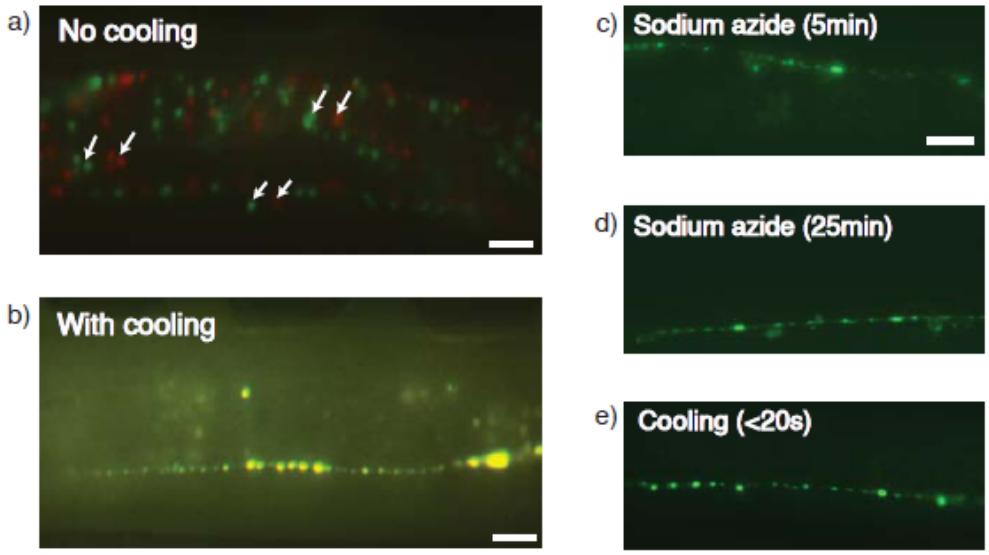

Figure 2.11. a) Two frames taken of a worm mechanically clamped with no cooling. The first frame was colored red and the second frame 270 ms later was colored green. Arrows point to features moved during the 270 ms. b) Two frames 10 s apart (also colored red and green) of a worm imaged with cooling to 4 ºC, showing no discernible movement. (c-e) YFP::RAB-5 distribution in immobilized worms. Representative images of YFP::RAB-5 distribution in *unc-16*$^{-/-}$ mutant immobilized with either (c, d) 10 mM of sodium azide or (e) cooling, showing similar punctual patterns. Scale bar: 10 µm.

The cooling channel is integrated underneath the worm loading channel in the valve control layer. Coolant is circulated through the channel to cool down the detection zone. *C. elegans* body temperature can be regulated by controlling its surrounding temperature. Once a worm is positioned in the detection zone, the animal is cooled within seconds because of its small thermal mass. Its low body temperature slows down the metabolism significantly and prevents the animal from moving. Because the time required for image acquisition and processing is on the scale of 10 seconds, the

undesirable effects of cooling are negligible.

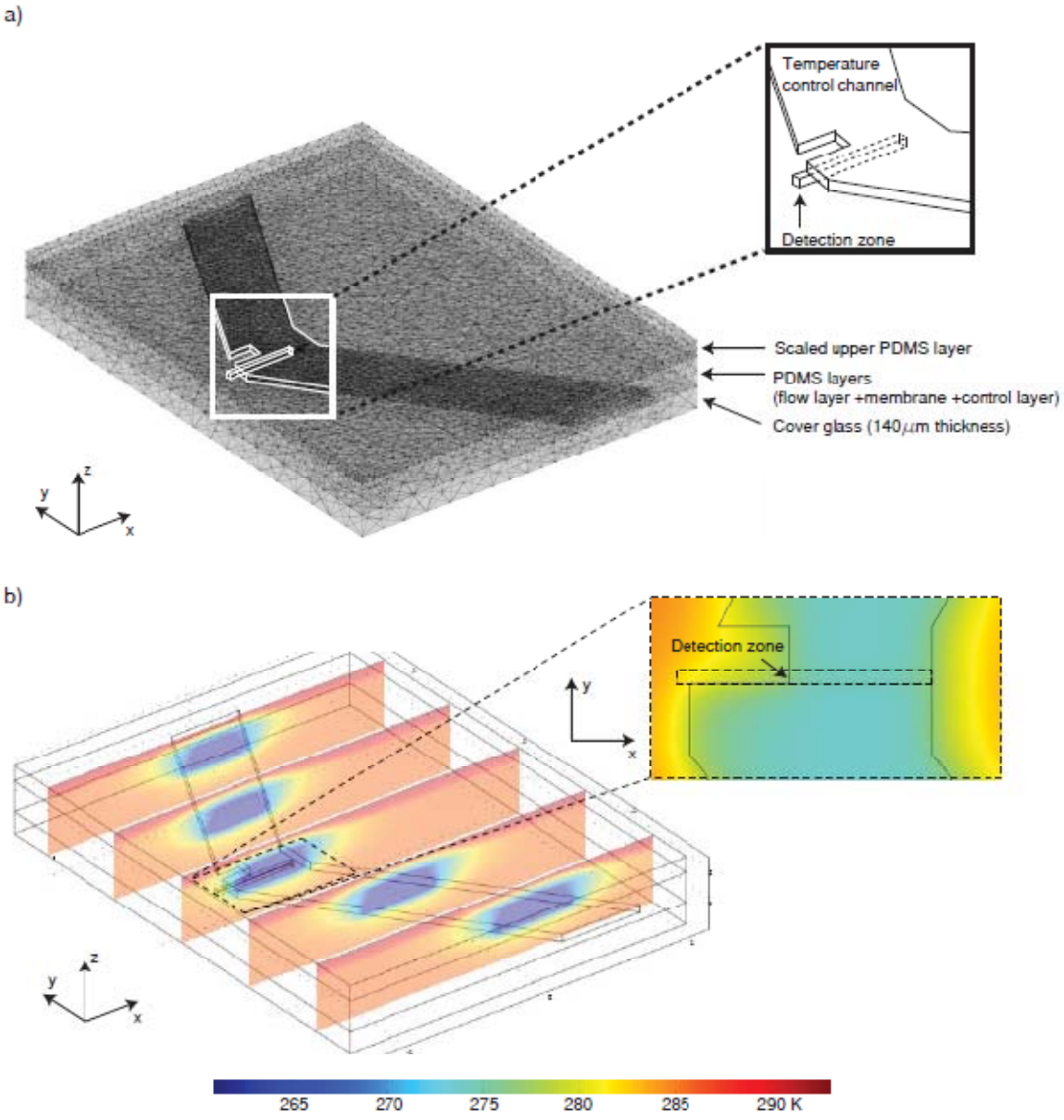

Figure 2.12. Temperature profile inside the device. Temperature profiles determined by numerical simulations using physical parameters and experimentally measured boundary conditions. a) Geometry of the device and finite element mesh used in numerical simulation. Inset: zoom-in view showing the outline of the temperature control channel and detection zone. b) Temperature profile at the various cross-section of the device showing local cooling. Inset: temperature profile at the vertical mid-plane of the detection zone.

To characterize the temperature distribution inside the chip, we use numerical simulations coupled with boundary conditions from experimentally measured values and physical parameters of the materials and fluids used in the experiments. The simulations of the coolant flow and heat transport in the device were performed using a commercial finite element package COMSOL (Stockholm, Sweden). The actual three-dimensional geometry of the section of the device is shown in Fig. 2.12a. To simulate coolant flow in the temperature control channel, the incompressible steady-state Navier-Stokes equations were used. The pressure at the outlet was fixed at atmospheric pressure and the fluid velocity at the inlet was set at the parabolic flow profile with the volumetric flow rate as measured. To simulate heat transport numerically, the convection-conduction equation was used. To reduce the number of mesh elements, the thermal conductivity of upper part of the PDMS and the actual geometry were rescaled by the equation, $k_{PDMS}/L_{PDMS} = k'_{PDMS}/L'_{PDMS}$. The temperature of the coolant at the inlet was fixed at 260 K as measured experimentally with a thermocouple. The temperature of the surface of the cover glass was also fixed at 286 K as measured. The temperature fields at the various cross-sections shown in Fig. 2.12b confirm localized cooling. Inset of Fig. 2.12b shows the temperature profile at the vertical mid-plane of the detection zone. Based on this model, the average temperature in the detection zone was found to be around 4°C.

2.4.4 In-line coarse filtering device & no small features prone to clogging

Dust particles in a sample suspension can clog micro-scale channels and cause improper operation of the device. To get rid of dust particles and debris, a filtering device has been developed (Fig. 2.13). The device is fabricated from PDMS and consists of parallel channels with a pillar array (Appendix C). The distance between adjacent pillars are 3~5 μm smaller than the width of the worm (~ 30 μm). Deformable worms can pass through the gap between pillars, but dusts bigger than the gap are filtered out.

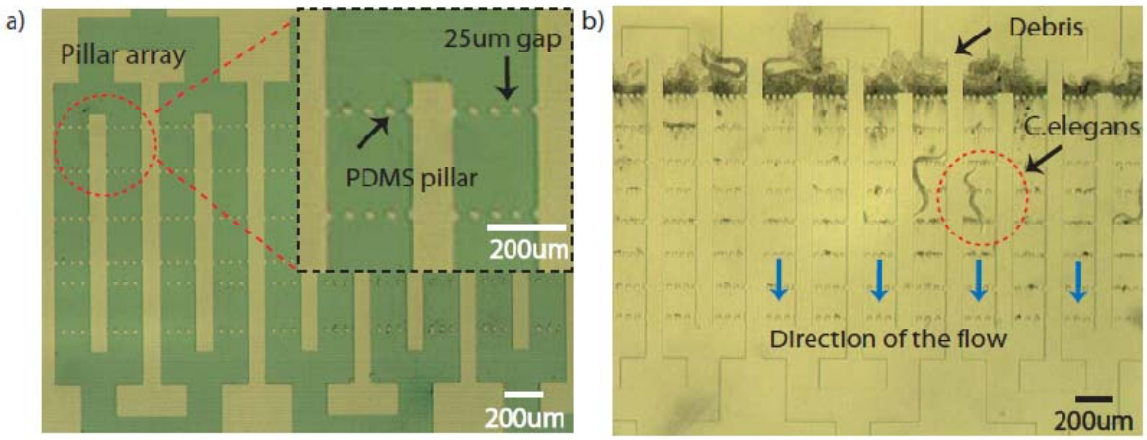

Figure 2.13. a) Filtering device. b) Debris aggregated in the filtering device.

However, small dust particles that cannot be filtered out using the filtering device can still clog the channels. The best way to prevent clogging would be to eliminate permanent small features vulnerable to dust. To do this, we developed size-adjustable elastomeric microchannels by actuating a control channel above (Fig. 2.14). The width of these channels is as big as that of a worm, but valves integrated on top of the channels can actively modulate the depth of the channel (to be smaller than the size of a worm).

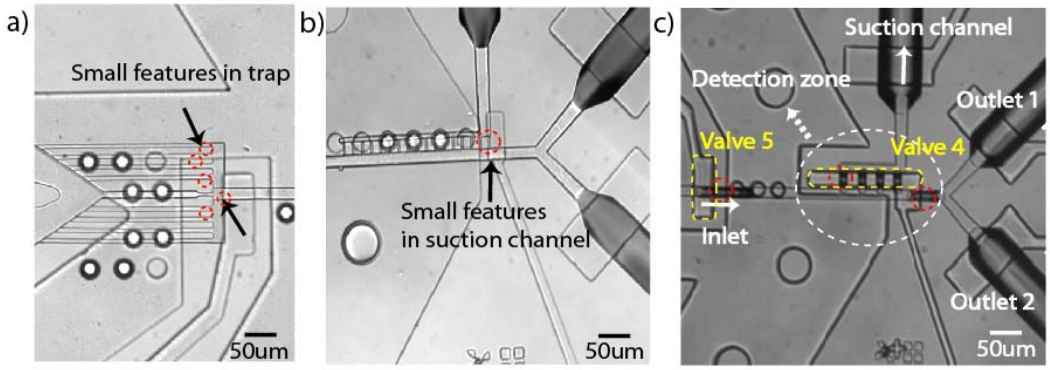

Figure 2.14. a) and b) The trap and suction channel images of the previous generation device. c) Finalized device with large width of trap and suction side channel. The width of trap and side suction channels are the same with that of a worm.

If the size-adjustable channels are clogged, the pressure applied on the valve can be released to increase the depth of the channel and flush out the dusts. This tunable trap and positioning channel design improved the robustness of the device dramatically and

enabled the device to handle large numbers of individual animals for a long period of usage.

2.4.5 Microfluidic device operation

An automated operation cycle of the microchip is demonstrated in Figure 2.15. Valve 1 is always partially closed to prevent multiple worms from entering. To load an animal into the imaging chamber, both outlet channels are closed while the side

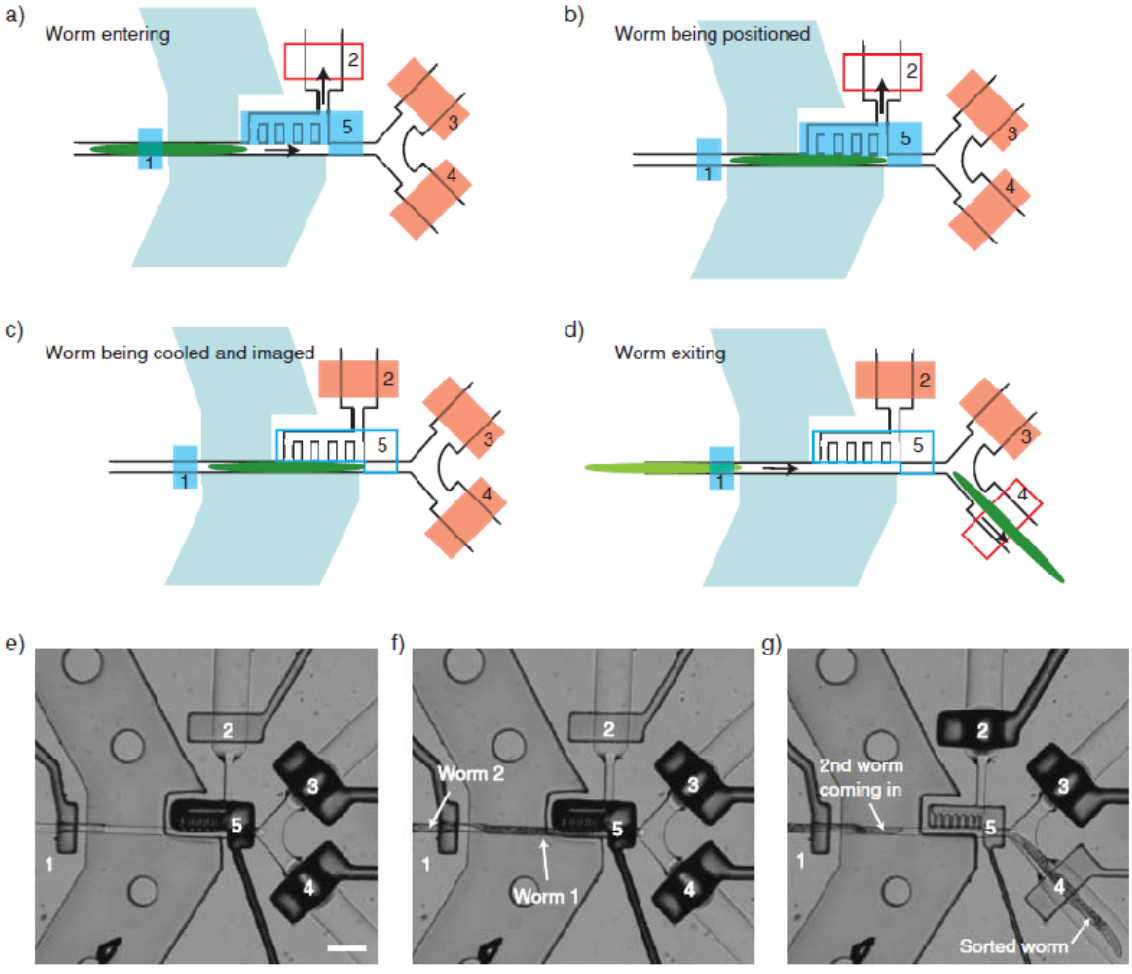

Figure 2.15. Microdevice operation. (a-d) Schematic diagrams summarizing the valve control sequence in the worm-sorting process (dark blue, partially closable and tunable valves; red, fully closable valves; open boxes, valves in closed position; colored boxes, valves in open position). a) Worm entering. b) Worm being positioned. c) Worm being

cooled and imaged. d) Worm exiting. (e-g) Frames from videos showing the chamber while waiting for a worm to enter. (e), with a loaded worm preventing a second worm from entering. (f), and a second worm automatically moving into the detection zone after the previous worm exited the detection zone. (g). Scale bar, 100 μm.

positioning channels remain open to generate a pressure gradient to guide a worm into the observation chamber. Once the worm is positioned in the observation chamber, all the valves for fluid to exit the observation chamber are closed to eliminate flow fluctuation. After imaging and decision making one of the exit valves (3 or 4) is opened to allow the imaged worm to leave. Once the worm leaves the observation chamber the valves return to the worm entering state. This automated phenotyping and sorting process is gentle, and in our experiments, ~ 100 % of animals were viable, crawling on agar and thrashing in buffer normally immediately after the processing.

2.5 Material and methods

2.5.1 *C. elegans* strains, culture, and sample preparation

The following strains were used in this work: CX6858 *tax-4(ks28); kyIs342 [pgcy-32::tax-4::GFP, punc-122::GFP]*, CX3695 *kyIs140 [str-2::GFP + lin-15(+)]*, CX3940 *kyIs140; rol-6(e187); slo-1(ky399)*, CZ5261 *juIs198 [punc-25-YFP::rab-5]*, and CZ5264 *unc-16(ju146); juIs198*. Animals were cultured according to established methods[19]. Age-synchronized L4 worms were prepared as follows: eggs were obtained by bleaching adults using a solution containing about 1% NaOCl and 0.1 M NaOH, washed and let hatch in M9 buffer, and cultured on Nematode Growth Medium (NGM) plates seeded with *E. coli* OP50. Animals were washed and suspended in M9 solution containing 0.5 wt% Bovine Serum Albumin (BSA) for each experiment. The worm suspension was flowed through the filtering device to remove debris.

2.5.3 System operation

System operation process is as follows: first, tubings and pins are properly connected to the device and the device is mounted on the stage of the microscope. After priming the device with the M9 buffer solution, the coolant is pumped through a tubing that is placed adjacent to the Peltier device. Worm suspension is then injected into the device using pressure driven flow. We use ~ 8 to 10 psi but the actual pressure depends on each system setup (e.g. the length of the tubing). After performing imaging/sorting, we flush the lines with enough buffer solution to collect animals and spin down the suspensions in the collection tubes. The animals are then transferred onto NGM plates seeded with *E. coli* OP50.

2.6 Results and discussion

2.6.1 Large-scale expression pattern analysis

Gene expression pattern analysis is a common technique in genetic and genomic studies. Typically one would be interested in the intensity, location, and timing of the appearance of a (fluorescent) reporter. We tested the capacity of our system to rapidly analyze the gene expression patterns in a population of worms carrying a reporter transgene *kyIs342*. In this strain GFP is expressed in sensory neurons AQR, URXL/R and PQR, and in coelomocytes (coinjection marker punc-122::gfp). In addition, we observed background fluorescence in the intestine.

In this experiment, worms were freely moving and we used no immobilization; we acquired all images at room temperature (20 ºC) and 10X magnification. The software processed images to distinguish specific neurons not only from background autofluorescence and from coelomocytes but also from each other. We could identify the neurons in each image (Fig. 2.16). We found that GFP expression in the URX neurons

was consistent, but expression in AQR and PQR neurons was stochastic, with four possible combinations: GFP expression in neither, both or one of the two cells (Fig. 2.16).

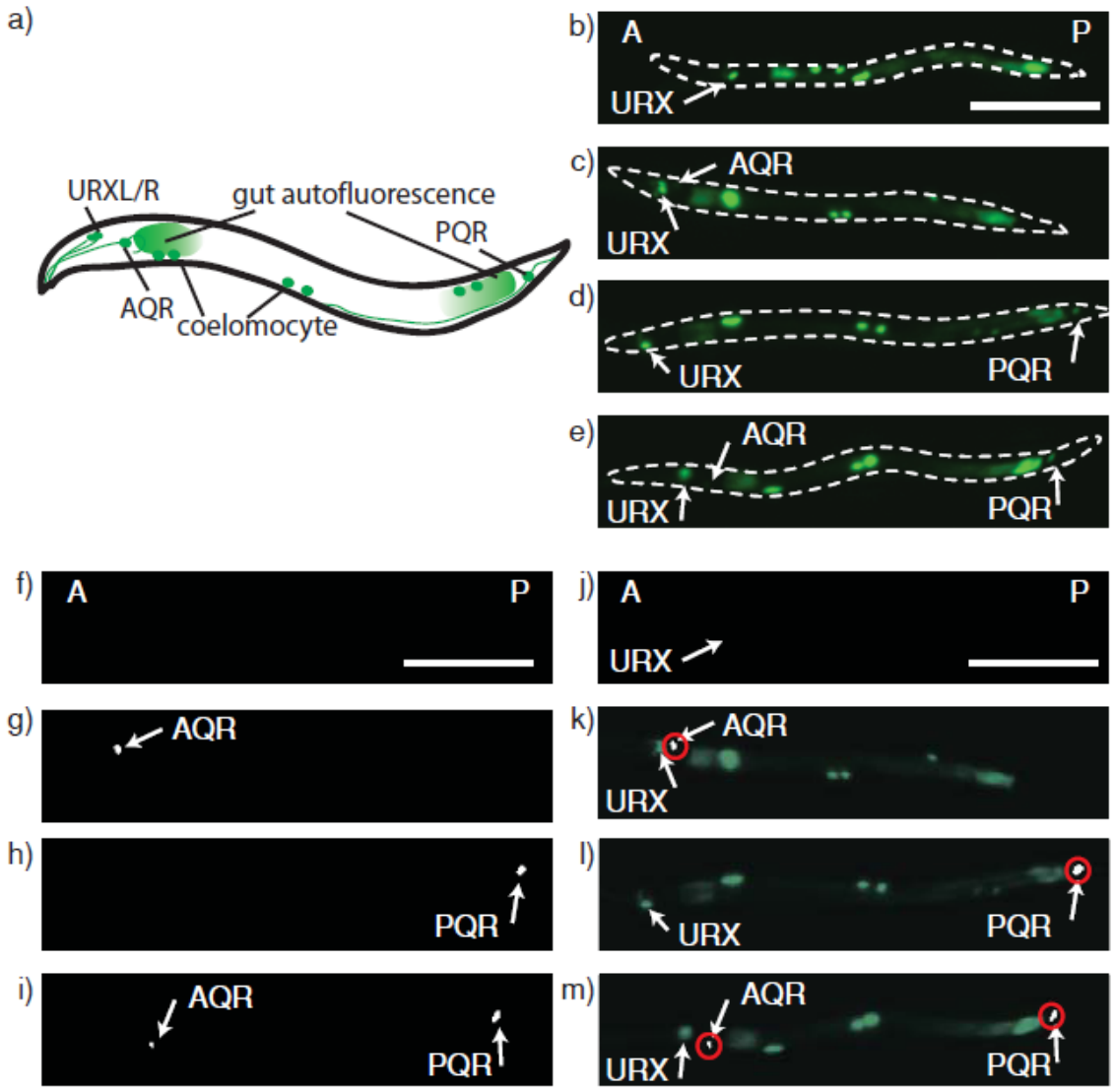

Figure 2.16. Automated analysis of gene-expression pattern in the integrated microsystem. a) Schematic of the fluorescent regions including expressions of multiple GFP transgenes and autofluorescence from the gut. (b-e) Representative images showing stochastic expression of reporter genes *kyIs342 [pgcy-32::tax-4::GFP, punc-122::GFP]* in wild-type. b) GFP in URXL/R only; c) GFP in AQR and URXL/R; d) GFP in PQR and URXL/R; e) GFP in AQR, POR, and URXL/R. (f-i) Processed images showing the identified neurons, distinct from other fluorescence signals. (j-m) Overlay of the raw images (b-e) and the processed images (f-i).

We sorted the worms based on classification of the PQR expression pattern. We collected two populations: one identified by the software as having GFP expression in PQR (on) and one identified as without GFP expression in PQR (on) and one identified as without GFP expression in the cell (off) (Table A.1). The worms were sorted at a speed of ~ 900 worms/h; both the loading and the image acquisition were rapid and entirely automated. Over 90 % of worms were loaded into the observation chamber within 1 sec after the previous worm exited (Fig. 2.17b; n ~ 8,200). The false positive and false negative rates of sorting were low (Table A.1). In addition, because the worms remained at room temperature with no exposure to anesthetics, there was no concern about the alteration of the expression pattern, and it was possible to collect and reimage the worms at a later time. This mode of operation of our system can be adapted for several types of studies using transgene reporters, for instance, the analysis of promoter activities and of genetic interactions.

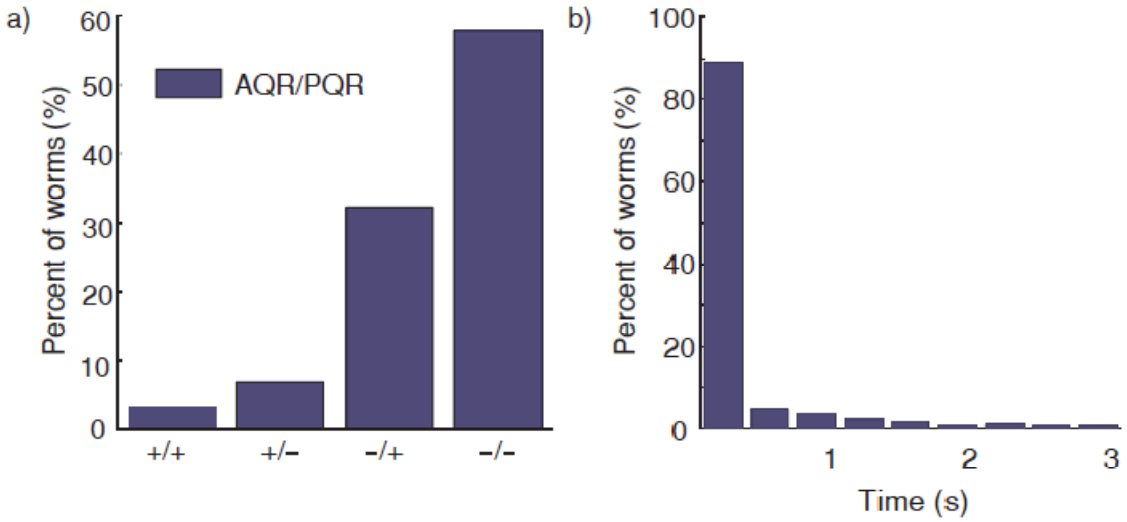

Figure 2.17. a) Percentage of animals with each of the four possible expression patterns of GFP in AQR and PQR. b) Histogram of animal loading time into the observation chamber (n ~ 8200) showing about 90 % worms were loaded within 0.33 sec.

2.6.2 Phenotyping and sorting based on synaptic features

As biological understanding advances, genetic screens are becoming increasingly more difficult to perform because the phenotypes of interest are becoming subtler. For example, many of the synaptic or other subcellular reporters exhibit features that are sub-micron in size, and reporters for these features are dim and easily photobleached. Thus, not only is manual phenotyping often too slow, but it is also often not precise or objective enough to detect quantitative changes. Using our automated system, we eliminate the need to seek the targeted region in the sample, therefore greatly reducing exposure time and the extent of photobleaching. Moreover, automated on-line image processing can phenotype animals more accurately and at greater speed, and synaptic features sensitive to the application of anesthetics can be examined in our system by applying cooling instead.

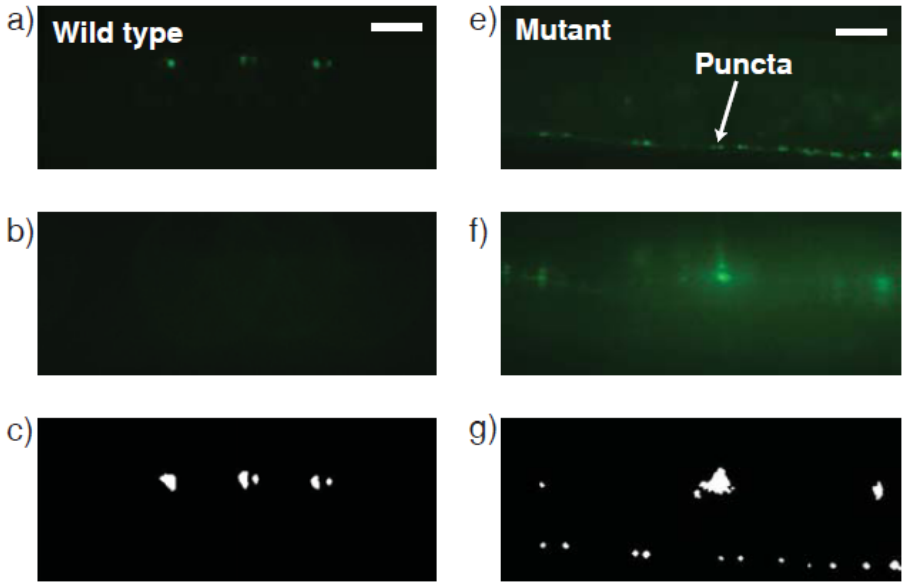

Figure 2.18. Automated high-throughput microscopy and sorting based on synaptic marker phenotypes. (a, b, and e, f) Representative images of punc-25-YFP::RAB-5 reporter expression in animals at two focal planes 20 microns apart. (a, b) Wild-type. (e, f) *unc-16* mutant. (c, g) Processed images from the corresponding animals to find puncta along the nerve cord and cell bodies. Mutants have puncta structures along the nerve cord, which were the basis for sorting.

To demonstrate the ability to screen based on subcellular changes, we performed a sorting experiment using strains carrying an integrated reporter transgene *juIs198 [punc-25-YFP::rab-5]*, which is expressed in the GABAergic motorneurons and labels a subset of synaptic endosomes[87]. In the wild-type background, YFP::RAB-5 is faint in the nerve cord (Fig. 2.18a), but *unc-16*$^{-/-}$ mutants have increased marker intensity along the nerve cord (Fig. 2.18e) (Heather Brown and Yishi Jin, personal communication), which is a major feature we used for sorting. Age-synchronized mixed populations were sorted according to their synaptic marker phenotypes at a rate of ~ 400 animals per hour. Cooling efficiently immobilized the animals, which enabled subcellular resolution. We used on-line image processing (Fig. 2.18c, g) to identify correctly the puncta along the nerve cord. To verify the sorting accuracy, we manually analyzed the sorted animals by the recorded images and by examining uncoordinated behavior. Table A1 bottom shows sorting results for each of the three trials; the overall sorting accuracy (total correctly sorted over total animals sorted) was 96.5% for a single round. All animals receive the same handling in the automated microsystem and images are analyzed uniformly using the same criteria, thus reducing noise and biases that may be introduced by manual operation.

2.7 Conclusions

The use of our automated microsystem for microscopy, phenotyping, and screens provides several obvious advantages. It is fast, allowing processing of large numbers of animals for genomic-scale studies. Photobleaching of fluorescent markers and other artifacts due to human handling are minimized by avoiding "feature seeking" steps. Brief cooling to immobilize animals provides an alternative to anesthetic drugs, allowing repeated imaging of the same animals over time. Our system is microscope- and camera-

independent; it is compatible with all typical microscopy set-ups in biology laboratories, e.g. confocal or two-photon microscopy, simple epifluorescence microscopy, or even stereo microscopy. Because the add-ons to already existing microscopy tools only include the microchip, some simple commercially available parts, and widely used software such as Matlab, the system is very inexpensive to replicate. In addition, tailored complex image-analysis routines for specific screens can be integrated because the control algorithm is modular. To adapt the system for *C. elegans* of different sizes as well as for other small organisms (e.g. *Drosophila melanogaster* and *Danio rerio* embryos), one would need to simply change the geometry (e.g. height and length) of certain parts of the chip, while using the same basic features and functions. Similarly, re-tuning the software modules (e.g. intensity and size thresholds) should be straightforward. This customizability provides our system with a wide range of applications.

Compared to manual phenotyping and screening experiments that typically require many months to complete, our system without further optimization can already perform such experiments without human intervention in a few days to a few weeks, depending on the complexity and subtlety of the phenotypes. More importantly, this microsystem and the automation should allow rapid complex genetic screens based on subtle phenotypes that would be otherwise difficult or impossible to detect. For example, human eyes are imprecise at detecting absolute changes in brightness; by using our system, one can potentially screen for mutants that have altered intensity of reporters or that have slightly altered morphology. In gene expression analysis, we can also drastically improve the quality of expression pattern data due to the less subjective nature of our approach. Compared to the only commercial automated sorting system, COPAS, our system has much higher optical resolution and therefore a much expanded repertoire of applications. Additionally, due to the modular nature of our system, a wide variety of supplementary devices could be incorporated in series with it to fulfill additional needs,

e.g. administering small molecule libraries to distinct populations in advance of screening for pharmacological studies.

In summary, our method for high-throughput and high-resolution microscopy and phenotyping could eliminate a significant bottleneck in genetic analyses and enable large-scale quantitative experimentation in developmental biology, functional genomics, network biology, and other related fields. In addition, the flexible and modular nature of our hardware and software systems also allow coupling with pharmacological studies, laser ablations, and behavioral studies, as well as being adaptable to other genetic model organisms.

CHAPTER 3

AN AUTOMATED MICROSYSTEM FOR HIGH-THROUGHPUT CELL LASER ABLATION

3.1 Overview

Laser ablation is an established tool for studying cells' roles during development and behavior, but its use has been limited due to the manual and low-throughput nature. We demonstrate here a technique combining multiplexing microfluidic manipulation of embryos/L1-stage *C. elegans* and software for image processing and automation, allowing for high-throughput cell ablations. Large numbers of neuron-ablated and age-synchronized animals showed defects in chemotaxis avoidance behavior in a population assay.

3.2 Integrated microsystem overview

A nitrogen laser that emits pulsed light at a wavelength of 337 nm with output pulses of 4 nanoseconds (VSL-337ND-S, Spectra-Physics) was integrated to the system described in the previous chapter (Fig. 3.1). Embryos suspended in a buffer solution are introduced into the microfluidic device by pressure driven flow and trapped in the embryo trap module. After two hours of incubation at room temperature hatched L1 worms are delivered to the laser ablation module. A Matlab algorithm (Appendix D) actuates macrovalves to control microvalves integrated on chip for loading/deloading one animal at a time. Local cooling formed by circulating coolant through the device instantaneously immobilizes the loaded worm. The Matlab program then acquires 3D volume images from the CCD camera at a variety of focal planes by manipulating the x-y-z-stage. These 3D images are processed automatically to identify center of target

neurons. The program then moves the motorized stage to center the laser on the neuron and triggers the laser firing. The entire cycle repeats automatically.

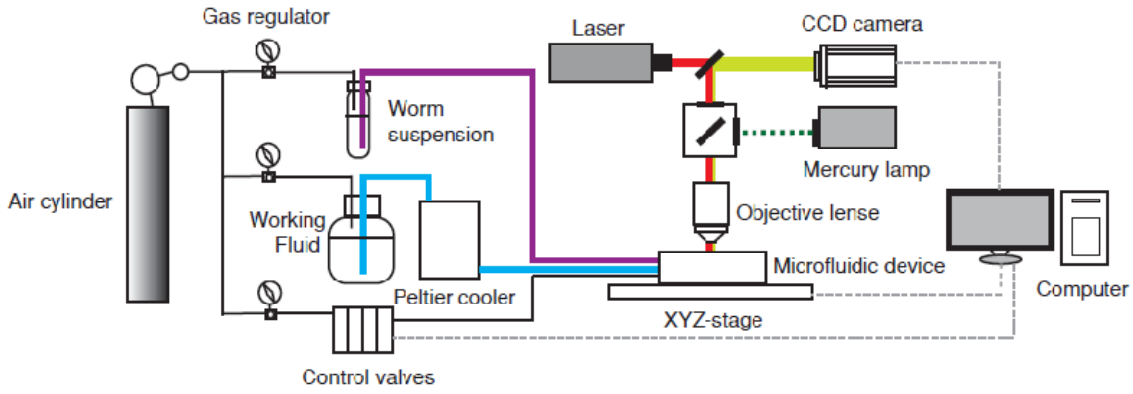

Figure 3.1. System block diagram showing the on-chip and off-chip components.

3.3 Microfluidic device

3.3.1 Microfluidic device fabrication

The microfluidic device consists of three PDMS (Sylgard 184, Dow Corning) layer was fabricated using multi-layer soft lithography. Three different molds were first fabricated by photolithographic processes to create the worm loading layer, the control layer, and the cooling layer. The mold for the worm loading layer was made by a two-step photolithographic process. In the first step, a 15-µm-thick negative photoresist (SU8-2010, Microchem) was spin-coated onto a silicon wafer for the laser ablation module (Appendix Ea). The embryo trap module was then fabricated with a 60-µm layer of negative photoresist (SU8-2025, Microchem) on the same wafer (Appendix Eb). The master for the control layer was made of a 10-µm layer of negative photoresist (SU8-2010, Microchem) on a silicon wafer (Appendix Ec). The master for the cooling layer was made of a 150-µm layer of negative photoresist (SU8-2100, Microchem) (Appendix

Ed). The three molds were treated with tridecafluoro-1,1,2,2-tetrahydrooctyl-1-trichlorosilane vapor (United Chemical Technologies) in a vacuum desiccator to prevent adhesion of PDMS during the molding process.

For fabricating the PDMS device, mixture of PDMS (A and B in 10:1 ratio) was poured onto the cooling-layer master to obtain a 5 mm-thick layer. Mixture of PDMS (A and B and THF in 20:1:5 ratio) was spin-coated on a control-layer master to give a 20-μm-thick layer. Mixture of PDMS (A and B in 5:1 ratio) was spin-coated on a worm-loading-layer master to give a 60-μm-thick layer. The three layers were partially cured at 70 ºC for 20 min. The cooling layer was then peeled off from the master and bonded to the worm loading layer. This assembled layer was cured at 65 ºC for 15 min and peeled off. The assembled layer was then bonded to the control layer and fully cured at 70 ºC for 2 hours. The assembled PDMS with three layers was peeled off and holes were punched. These assembled layers were then bonded onto the cover glass to form the micro device.

3.3.2 Microfluidic components of the engineered microchip

In order to perform high-throughput laser ablation, the microfluidic device needs to execute following tasks; 1) to provide large number of age-synchronized first larval (L1) stage worms, 2) to load/unload the animals in a high-throughput manner, 3) to immobilize the movement of a loaded worm and pumping of the pharynx to ensure successful ablation. The microdevice we designed has several key features necessary to perform these tasks.

The device consists of the embryo trap and laser ablation modules (Fig. 3.2). The embryo trap module consists of array of 2,000 embryo traps and provides up to 2,000 age-synchronized L1 worms to the laser ablation module. The traps have a unique geometry allowing single embryos to be trapped while releasing hatched L1 worms (Fig.

3.3). A gap of 14-µm allows a fraction of fluid carrying embryos to enter a trap. Once an embryo is trapped and partially blocks the gap, the fraction of fluid entering the trap region is reduced[88, 89]. This allows single-embryo trapping. Once the embryo hatches, the L1 worm with small width (~ 12 µm) can be released through the gap.

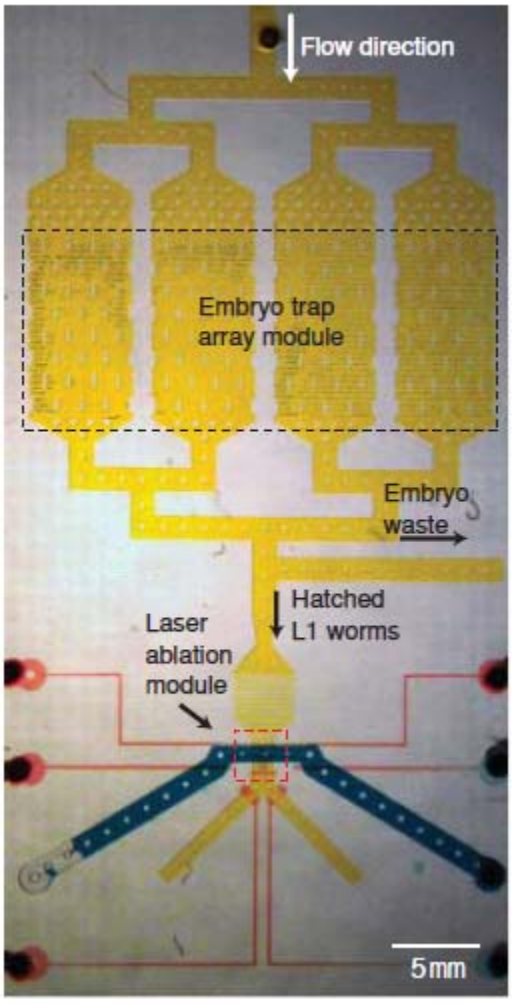

Figure 3.2. Dye-filled image of the device: sample channel (yellow), valve control channel (red), and temperature control channel (blue).

Embryos isolated by bleaching gravid adults and suspended in buffer are introduced to the trap module after incubation at 20 °C. After further incubation on chip, many embryos hatch (Fig. 3.4**)** and these well-synchronized L1s are then delivered to the laser ablation module. Compared to manually picking individual animals, this process is

easy and requires much less time. Additionally, the embryo trap module also functions to remove dust particles from embryo/L1 suspension such that the ablation device can operate robustly without clogging of the small channel features; big dust particles are filtered by the array and small dust particles go to the waste in the embryo loading step.

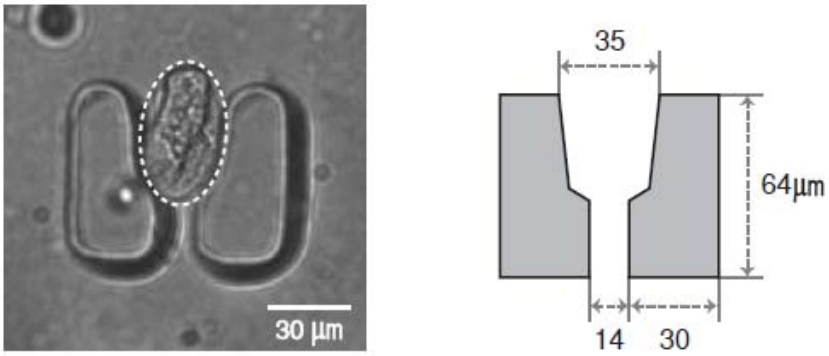

Figure 3.3. Geometry of an individual embryo trap design.

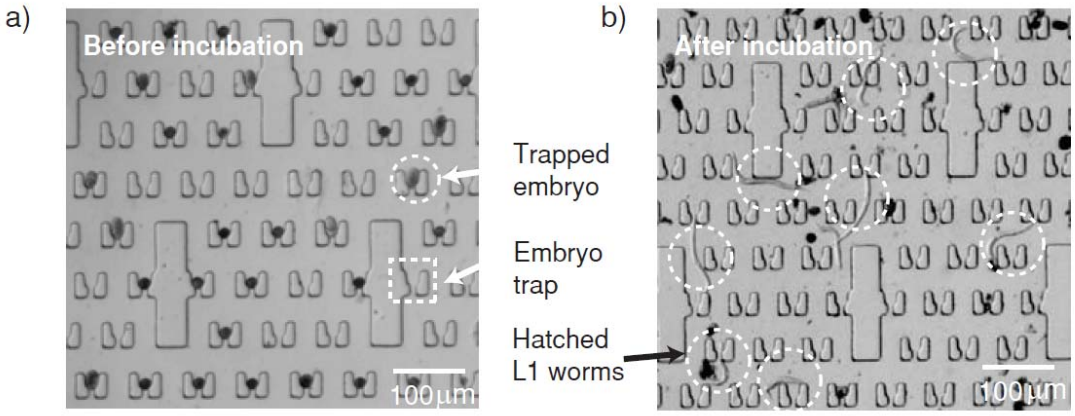

Figure 3.4. a) Bright field image of the embryo trap array showing embryo traps and trapped embryos. b) Hatched L1 worms in the embryo trap chamber after incubation of the trapped embryos for two hours.

The laser ablation module is optimized for automated operation and has several unique features to maximize throughput (Fig. 3.5). This module is capable of processing multiple worms in parallel without substantially increasing the complexity of the control requirements. It has two sets of worm-loading channels that operate in parallel, allowing

worm-loading and -exiting at one set while simultaneously performing imaging and laser ablation in the other set. L1 worms are directed to the loading channels by pressure driven flow from the embryo trapping module, and are positioned by restriction structures in the loading / ablation channels (Fig. 3.5). The loading channel geometry makes it difficult for a second worm to enter, and the presence of a worm in the loading channel also diverts upstream worms towards the empty channel[81]. Once a worm is loaded, the loading regulator and resistance regulator are closed to further increase the hydrodynamic resistance and thereby reduce buffer flow that can cause movement of the loaded worm. To unload the worm, the restriction valve is open while the loading regulator is closed, which assures releasing of the single processed worm. This parallel processing of worms significantly increase throughput because the time required for loading/unloading process does not contribute to the effective processing time.

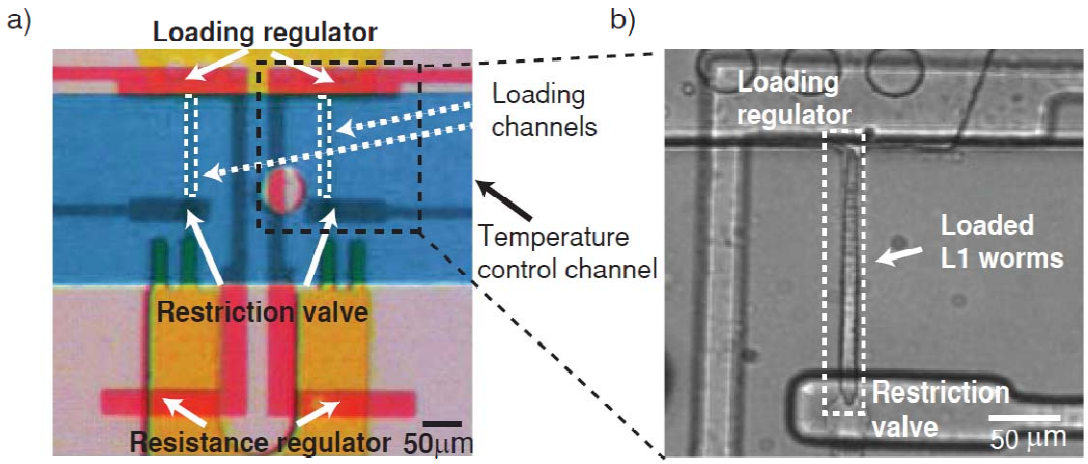

Figure 3.5. Optical micrographs of the microfluidic device and its operation. a) Dye-filled image of the device: sample channel (yellow), valve control channel (red), and temperature control channel (blue). b) A loaded worm in the loading channel.

For automated laser ablation, it is crucial that worms remain completely still for the duration of imaging and targeting of the neurons and firing the laser, because any

movement or drift can cause inaccurate targeting of the neurons. Body movement and pharyngeal pumping are sources of such movements. We use cooling to immobilize worms; it has several important advantages over other immobilization techniques for automated cell laser ablation[77-79, 81, 90]. First, cooling is the only method to stop activity of pharynx besides using anesthetics. This is particularly important because many sensory and inter-neurons of interest are near the pharynx. Second, cooling does not cause deformation of the animal's body, which may change the relative anatomical position of the neurons. Therefore, internal anatomical information of cells can be used for image processing algorithm to distinguish target cells from other cells or auto-fluorescent fat granules in the intestine. Third, immobilization by cooling is instantaneous and reversible, which allows rapid manipulation of worms.

3.3.3 Microfluidic device operation

Embryos obtained by bleaching adult worms were suspended in 8 wt% dextran solution and introduced to the embryo trap module by a pressure driven flow. After loading embryos filtered M9 solution containing 0.5 wt% BSA was introduced to exchange the dextran solution and further remove dust particles. After incubation for 2 hours in the trap module hatched L1 worms were delivered to the laser ablation module.

In laser ablation module, both positioning valves are partially closed for loading (Fig. 3.6). In order to perform laser ablation in the left loading channel valve 3 and 5 are partially closed to minimize flow through the left loading channel while valve 4 and 6 are open to load a worm in the right loading channel. After laser ablation of the worm loaded in the left loading channel the positioning valve 1 is open to release the ablated worms. The loading regulator (valve 3) remains closed to prevent non-ablated worms in upstream from exiting. Meanwhile, the x-y-z-stage moves to the right loading channel to process a loaded worm. The animal in the right loading channel is then ablated while another

worm is loaded in the left loading channel. After ablation, positioning valve 2 is open to release the ablated worm. In the meantime, a worm in the right loading channel is processed. This parallel processing significantly reduces the effective ablation time per animal.

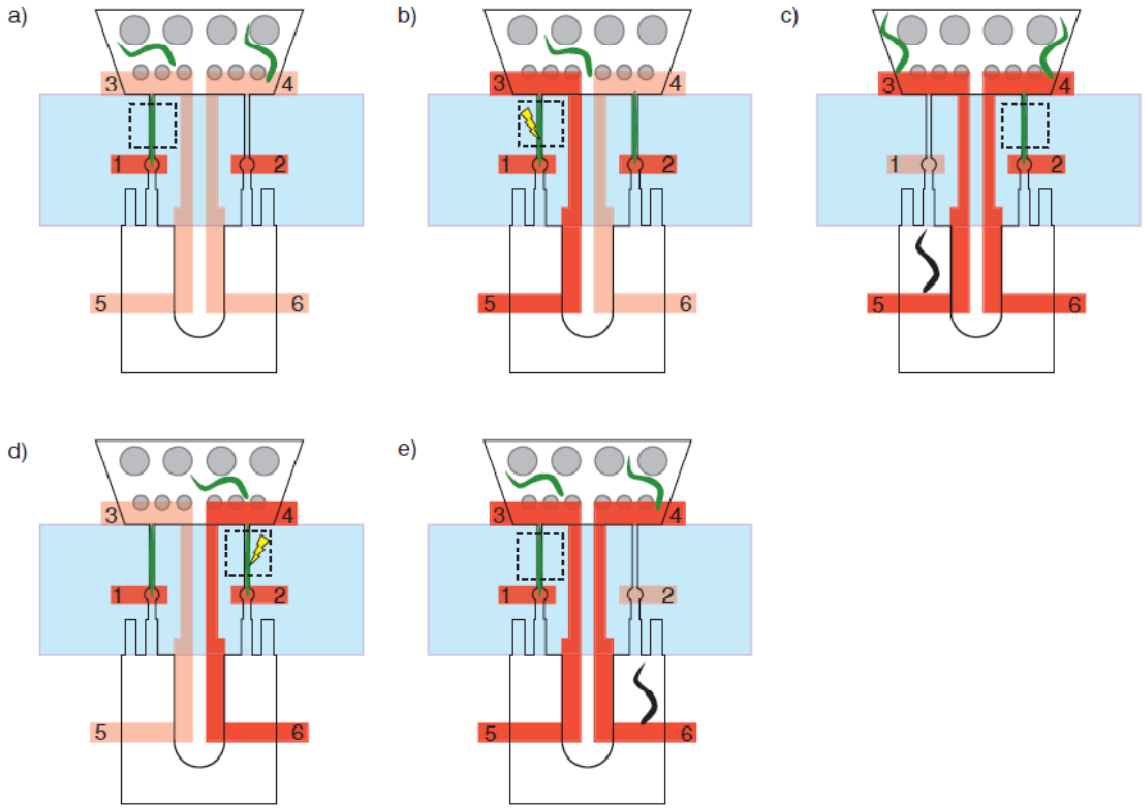

Figure 3.6. Schematic diagrams summarizing the valve control sequence of the laser ablation module. Valve 1, 2: positioning valves, Valve 3, 4: loading regulators, Valve 5, 6: resistance regulators. Blue, cooling channel; bright red, valves in open position, dark red, valves in partially closed position; green worms, animals before ablation, black worms, animals after ablation; dashed square, field of view of the camera. a) Both loading channels: worm loading. b) Left loading channel: ablation, right loading channel: worm loading. c) Left loading channel: unloading, right loading channel: ready for ablation. d) Left loading channel: worm loading, right loading channel: ablation. e) Left loading channel: ready for ablation, right loading channel: unloading.

3.4 System control, image acquisition, and image processing

To ablate neurons automatically, we use image processing (Fig. 3.7) guided by heuristics such as anatomical information of the neurons in the worms (Fig. 3.8). Once the worm is immobilized in the loading channel, sparse z-stack (2-μm steps) was acquired with 100X oil-immersion objective (NA = 1.4) using Hamamatsu C9100-13 EM CCD camera (512×512 pixels). The z-stack was then flattened by computing the standard deviation of pixel in the x-y plane along the z-direction. The flattened image was filtered via a spatial bandpass filter to remove random noise[91]. A threshold was subsequently applied to the processed image to identify all local maxima, which included the target neurons and auto fluorescent fat granules in the intestine. The target neurons were then distinguished from the fat granules based on a number of features such as relative distances between objects, position of the objects, and size. The software then calculates their x-y-z coordinates. The x-y-z stage then moved to pre-aim the center position of the two neurons. A denser z-stack (0.5-μm step size) was subsequently obtained and similarly processed to identify x-y-z coordinates of center of the neurons. The program then moved the stage to center on the neuron and triggers the laser firing. To verify the accuracy of the image processing, worm images before and after laser firing were saved. The entire cycle takes 15 seconds when we ablate two neurons, where the majority time is spent by the travel of the x-y-z stage. This automated cell-identification and laser firing process is an essential element of the microsystem to achieve high-throughput cell ablation with a high degree of accuracy and uniform treatment of the sample.

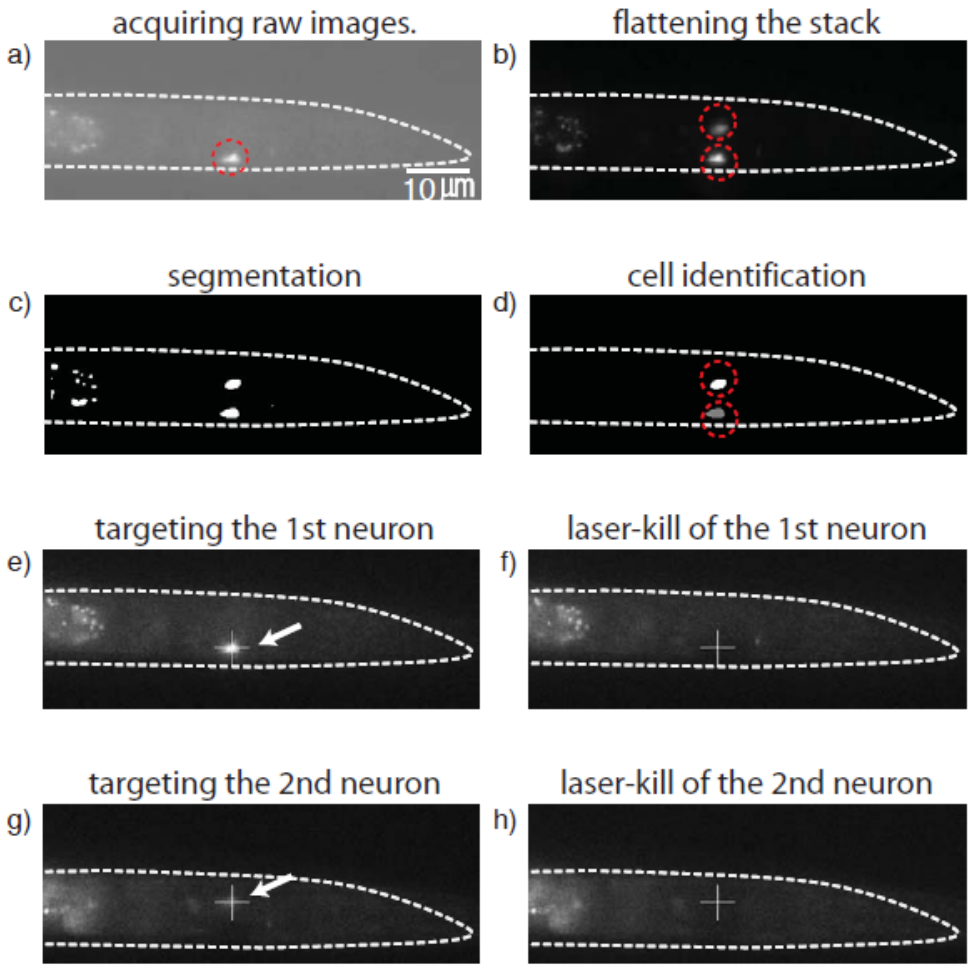

Figure 3.7. Process of the automated imaging process (a-d) and laser ablation (e-h). a) One frame from the z-stack fluorescent image showing the in-focus neuron (red circle). b) Flattened z-stack image showing two neurons (red circle). c) Thresholded image showing the two neurons and fat granules. d) Processed image showing identified neurons with the fat granules automatically removed. e) Moving the target neuron to the laser focal point. f) After laser firing: the target neuron is no longer visible in fluorescent image. g) Before laser firing on the second neuron. h) After laser firing on the second neuron.

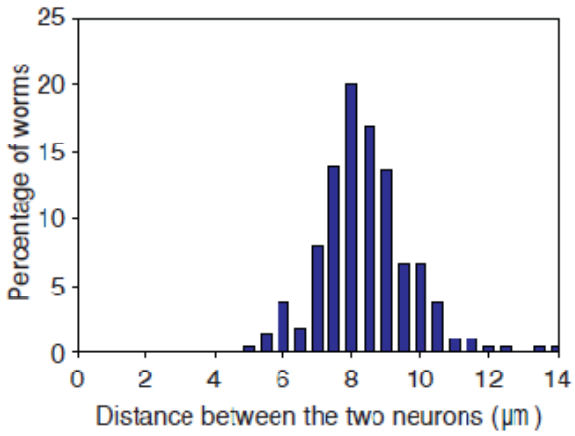

Figure 3.8. Calculated distance between the two neurons of ablated worms by the image processing algorithm. Internal anatomical information of cells including relative distance was used to distinguish the target neurons from auto-fluorescent

3.5 Results

3.5.1 Laser ablation of *C. elegans*' olfactory neurons

To demonstrate the capability of this system, we ablated animals with the olfactory neurons AWBL/R expressing green fluorescent protein (GFP) at a rate of up to 110 worms per hour to generate enough worms for a population behavior assay. Typically population-based assay requires at least 50 ~ 100 age-synchronized worms per assay and multiple repeats[92]. Traditional manual laser ablation method cannot provide such a large number of animals, while genetically mediated cell disruption using cytotoxic genes does not necessarily eliminate the target neurons completely and efficiently and may complicate interpretation of behavior data. For instance, animals expressing the degenerin gene *mec-4(d)* in AWB showed diminished avoidance, but it was unclear whether the residual avoidance is due to residual AWB function or to the contribution of other sensory neurons[14]. Using our automated system, we ablated ~ 350 pairs of AWB neurons to generate enough animals for the behavior assay.

In order to diminish the animals' ability to sense 2-nonanone, both neurons have to be correctly ablated. Our image analysis algorithm can successfully distinguish the target cells from auto-fluorescent fat granules (Fig. 3.7) using anatomical information of the neurons (Fig. 3.8). The cell-identification algorithm was 99% correct in targeting cells (verified by the images recorded for laser ablation). Successful ablation was confirmed by looking for *Pstr-1::gfp* expression ~ 2 days after the ablation.

3.5.2 Chemotaxis assays

We performed 2-nonanone chemotaxis assays with populations of worms. Population chemotaxis assays were performed similar to those described in Troemel *et al.* Briefly, well-fed young adult animals were placed on the center of a plate. Two spots with 1µl of 2-nonanone in ethanol (1:4) were spotted on one side and ethanol alone were spotted on the opposite side of the plate to establish a concentration gradient of the avoidant from the point source in the plate. Animals at each section were counted after 1hr and an avoidance index was calculated as (A+B-E-F) / (A+B+C+D+E+F) where A is the number of animals on the section A (Fig. 3.9a).

Compared to both control animals (i.e. those not handled in micro device and not ablated) and mock-ablated animals (i.e. those handled in micro device but without laser firing), AWB-ablated animals exhibited greatly diminished avoidance of the volatile repellent (Fig. 3.9b), confirming that AWB neurons contribute to avoidance of 2-nonanone. However, residual 2-nonanon avoidance suggests that other sensory neurons may also detect this repellent. These results show that our system can be used to perform automated ablation to provide a large number of ablated animals for understanding neurons' roles in behavior.

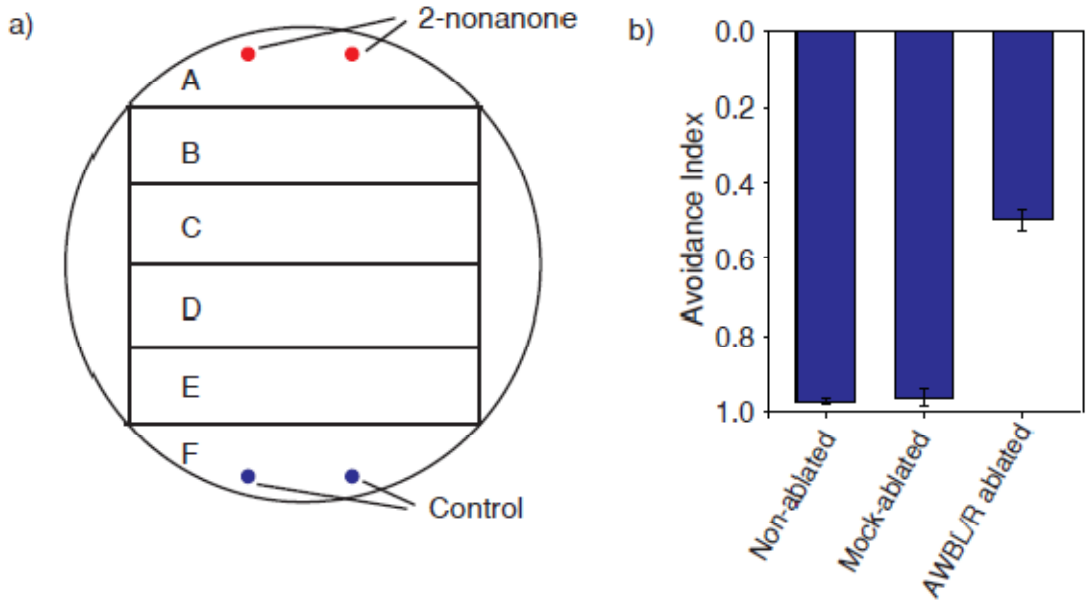

Figure 3.9. a) Avoidance population assay. Animals are placed in the center of the plate and animals at each section are scored based on their final position after one hour. 2-nonanone was diluted four times with ethanol. Control: ethanol. b) 2-nonanone chemotaxis response of AWBL/R ablated, mock ablated, and control animals. AWBL/R ablated worms have defects in 2-nonanone avoidance behavior. Each data point represents the average of at least five independent assays. Error bars indicate the standard error of the mean (SEM).

3.6 Conclusions

The unique features of our microsystem enable high-throughput cell microsurgery: The embryo trap module of the microdevice provides a large number of age-synchronized L1 worms while filtering out dust particles; Multiplex processing of the animals in the laser ablation module significantly increases the throughput; Cooling stops body and pharynx movement for accurate aiming and ablation of the target neurons; Automation of image processing and laser firing allows even treatment of worms and thereby minimize sample-sample variation. Compared to manual method that occurs at a rate of a few animals per hour, our system can perform ablation of hundreds of worms per hour. Moreover, the success rate and the throughput don't suffer as the number of the

neuron required to be ablated increases because of complete automation of the entire process.

Using other cell-specific markers, it is easy to adapt the system to ablate other cells for large-scale systematic studies in many other contexts, such as development. This system can also be coupled with other lasers to perform, for example, laser surgery on subcellular structures. Moreover, we believe this system could be used as an imaging tool for *C. elegans* from embryo to L1 stage.

CHAPTER 4

THREE-DIMENSIONAL *IN SITU* TEMPERATURE MEASUREMENT IN MICROSYSTEMS

4.1 Overview

Temperature control in the microsystems for imaging and ablation of *C. elegans* is critical. This chapter describes an *in situ* method for three-dimensionally resolved temperature measurement in microsystems. The temperature of the surrounding fluid is correlated from Brownian diffusion of suspended nanoparticles. We use video-microscopy in combination with image analysis software to selectively track nanoparticles in the focal plane. This method is superior with regards to reproducibility and reduced systematic errors since measuring Brownian diffusivity does not rely on fluorescence intensity or lifetime of fluorophores. The efficacy of the method is demonstrated by measuring spatial temperature profiles in various microfluidic devices that generate temperature gradients and by comparing these results with numerical simulations. We show that the method is accurate and can be used to extract spatial temperature variations in three dimensions (3-D). Compared to conventional methods that require expensive multi-photon optical sectioning setups, this technique is simple and inexpensive. In addition, we demonstrate the capability of this method as an *in situ* tool for simultaneously observing live cells under the microscope and monitoring the local temperature of the cell medium without biochemical interference, which is crucial for quantitative studies of cells in microfluidic devices. This chapter covers background, mechanisms of 2-D/3-D temperature measurement, design of the devices for generating temperature gradients, numerical models for simulating temperature distributions in the devices, and experimental results. This work is done in collaboration with Jaekyu Cho in

Dr. Victor Breedveld's group. Jaekyu developed the particle tracking algorithm. This chapter is adapted from Reference 93.

4.2 Introduction and background

4.2.1 Motivation

As described in previous chapters, we used on-chip cooling to completely immobilize *C. elegans* for high-resolution microscopy and laser ablation. At present, cooling is the only method to completely stop worm's movement, besides using anesthetics. Moreover, immobilization by cooling is instantaneous and reversible, thus making it an attractive tool for high-throughput applications. Cooling temperature, however, needs to be accurately controlled (~ 4 ºC) for proper immobilization while minimizing its potential side effects.

In our microsystems, on-chip cooling is achieved by integrating the cooling channel underneath of the worm loading channel and circulating the coolant through the channel to cool down the detection zone. Temperature that a loaded worm experiences is determined by many experimental factors, such as thickness of the membrane in between the layers, flow rate and temperature of the coolant. These experimental conditions can be simulated using a numerical model to estimate the temperature, as described in Chapter two. However, discrepancies between the predicted temperature and the actual temperature often exist due to uncertainties in model parameters and slight geometric differences between the actual devices and the model. Therefore, it is critical to experimentally measure the actual temperature in order to confirm proper device operation and aid further system optimization.

Besides the application stated above, the ability to control and measure temperature inside microfluidic devices is also critical for many other microfluidic applications since temperature often affects biological or chemical processes[30, 38, 79, 94-97]. For instance, precise temperature control over time and/or space is essential for on-chip amplification of DNA sequences by Polymerase Chain Reaction (PCR)[30]. In another case, a strong temperature-dependence and stringent regulations of the embryonic development of *Drosophila melanogaster* was demonstrated using a microfluidic device that generates a temperature differential across the embryos[38]. Besides controlling biological processes, temperature also plays a role in device functions. Numerous studies have demonstrated the importance of temperature effects in capillary electrophoresis systems[94-97]. For instance, temperature gradients in electrophoresis capillaries have long been understood to cause band spreading that reduces separation efficiency[97]. Thus, a reliable on-chip temperature measurement method is essential to design and operate microsystems effectively.

4.2.2 Limitations of existing technology

To address the need of temperature measurement in microsystems, many temperature measurement methods in microsystems have been developed. The common solution is to use microfabricated thermocouples for temperature measurement in microfluidic devices[98-100]. However, this approach constrains the measurements to specific fixed positions in the microdevices. As an alternative to microfabricated thermocouples, spectroscopic methods can provide temperature measurements with sub-micron spatial resolution by taking advantage of the temperature dependence of material

properties of chemicals[101-107]. For example, thermochromic liquid crystals (TLC) have been successfully used as thermal probes[105, 108], but the high viscosity of TLCs limits their applications[105]. Fluorescent dyes are another class of commonly used thermosensitive chemicals. Rhodamine-B, for example, has been broadly used because high spatial- and temporal-resolution can be achieved with fluorescence microscopy[104]. However, these measurements are based on the magnitude of fluorescence intensity, which can often be affected by environmental factors, such as uneven illumination from the light source, adsorption of Rhodamine-B on polymer-based microfluidic chip material, and photobleaching[103]. In particular, variations in excitation and detection efficiencies across the microscope field of view can hinder quantitative interpretation of the intensity data, making these dyes unsuitable for accurate temperature measurement without complicated calibration. To overcome some of the shortcomings of the intensity-based temperature measurement, ratiometric fluorescence techniques and fluorescence lifetime imaging can be made since the readout signal is independent of intensity[106, 107]. However, these techniques are often associated with specialized and expensive equipment.

Another critical drawback of these conventional techniques is that the addition of the probes could perturb device function[103, 109], or be potentially toxic to biological samples[110, 111]. It has been reported that organic small-molecule fluorescent dyes commonly used for temperature measurement can adsorb onto and diffuse into walls of polymer microfluidic chips[103, 109, 112]. In some instances, the adsorption of the charged dyes may alter surface chemistry of the microchannels, which results in unpredictable operation of electroosmotically pumped flow and electrophoretic separations[103, 109].

Chemical probes have also been reported to be toxic to biological samples[110, 111]. For example, Rhodamine-B inhibits the proliferation of human lip fibroblasts significantly, even at concentrations lower than that generally used for temperature measurements[111].

The adsorption and toxicity of the thermosensitive chemicals can sometimes be addressed by separating the probes from the samples[103, 105]. One approach is by using a thin PDMS membrane saturated with Rhodamine-B dye and sandwiching it between two glass substrates, thereby allowing temperature measurement in the presence of biological samples[103]. However, this temperature measurement is indirect due to the non-negligible thickness of the dye film and the glass substrate. Encapsulated beads of thermochromic liquid crystals also can be used for temperature measurements without altering the sample system[105]. The main drawback is that the encapsulated beads are typically tens of micrometers in size and are therefore impractical for use in micrometer-sized channel structures. As a result, in most studies that apply these methods, temperature profiles in microfluidic devices have been characterized without the actual devices in operation or without the presence of biological samples.

Since the presence of samples and the operation of integrated functional components can actually generate local temperature changes[47, 113], such temperature measurements do not accurately represent the actual temperature distributions. For example, it was found that the position and orientation of a *Drosophila* embryo affects the temperature distribution in the microfluidic device that was designed to generate temperature differential around the embryo[47]. In another example, dielectrophoretic cell separation causes Joule heating around electrodes and thus increases the local temperature, especially along the vertical dimension, which can lead to hyperthermic cell

damage[113]. Therefore, in order to optimize the design and the operation of microsystems effectively, it would be desirable to characterize temperature while the device is in operation without introducing artifacts to the measurements or toxicity to the samples.

4.3 Objectives of the work performed in this chapter

To address the need for non-invasive three-dimensional temperature measurement in microsystem, we developed a novel three-dimensional *in situ* temperature measurement method using the Brownian motion of nanoparticles with a simple and inexpensive videomicroscopy setup that fulfills the following goals: (1) spatial resolution as low as 1 ~ 2 μm in all dimensions; (2) overall accuracy of temperature measurement of less than 1 °C; (3) high reproducibility (less than 1 °C between measurements); (4) easy to use; (5) inexpensive.

4.4 Experimental methods

4.4.1 Fabrication of PDMS devices

The microfluidic devices used in this chapter were fabricated using multi-layer soft lithography[55]. Negative molds were fabricated by UV photolithographic processes using a negative photoresist (SU8-2050, Microchem, Newton, MA) (Appendix F). Patterned wafers were then treated with tridecafluoro-1,1,2,2-tetrahydrooctyl-1-trichlorosilane vapor (United Chemical Technologies, Bristol, PA) in a vacuum desiccator to prevent adhesion of PDMS (Sylgard 184, Dow Corning, Midland, MI) before the molding process. For all the PDMS fabrication processes, PDMS mixture of A and B in 5:1 ratio was used to minimize deformation of the PDMS structures while in device operation. For single-layer devices, PDMS mixture was poured onto the mold to

obtain a 5-mm thick layer and then fully cured at 70 °C for 2 hours. In the case of two-layer devices, PDMS mixture was spin-coated on the sample-channel mold to give a 100 μm-thick layer, which results in a 30 μm-thick PDMS membrane on top of the sample-channel. The same ratio of PDMS was poured onto the wafer mold for temperature-control channels to obtain a 5-mm thick mold. Each layer was partially cured at 70 °C for 5 min (sample-channel mold) or 20 min (mold for temperature-control channel). The thick control layer was then peeled off from the mold and bonded to the sample-channel layer. The assembled layers were then fully cured at 70 °C for 2 hours. After holes were punched, the PDMS devices were bonded onto either the cover glass or the slide glass depending on applications. In general, the devices in this study include several parallel channels: one channel for sample and one or two channels for temperature control. The sample channel and the temperature-control channels are either within the same layer or in different layers depending on required temperature gradient profiles.

4.4.2 Experimental setup and image acquisition

We used 250-nm radius carboxylate-modified polystyrene particles (FluoSpheres®, Invitrogen, Carlsbad, CA). Fluorescene particles were suspended in either DI water for calibration and temperature mapping, or in cell medium for *in situ* temperature measurements. Before every experiment, the particle suspensions were sonicated for ~ 30 min to get rid of aggregates. After sonication the particle suspension was introduced into the particle channels, after which the in- and outlets of the particle channels were sealed with solid metal pins to eliminate fluid convection. To create temperature gradients in the devices, hot and cold fluids were first generated by flowing DI water (for the hot fluid) and 30 wt % sodium chloride solution (for the cold fluid) off-chip through temperature-controlled copper tubing and then introduced into the temperature control channels via constant pressure-driven flows. Temperatures of the

copper tubing were controlled using a water-bath for the hot fluid and a Peltier cooler for the cold fluid. The flow rates of the hot and cold streams were set to be high enough (typically 5 ~ 10 ml/min) so that the temperature differences between inlet and outlet temperature of the streams were less than 1 °C.

The Brownian motion of fluorescent nanoparticles in the particle channels was monitored via optical Microscope (Leica DM-IRB) with a 63X air or 63X oil-immersion objective, and movies were captured using a CCD camera (Cohu, Poway, CA) at 30 frame/s and a resolution of 640 × 480 pixels. Subsequently the recorded movies were analyzed with software developed using Interactive Data Language (ITT Visual Information Solutions, Boulder, CO). Because Brownian motion leads to small particle displacements on these timescales and is highly sensitive to external vibrational noise, all experiments were performed on a vibration-isolated optical table.

4.4.3 Numerical models for heat transfer

The simulations of heat transport in the devices were performed using a commercial finite element package COMSOL (Stockholm, Sweden). The convection-conduction equation was used:

$$k\nabla^2 T + \rho C_p v \nabla T = 0 \qquad (1)$$

where T [K] is temperature, C_p [J kg^{-1} K^{-1}] is the heat capacity, ρ [kg m^{-3}] is the density, v [m s^{-1}] is the velocity vector, and k [W m^{-1} K^{-1}] is the thermal conductivity.

The actual three-dimensional geometries of the devices including the PDMS layers, the glass substrate, and air layer surrounding the devices were constructed. To reduce the number of mesh elements, the thermal conductivity of the upper part of the PDMS and the actual geometry were rescaled by the equation, $k_{PDMS} / L_{PDMS} = k'_{PDMS} / L'_{PDMS}$. Heat capacities of 1100, 4180, 835, and 1006 were used

for PDMS, DI water, glass, and air, respectively. Densities of 1030, 1000, 2225, and 1.205 were used for PDMS, DI water, glass, and air, respectively. Thermal conductivities of 0.17, 0.61, 1.4, and 0.025 were used for PDMS, DI water, glass, and air, respectively[114, 115].

The surface temperatures of the temperature control channels were set as an average of the inlet and outlet temperature of the fluids measured experimentally with a thermocouple (HH202A, Omega, Stamford, Conneticut). In all experiments the temperature difference between the inlet and the outlet was found to be less than 1 °C due to the high flow rates (5 ~ 10 ml/min) and low thermal conductivity of the PDMS. The temperature of the surface of the cover glass was also set based on experimentally measured values. The temperature was kept constant by air convection from a heating fan.

4.4.4 Cell culture

NIH/3T3 mouse embryonic fibroblasts (ATCC, Manassas, VA) were cultured according to standard ATCC protocols in Dulbecco's modified Eagle's medium (D-MEM with 4500 mg/L D-glucose, L-glutamine, and no sodium pyruvate, Gibco 11965, Invitrogen, Carlsbad, CA) in 5 % CO_2 and 37 ºC. The D-MEM was supplemented with 10 % v/v bovine calf serum (HyClone, SH30073, Logan, UT) and 1 % v/v antibiotic-antimycotic solution (100 IU/mL penicillin and 100 µg/mL streptomycin in 0.85 % saline, Gibco 15240, Invitrogen, Carlsbad, CA). Cells were detached from their culture dish using trypsin-EDTA solution (0.05 % trypsin and 0.2 g/L EDTA, Gibco 25300, Invitrogen, Carlsbad, CA). Once the cells are detached, excess D-MEM was added and the suspension was centrifuged. The supernatant was then aspirated, and the cells were re-suspended in fresh D-MEM to yield a density of ~ 1×10^6 cells/mL.

4.5 Results and discussion

4.5.1 Brownian motion of nanoparticles correlating to temperature

To overcome the limits of the current technology, we developed a novel 3-D *in situ* temperature measurement method using Brownian motion of nanoparticles with a simple and inexpensive videomicroscopy setup. The Brownian motion of nanoparticles suspended in a liquid is a result of random collisions by the constituent molecules. The random particle displacement can be quantified through the mean square displacement (MSD), a statistical measure of particle mobility that is related to diffusivity via the following equation:

$$< r^2 >= \frac{\sum_{i=1}^{n} (\Delta x_i^2 + \Delta y_i^2 + \Delta z_i^2)}{n} = 6D\Delta\tau \tag{2}$$

where D is the diffusivity of particles and $\Delta\tau$ is the observation time interval of each incremental three-dimensional displacement (Δx, Δy, Δz). Equation 2 assumes that the diffusion is isotropic and that there is no convective transport. The diffusivity of particles can be described by the Stokes-Einstein equation:

$$D = \frac{\kappa_B T}{6\pi\eta(T) r_p} \tag{3}$$

where d is dimensionality, k_B is Boltzmann constant, T is the absolute temperature of the fluid, r_p is the particle radius, and $\eta(T)$ is the viscosity of the fluid, which is generally a function of temperature[116]. Consequently, equations 2 and 3 can be combined to express MSD as a function of temperature:

$$< r^2 >= \frac{\kappa_B T}{\pi\eta(T) r_p}\Delta\tau \tag{4}$$

Therefore, by measuring the MSD of the suspended particle of known sizes, the surrounding liquid temperature can be easily determined.

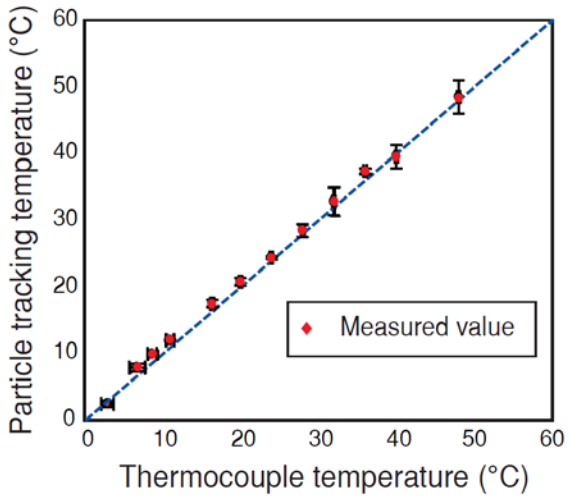

Figure 4.1. Comparison of temperature data from particle tracking with simultaneously measured thermocouple temperature; the dotted line representing perfect agreement between the two methods has a slope of 1.

To measure MSD of individual nanoparticles, about 10 seconds of movie of suspended particles were taken at 30 frames per second and processed using the modified particle tracking software[91]. We measured MSD of the nanoparticles for temperature ranging from 1 to 50 °C. The calculated temperature shows excellent agreement with the corresponding temperature measured by a thermocouple (Fig. 4.1), which is consistent with previously published data[116, 117]. As shown in Fig. 4.1, when using 500 nm (± 15 nm) particles, this method provides an overall accuracy of temperature measurement of less than 1 °C.

The advantage of temperature measurements using MSD is that the accuracy is not affected by spatial variations in excitation illumination and detection efficiency. This is because the particle tracking microscopy uses intensity contrast between particles and local background to locate the center of particles, and does not rely on quantitative analysis of fluorescence intensity, thus avoiding problems associated with

photobleaching. Moreover, the methodology is not limited to the fluorescence mode, it can equally well be used to images obtained in the differential interference contrast (DIC) mode. The calibration experiments thus show that this method provides accurate absolute temperature measurements with excellent robustness, independent of experimental conditions.

4.5.2 Mechanism of 3-D temperature mapping

Previously Bennigner *et al.* described a spectroscopic method using temperature sensitive chemicals to map 3-D temperature profiles[106]. Although elegant, this method requires a multi-photon optical sectioning setup to provide 3-D data stacks and also to eliminate out-of-plane fluorescence that could skew the observed temperature distributions. While this method offers high resolution and accuracy, microscopes with the multi-photon optical sectioning setup are at least an order of magnitude more expensive than conventional microscopes. In contrast, we provide a method for 3-D temperature mapping with a simple and inexpensive video-microscopy setup. This can be achieved by using the software algorithm that distinguishes in-focus particles in dense particle suspension with the presence of significant amount of out-of-focus fluorescence. By selectively tracking the in-focus particles, temperature of the focal plane can be measured. Therefore, 3-D temperature maps can be obtained by measuring temperature from a series of images at different focal planes.

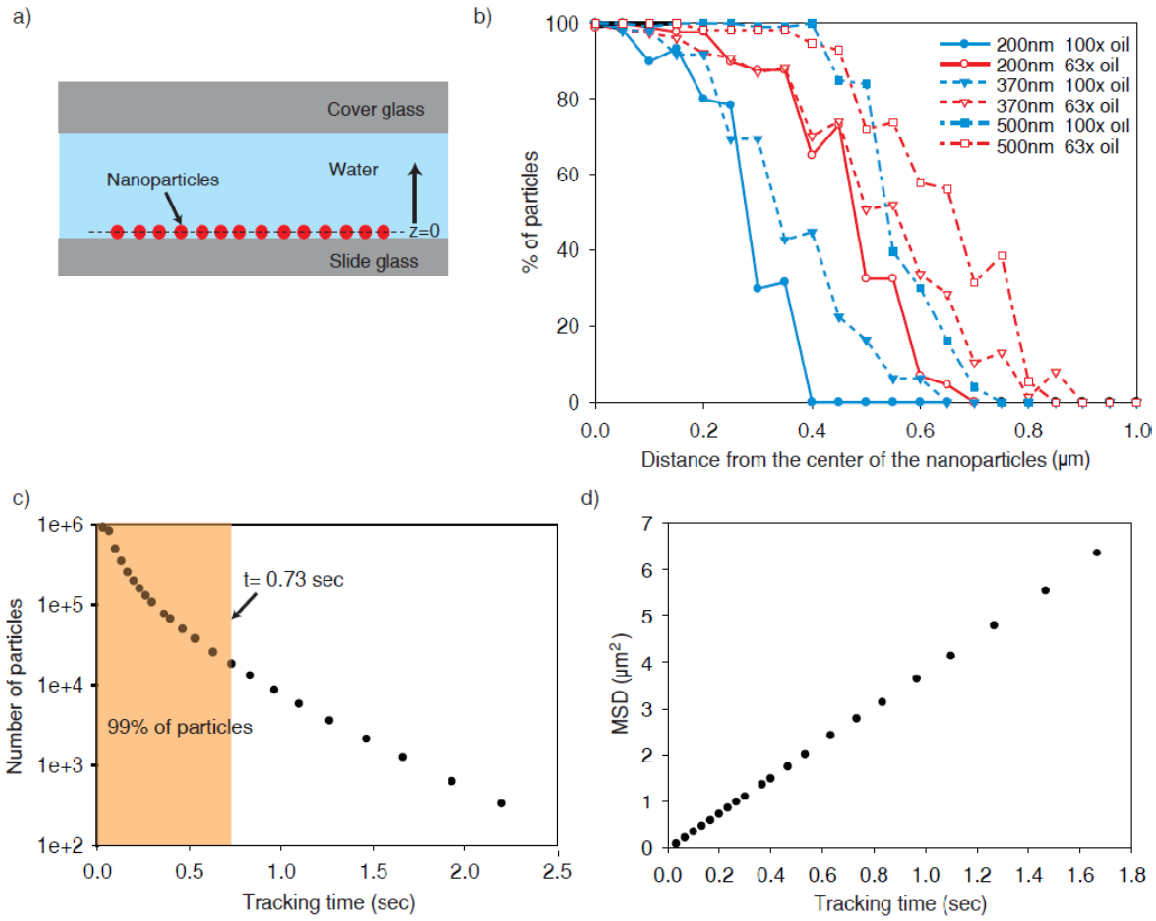

Figure 4.2. Mechanism of 3-D temperature mapping using Brownian motion of nanoparticles. a) Schematic of a sample slide for determining spatial resolution in the axial dimension. b) Percentage of particles indentified by the software algorithm as a function of distance from the center of particles. Z-stacks with a 50 nm step size were acquired and processed. c) The distribution of tracking time of the particles in the case when 500 nm diameter particles were imaged with 63X air objective. d) Corresponding MSD of the 500 nm particles as a function of the tracking time at 25ºC.

In this method, the vertical resolution of each temperature measurement depends upon the tracking depth, which is defined as the distance above and below the measurement focal plane, outside of which particles cannot be tracked by the software algorithm. The tracking depth depends on particle size and microscope optics. To experimentally determine the tracking depth, a sample specimen with a single layer of particles was prepared (Fig. 4.2a), and a series of images at different focal planes with a 50-nm step size were acquired from the center ($z = 0$ in Fig. 4.2a) of particles in the

vertical direction. Fig. 4.2b shows the percentage of particles the algorithm can identify as a function of vertical distance above the particle layer. For example, with 200-nm particles and a 100X oil objective, the tracking depth is found to be 0.4 μm above and below the focal plane, which corresponds to a minimum vertical measurement resolution of 0.8 μm.

The small tracking depth not only enables temperature measurement in the vertical direction, but also allows two-dimensional (*x* and *y*) temperature mapping in a focal plane. This is possible because the three-dimensional random motions of nanoparticles cause them to move in and out of the tracking range, thereby limiting the length of time during which each particle can be tracked. The MSD value associated with the trajectory of the particle can be assigned to the location of the center of mass of the trajectory. In this scenario, the MSD value associated with the trajectory corresponds to the *x* and *y* resolution of the measurement. As an example, using 500-nm particles with a 63X air objective (Fig. 4.2c), the tracking time of 99 % of particles was less than 0.7 sec at room temperature. The corresponding MSD of the particles was less than 3 μm^2 (Fig. 4.2d). Therefore, the temperature calculated from each MSD represents a local value defined by the distance explored by the particle, 1.7 μm. These results show that the spatial resolution of our simple videomicroscopy method is as low as 1~2 μm in all dimensions. Therefore, 3-D temperature mapping can be achieved without using multi-photon optical scanning.

4.5.3 2-D temperature mapping

In some microfluidic applications, spatial temperature gradients in a micro-scale channel are desired to study temperature-sensitive biological phenomena, such as the rate of cell division[38]. To demonstrate the capability of our method to measure spatial variations of temperature in such systems, we performed temperature measurement in a microfluidic device that was specifically designed to generate a temperature gradient. Two parallel temperature control channels (Fig. 4.3a, b) sandwich a middle channel that is filled with particle suspension. We first measured the temperature distribution at room temperature with no imposed temperature gradient. Fig. 4.3c shows a false-color image of measured temperature distribution. The standard deviation of temperature is 0.62°C, which is small and gives an indication of the temperature resolution one can get with our technique.

We then created a temperature gradient across the particle filled channel by flowing a cold stream of ~ 5 °C and a hot stream of ~ 35 °C through the parallel side channels (Fig. 4.3a, b). Fig. 4.3d illustrates the measured temperature distribution in the presence of a temperature gradient, with Fig. 4.3e showing the results of the corresponding numerical simulation. As expected, both the experimental data and the numerical simulation demonstrate that temperature increases as a linear function of distance from the cooling side to the heating side with a rise in fluid temperature of ~ 6 °C. This temperature gradient is quantified in Fig. 4.3f, for which the horizontal (*x*-direction) temperature profile at height of 40 μm (center of the channel in the *z*-direction) was read. The observed temperature gradient corresponds well with the numerical simulation, typically within 1 °C. Discrepancies between the predicted temperature and the measured temperature are in part due to slight geometric inconsistencies between the actual microfabricated channels and the one used in the numerical simulation. In addition, during operation of the device, we observed that flowing pressurized streams slightly deformed the thin PDMS wall in between heating and cooling channels and

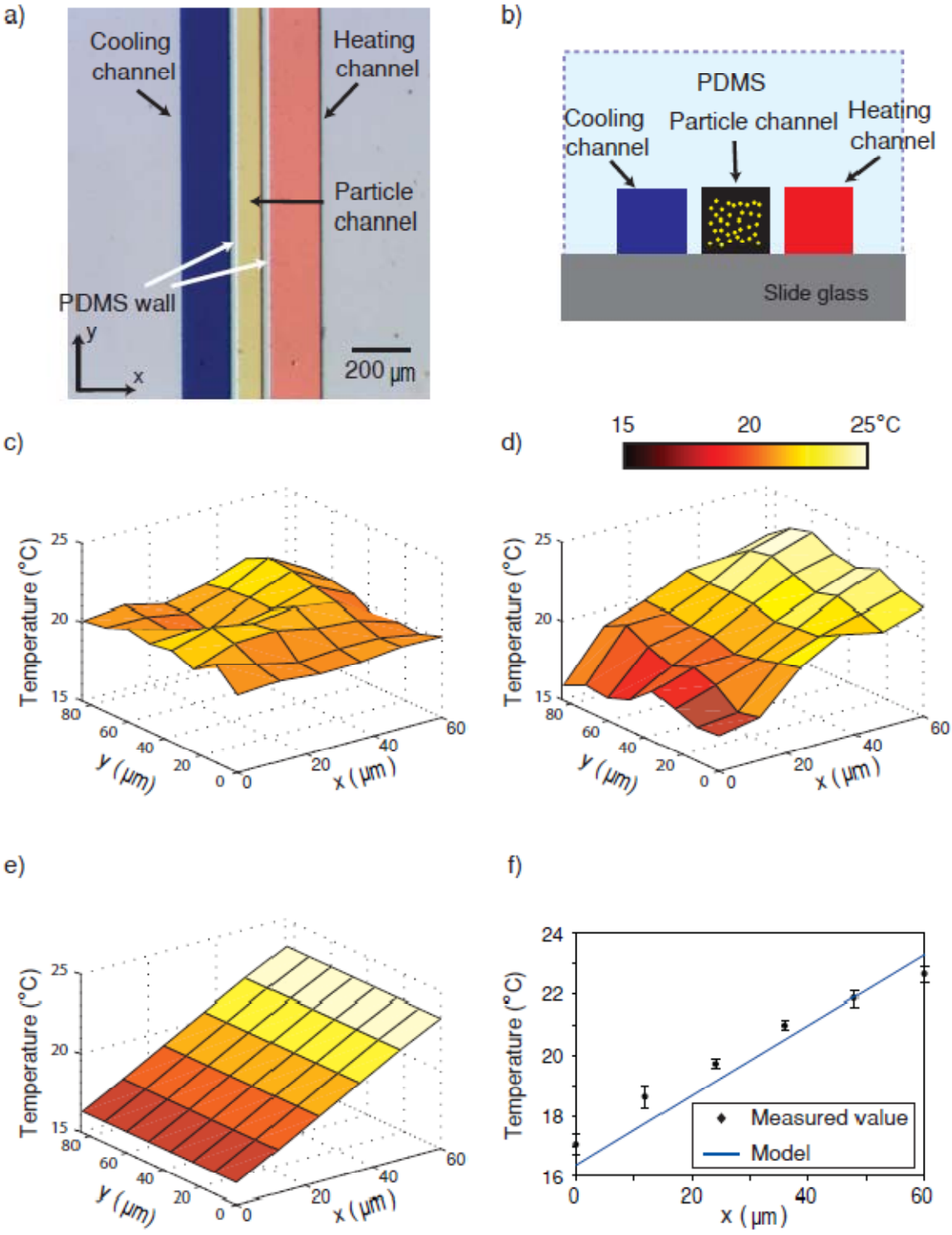

Figure 4.3. 2-D temperature mapping. a) Optical micrograph of the microdevice fabricated using soft lithography. The temperature control channels colored with red (hot stream) and blue (cold stream) was 200 µm × 80 µm (width × height) and the tracer

particle loading channel colored with yellow was 60 μm × 80 μm (width × height). The temperature distribution in the detection zone was generated by flowing two streams with controlled temperatures through the temperature control channels. b) Schematic of cross-sectional view. (c-d) False-color image of measured temperature distribution: c) with no imposed temperature gradient at room temperature. d) in the presence of temperature gradient. Hot stream: 35 °C, cold stream: 5 °C. e) Corresponding numerical simulation. f) Horizontal temperature line profile at height of 40 μm across the particle loading channel. Black circles: measured values, the blue line: numerical prediction.

particle loading channel, which was not taken into account in the numerical simulation. Additionally, uncertainties in the thermal properties of PDMS and the surrounding boundary temperatures may contribute to the discrepancies[115, 118].

In these experiments, we demonstrated that tracking individual particles enables spatially resolved temperature measurement in the horizontal direction with a resolution of ~ 12 μm. We note that, although the theoretical optical resolution for our 63X objective is less than 2 μm, to reduce experimental uncertainty we needed to discretize the field of view as shown Fig. 4.3c-e so that each domain contains more trajectories of particles to increase number of data points. This resolution can be easily improved by using higher magnification objectives, higher speed cameras, particle suspensions of higher concentration, and/or three-dimensional particle tracking[116].

4.5.4 3-D temperature mapping

Many microfluidic systems are multifunctional and highly integrated. This functional requirement results in increased complexity of microchannel networks and often requires three-dimensional layering of the components[79, 113]. For example, microfabricated electrodes for DEP are normally fabricated on a dielectric substrate (such as glass), and Joule heating caused by the operation of electrodes could generate temperature gradients along the horizontal and the vertical direction inside the channel[113].

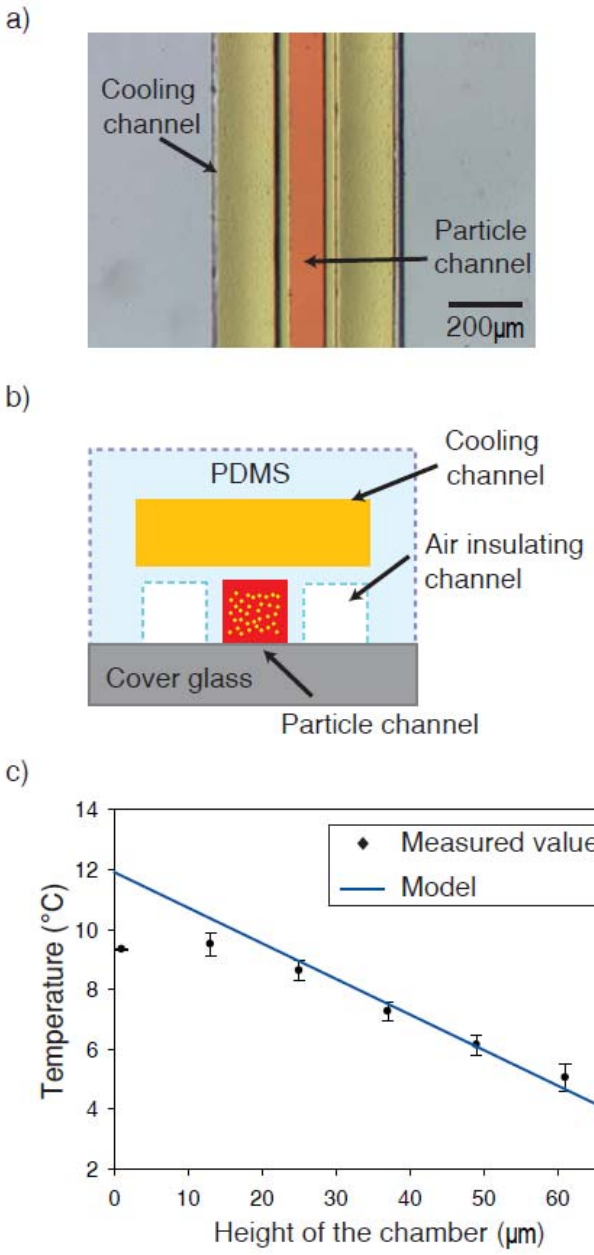

Figure 4.4. 3-D temperature mapping. a) Optical micrograph of the microdevice fabricated using multilayer soft lithography; yellow, temperature control channel; red, particle loading channel. b) Schematic of cross-sectional view. c) Comparison between experimentally measured and numerically predicted temperature profile as a function of height in the particle loading channel showing good agreement. Black circles: measured values, the blue line: numerical prediction.

To demonstrate the potential application of our thermometry method in the vertical direction (z-axis), we measured the temperature distribution in a multi-layered

microfluidic device that generates temperature gradient perpendicular to the glass substrate. Fig. 4.4a and 4.4b illustrate the geometry of the multi-layer PDMS device. The temperature gradient was created by flowing coolant at -8 °C through the temperature control channel in the top layer. Air-filled channels were placed parallel to the particle loaded channel for insulation to minimize temperature gradients in the horizontal direction. The surface temperature of the cover glass was controlled by warm air from a heating fan and measured to be 30 °C. We obtained a z-stack of movies of nanoparticles with a step size of 12 μm and processed these movies with the image analysis algorithm to achieve optical sectioning.

Fig. 4.4c shows the experimentally measured and numerically predicted temperature profiles in the channel as a function of *z*, the height above the glass surface. The observed temperature variation was consistent with the numerical modeling. Although the PDMS membrane between the coolant channel and the particle channel is relatively thin (~ 40 μm) compared to the height of the channel and the thickness of the coverglass, a large temperature increase of ~ 12 °C occurred in the membrane as expected due to the inherently low thermal conductivity of PDMS (0.17 W/m K). Because polymeric materials including PDMS have been broadly used for devices that control temperature in microchannels[79, 119], in device design, the low thermal conductivity of the polymeric materials must be taken into account.

4.5.5 *In situ* temperature measurements in the presence of living cells

In situ temperature measurements via nanoparticle tracking were performed in the presence of living cells to test the robustness and compatibility of the measurement method in biological experiments The NIH/3T3 fibroblasts were seeded onto the glass surface inside a microchannel in a PDMS device that was pre-incubated with 2 μg/mL fibronectin. A 0.02 % w/v suspension of nanoparticles in D-MEM was introduced into the device, and the MSD of the particles was measured in two different microscopy modes (fluorescence and DIC) at two temperatures. MSD measurements (representative images shown in Fig. 4.5) and measured viscosity data of D-MEM (data not shown) were then used to calculate the corresponding temperatures on chip.

Temperatures calculated from *in situ* MSD measurements agreed well with those reported by the thermocouple, demonstrating the ability of the *in situ* method to function in the presence of adherent cells. Under heated conditions (from the heating fan), *in situ* measurements yielded a temperature of 37.9 ± 0.8 °C and 36.7 ± 1.9 °C in fluorescent and DIC modes, respectively (Fig. 4.5). The thermocouple, placed on the surface of the glass substrate outside the PDMS device, measured 39.0 ºC. At a lower temperature, the *in situ* measurements yielded temperatures of 29.1 ± 0.8 °C and 29.7 ± 1.0 °C, in fluorescence and DIC modes, respectively. In that case, the thermocouple read a temperature of 28.5 ºC. The differences between the *in situ* and thermocouple measurements can be attributed to the location of the thermocouple relative to the microchannel and the direction of convective heating from the fan. Since the heating fan was blowing down from above the device, the thermocouple was directly exposed to the air current, while the microchannel was shielded by the 5 mm-thick PDMS layer and faced the cooler underside of the device. Therefore, a slightly higher temperature at the thermocouple is expected under heated conditions.

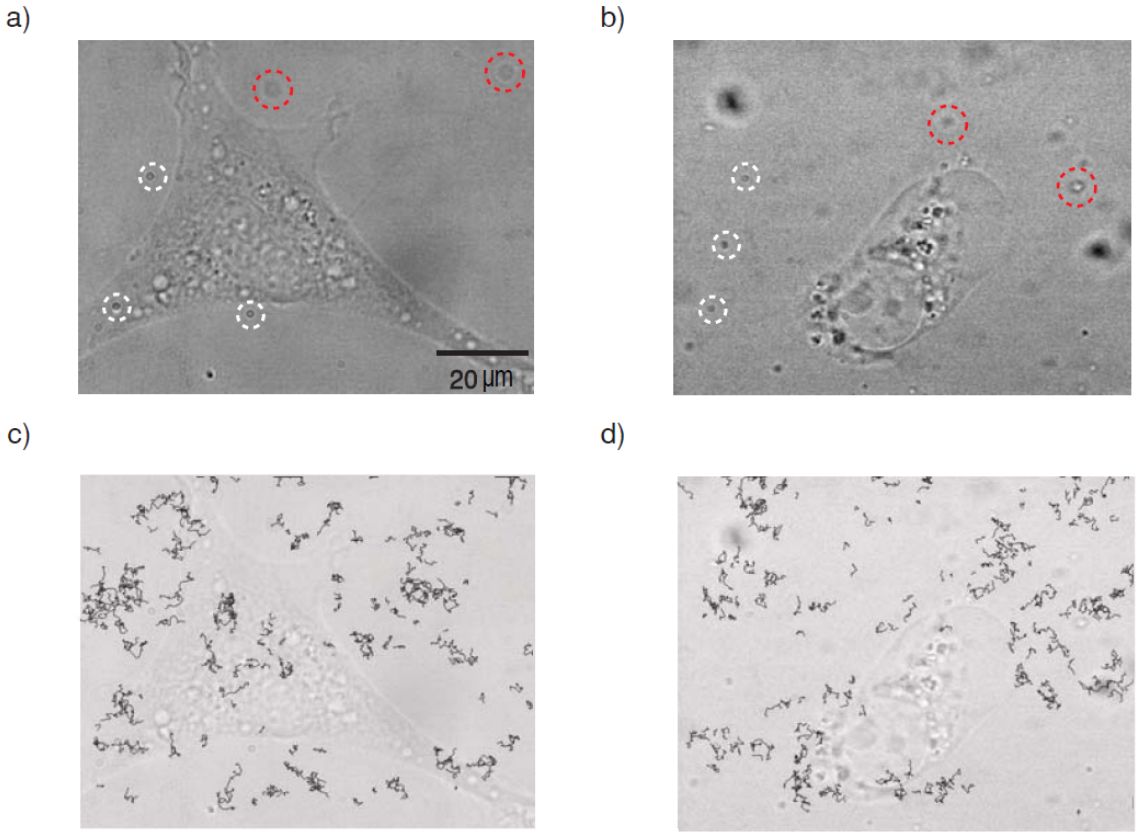

Figure 4.5. *In situ* temperature measurement in the presence of a biological samples. (a-b) Images in DIC mode, showing a NIH/3T3 cell and tracer particles in the chip. Focal plane of measurement is located 15 µm above glass surface; white circles indicate representative particles in focal plane; while red circles indicate representative particles out of focal plane. Temperature of the chip was controlled by convection (heating fan), and near-cell temperature was measured using the presented method in both fluorescent mode and DIC mode. a) At ~ 37 °C (Fluorescent mode: 37.93 ± 0.77 °C, DIC mode: 36.70 ± 1.86 °C). b) At ~ 29 °C (Fluorescent mode: 29.12 ± 0.84 °C, DIC mode: 29.68 ± 0.99 °C). Note that the fully spread morphology at ~ 37 °C (pointed, triangular) changes to a contracted morphology at ~ 29 °C, which is expected of this adherent cell line. (c-d) Overlay of the cell images (a, b) and the processed images showing trajectories of particles at ~29 °C in (c) fluorescent mode and (d) DIC mode.

The introduction of nanoparticles into the medium surrounding cells did not cause an observable change in cell morphology for at least 3 hours. This observation suggests that the nanoparticles do not affect cell viability, at least in the short term. Since *in situ* temperature measurements can be performed in as little as 10 seconds, it is very easy and practical to introduce the particles, perform experiments, and replace the medium to

remove the particles before the particles interact with cells. An advantage of the *in situ* measurement technique shown here is that it works not only in fluorescence but also in a transmitted light mode (DIC, in this case). Cellular features and outlines can be seen in the background of each image when operating with transmitted light, but such background images did not interfere with MSD measurements (Fig. 4.5). This feature makes it possible to monitor cells while tracking the temperature *in situ*. which opens new possibilities to study temperature-dependent cell responses, such as morphological changes in cell injury induced by temperature shifts[120, 121], immunological response of cells after local hyperthermia[122], and cell signaling under cold stresses[123]. In addition, the transmitted light mode does not suffer from potential photobleaching, which makes the technique more widely applicable.

4.6 Conclusions

We demonstrated for the first time that tracking Brownian motion of nanoparticles can be used for 3-D *in situ* thermometry in microfluidic devices. In contrast to fluorescence intensity measurement techniques, particle tracking is independent of fluorescent intensity. In particular, the use this methodology in combination with DIC mode microscopy completely eliminates photobleaching-related problems. Thus, this method offers accurate temperature measurements with superior reproducibility and reduced systematic error. Another notable advantage of this method is that it provides 3-D temperature mapping without using an expensive multiple-photon scanning setup. The use of software algorithm and the associated small tracking depth offer a spatial resolution up to 1 ~ 2 μm in the vertical direction. The most unique advantage of this method over conventional methods is that this method can be used for *in situ* temperature monitoring. We also note that one potential drawback of our method is that fluid must be stopped in order to track accurately Brownian motion of particles.

However, recent developments in particle tracking technology have shown that Brownian motion of particles is measurable in the presence of convection flow. Implementation of these more advanced particle tracking algorithms will not only enable temperature measurement in convection flow, but also broadens its application to the simultaneous measurement of fluid temperature and velocity distributions.

CHAPTER 5

MULTIPLEX PRESSURE MEASUREMENT IN MICROSYSTEMS

5.1 Overview

The microfluidic components of the microsystems for imaging and ablation of *C. elegans* utilize dynamic pressure change in the microchannels. It is, thus, important to characterize pressure distribution in the microchannels to aid further device optimization. This chapter describes a simple image-based method to measure pressure in microsystems using volume displacement of fluorescent particle suspensions. These micro pressure-sensors are composed of two flow layers with a polydimethylsiloxane membrane in between: the bottom layer includes a flow channel and the top layer contains a detection channel filled with suspensions of fluorescent particles. The pressure increase in the flow channel deflects the membrane, and this membrane deformation can be quantified by measuring the cross-sectional areas at specific focal planes. These simple sensors have the advantage that a broad sensing-range can be achieved by tuning the mechanical property and the geometry of the membrane during design and fabrication, and even simpler by tuning the focal plane or the pressure of a reference chamber while in operation. We also demonstrate here a pressure transduction scheme coupled with the image-based sensing method as a multiplex pressure measurement tool for simultaneously detecting pressures in multiple locations in a microsystem. Overall, the image-based pressure sensing method has high precision when operated in both the direct and the remote detection modes. Compared to conventional mechanical methods of pressure detection, this technique is inexpensive because it does not require complex off-chip equipment to quantify the pressure-dependent membrane deformation. In addition, the image analysis using the software code developed here is fast, and it generates data that are simple to interpret. This chapter covers background,

design of the pressure sensors, image analysis algorithm, and mechanism of the remote/multiple pressure measurements. This work is done in collaboration with Hyewon Lee in Dr. Hang Lu's group. Numerical models that she developed to aid design of the sensors are not included in the discussion here.

5.2 Introduction and background

5.2.1 Motivation

The robustness and automation of the microsystems for imaging and laser ablation I developed (Chapter Two and Chapter Three) greatly relies on how worms are manipulated in the microchips. To handle a large number of worms robustly and consistently, we developed the microfluidic components, such as the loading regulator and positioning channels. These components passively use dynamic pressure change in the devices that is naturally caused by presence and position of worms in the loading channels when a constant pressure drives worm suspension. Although, the numerical models suggest that the components can operate properly in a broad pressure range, it is important to experimentally measure the actual pressure distribution to further optimize the devices.

In many other applications, accurate pressure control and measurement is also required in handling biological or chemical samples in microsystems, oftentimes at low flow rates with minimum fluctuation[79, 124-129]. For example, pressure-driven flow was used in cell loading into target microchannels for single cell studies[124-126] and supplying perfusion media for long-term cell culture[128, 129]. Besides controlling the flow, pressure measurement has been used to characterize hydrodynamic resistance of microchannels for studying mechanic properties of cells. For instance, the rheological properties of red blood cells and white blood cells in the flow of microchannels were studied by measuring

pressure drop variations at the outlet of the test channel[130, 131]. In these examples, the response of the flow system depends on cell type, the number of cells, and drug-induced changes in mechanical properties of the cell membrane; the pressure fluctuation in the system can be used to infer these changes. In other applications, pressure is critical in the generation and manipulation of monodisperse droplets and bubbles in a continuous liquid stream, in various reactions such as polymerase chain reaction[132], hydrophobic-hydrophilic patterning in microchannels[133], and manufacturing contrast agents for ultrasonic imaging[134]. Gas-liquid segmented flow is often used in the microfluidic systems to enhance mixing and transverse channel transport by inducing a recirculation motion in the liquid. In multiphase flow in microchannels, the size of the gas bubble is highly dependent on the applied pressure in gas stream[135, 136]. Thus, pressure sensing in microfluidics is important and necessary in many applications.

5.2.2 Limitations of existing technology

Although there is a great need of pressure measurement in microsystems, from a practical point of view, accurate pressure measurement inside microfluidic devices is difficult without impeding system operation, due to the small feature sizes in microchannels. To achieve on-chip pressure detection, a number of measurement methods have been developed[130, 137-143]. A microfluidic differential manometer was used to detect pressure drop by measuring displacement of the interface of two streams[130], one of which is the sample flow and the other the reference fluid. The movement of the interface as a function of pressure change in a sample flow was measured by image analysis. This differential manometer can measure the rapid fluctuations of pressure, and it is suitable for the identification of target objects in flow to enable studies of physical state of individual cells; however, it requires the sample fluid to be in contact with the reference fluid, and does not measure absolute pressure. In another approach, an *in-situ*

pressure sensor used trapped air compression to detect static pressures for both liquid and gas samples precisely[137]. While accurate, this design requires long indicator channels for a large sensing range and large chambers for high resolution of small pressure changes. These size constraints in the device layer may not fit to highly integrated microchips. In addition, the application of this method is limited because trapping air in the indicator channels requires the use of non-gas-permeating materials, such as glass, which is more difficult to fabricate compared to standard soft lithography. Yet another common pressure measurement method uses a membrane deflection to detect applied pressure. Piezoresistive[138, 139], capacitive[140], or optical[141] sensors are typically used to detect the change of membrane deflection. It has been known that these mechanical methods show high sensitivity and precision. However, there are a few drawbacks to this approach as well: first, these measurements may have substantial dead volumes; second, they require complex electrical/electronics control[138-140] or expensive optical equipment such as lasers[141] and position- or intensity-sensitive detectors to detect membrane displacement; third, these devices may not be readily integrated with any existing microfluidic devices because of the multistep fabrication processes, most commonly based on silicon or other semi-conductor fabrication processes[138-141]. Alternative PDMS pressure sensors fabricated by soft lithography were also developed[142, 143]. However, these sensors requires either optical equipment with a complicated analysis[142] or multiple valves and additional electronics for control[143]. Additionally, to multiplex these existing pressure sensors (e.g. to measure pressure at multiple locations) would also require additional hardware and take longer time.

5.3 Objectives of the work performed in this chapter

To address the need for an integrated on-chip pressure sensor, we developed a simple image-based pressure measurement method that fulfills the following goals: (1) easy to use; (2) inexpensive; (3) high accuracy (accuracy of < 0.2 psi in the range of 0 ~ 2psi and < 0.5 psi in the range of 2 ~ 15 psi); (4) broad detection range (0 ~ 15 psi); (5) fast detection (less than a second); (6) multiplex pressure measurement.

5.4 Experimental methods

5.4.1 Design and fabrication of devices

The pressure sensors we designed consist of flow channel layer, detection layer, and PDMS membrane in between layers. The pressure increase in the bottom microchannels results in the deflection of the membrane toward the upper channel ("detection channel") filled with nanoparticle suspension. This pressure-dependent membrane deformation is quantified by measuring the diameter of area that is in- and out-of-focus particles.

Multilayer soft lithography was used to fabricate all two-layer devices in PDMS (Dow Corning Sylgard 184, Essex-Brownwell Inc., McDonough GA)[55]. To make all masters, features on transparency masks (Appendix G) were transferred to SU-8 2025-spin-coated wafer (or SU-8 2010 and AZ 50 XT in series) by standard UV photolithography. For direct pressure measurement method, both of the two masters were fabricated using SU-8 2025 (Microchem Corp., Newton, MA): the top layer (Appendix Gb-d) is a mold for a detection channel and the bottom one includes a flow channel (Appendix Ga). For remote and multiplex detection scheme, the top layer contains sensor chambers, detection chambers, transferring channels, and valves, and the bottom layer includes flow, reference, and valve control channels. To fabricate masters

for the top layers, SU-8 2010 was used for control channel, SU-8 2025 for two chambers, and AZ 50XT (AZ Electronic Materials USA Corp, Somerville, NJ) to make the channel closable by the control valves. The wafer surface was treated with tridecafluoro-1,1,2,2-tetrahydrooctyl-1-trichlorosilane vapour (United Chemical Technologies, Inc, Bristol PA) to facilitate release of PDMS from the molds. To form a 10-20 μm-thick PDMS membrane on top of the flow channel, a PDMS mixture of A and B in 20:1 weight ratio was spin-coated on the mold of the bottom layer and partially cured at 65 ^{o}C for 15 min. For the top layers, 5 A: 1 B weight ratio PDMS mixture was poured onto the top-layer master to give a 5-mm thickness and cured at 70 ^{o}C for 20 min. After peeling off the 5-mm PDMS top layers, the top layer was aligned onto the thin bottom layers and cured at 70 ^{o}C for 2 hr. The devices were then cut to shape and access holes were punched in the PDMS before the devices were bonded to cover glass. In order to measure the thickness of the membrane, the devices were cut vertically, and the membrane thickness was measured using an optical microscope with a 20X objective.

5.4.2 System preparation and operation

For all the experiments, carboxylate-modified polystyrene particles (500-nm) (FluoSpheres®, Invitrogen, Carlsbad, CA) were suspended in DI water and sonicated for ~30 min to break aggregates. The particle suspension was introduced into the detection channel and the fluid channel was filled with DI water (Fig. 1a, b). For the direct pressure measurement, the inlet of the flow channel was connected to a nitrogen tank and exposed to pressures in the range of 0-12 psi. The deformation of the membrane was then quantified as described in the following section. For the remote pressure measurements, the sensing chamber, the detection chamber, and the transferring channel in the top layer were filled with the particle suspension. An elastomeric pneumatic on-chip valve was then closed to keep the total volume of the nanoparticle suspension

constant. The flow channel and reference channel in the bottom layer were filled with DI water. Pressure ranging from 0-11 psi was then applied in the flow channel and deformation of the membrane of the detection chamber was quantified. For the multiplex pressure measurement, the device was prepared as described previously. In order to calibrate the four sensors, the outlet of the flow channel was closed and pressure ranging from 0-11 psi was applied in the flow channel. Images were acquired under multiple pressures and processed. After calibration, the outlet of the flow channel was opened and the fluid was connected to a pressure source. Pressure drop along the flow channel was then analyzed by measuring pressure at four points of the flow channel simultaneously.

5.4.3 Image analysis

The fluorescent nanoparticles at a focal plane were monitored via optical microscope (Leica DM-IRB) with a 100X or 63X oil-immersion objective, and images were captured using a Hamamatsu C9100-13 EM CCD camera. The captured images were analyzed with software code developed in Matlab® (Appendix H) (Fig. 5.1). The analysis involves three steps: locating possible particle centers, indentifying in-focus particles, and defining a minimum circular boundary that encompasses all the in-focus particles. During the first step, the original image (Fig. 5.1a) is filtered via a spatial bandpass filter to remove random high/low frequency noises (Fig. 5.1b). The brightness-weighted centroid algorithm then determines all local maxima regardless of whether they represent a real particle. After indentifying all local maxima, cutoff criteria based on combinations of brightness and geometry were applied (Fig. 5.1c). Lastly, distances between center of the detection chamber and each in-focus particle are calculated and the longest distance was chosen as a diameter of a minimum circular boundary that encloses all the in-focus particles (Fig. 5.1d). For the multiplex pressure measurement, images were discretized into four equal-sized square domains. Each domain shows a quarter of

one of the four sensors. For each domain, distances between the corner of the domain (the center of the detection chamber) and in-focus particles were calculated and a diameter was determined as described previously.

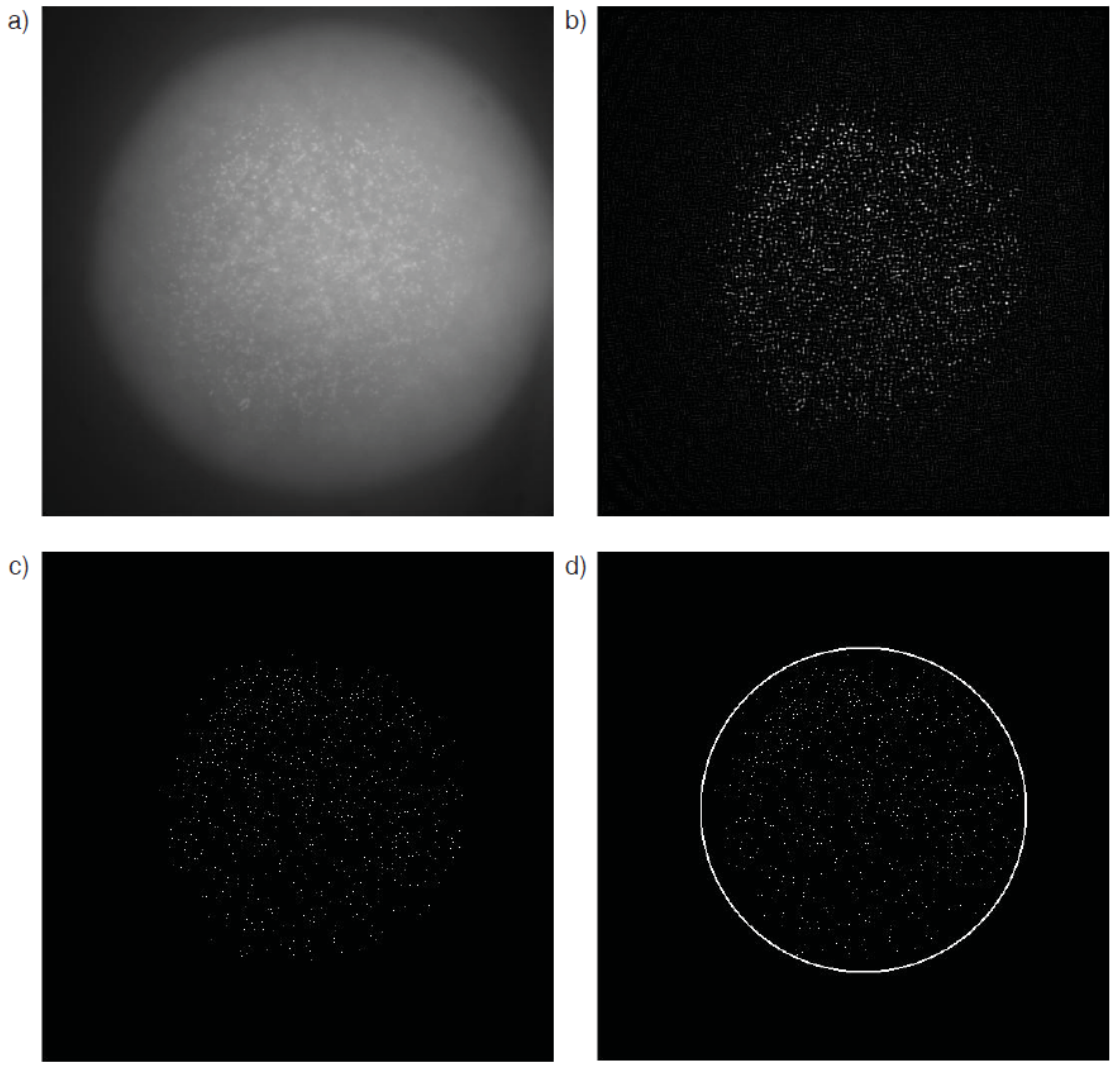

Figure 5.1. Image analysis process. a) A raw image. b) A processed image filtered via a spatial bandpass filter. c) A processed image showing identified in-focus particles after cutoff criteria applied. d) A minimum circular boundary that encloses all the in-focus particles is calculated and drawn on Fig. 5.1c.

5.5 Results and discussions

5.5.1 The mechanism of the image-based pressure detection method

In order to detect pressure by a simple image-based method, we developed a microfluidic pressure sensor consist of two flow layers and a PDMS membrane in between. This device has a top layer that includes a detection channel filled with a fluorescent particle suspension and a bottom layer containing a flow channel (Fig 5.2a, b). The pressure sensing mechanism is based on the deflection of the membrane. We use a simple fluorescence microscope to capture images located within the detection chamber at particular focal planes, a few microns above the membrane (Fig 5.2a, b), to quantify the applied pressure. Before applying pressure in the flow channel (bottom), the membrane is flat (Fig. 5.2a), and therefore at the focal plane, the image shows that the area enclosing all in-focus nanoparticles is the same size as that of detection chamber itself (Fig. 5.2c, e). When pressure is applied to the fluid in the flow channel, the membrane deflects upwards (Fig. 5.2b) and displaces the particle suspension fluid and thus the in-focus particles in the center of the image (Fig. 5.2d, f); the image then shows only a donut-shaped area containing fluorescent particles that are in focus. Note that the raw images (Fig. 5.2e, f) also show fluorescence from particles that are out of focus with dimmer and more diffused signals. It is through image processing that we can quantify the membrane deformation as a function of applied pressure. The Matlab® algorithm automatically processes the raw images, identifies in-focus particles (Fig. 5.2g, h), and calculates the diameter of the area devoid of the in-focus particles, as described in the previous section. This entire process takes less than one second, allowing for almost instantaneous pressure detection. Moreover, the simplicity of the sensing mechanism and the sensor design allow the sensor to be easily integrated in microdevices, particularly in multilayer PDMS devices, without complicated fabrication processes.

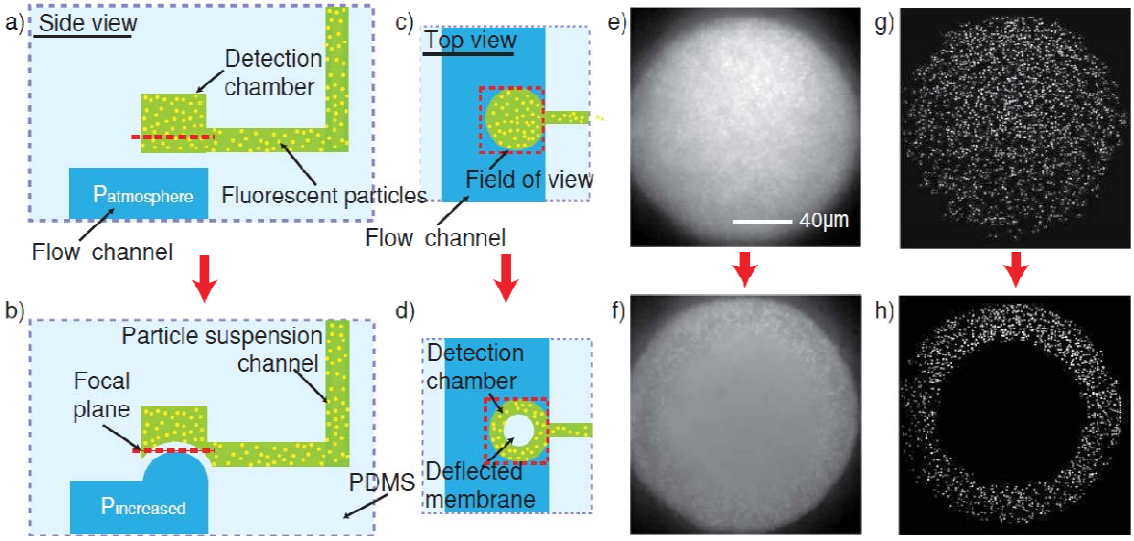

Figure 5.2. Design and operating mechanism of an image-based pressure measurement method. Figures (a, c, e, g) show the sensor before pressure is applied in the fluid channel below, and figures (b, d, f, h) after. (a-b) Schematic of the cross-sectional views before (a) and after (b) applying pressure in the fluidic channel showing membrane deformation as a function of applied pressure. (c-d) Schematic of the top views at a particular focal plane before (c) and after (d) applying pressure in the fluid channel, the latter showing pressure-dependent membrane deformation, i.e. a decrease of an area enclosing in-focus particles. (e-h) Raw and processed images of 500-nm fluorescent polystyrene particles correlating with applied pressure. Figures (e-f) represent raw images showing in- and out-of-focus particles before (e) and after (f) the pressure is applied. Figures (g-h) represent processed image showing only those particles that are in focus before (g) and after (h) the pressure is applied. The diameter of the area devoid of particles is a strong function of the applied pressure, and can be automatically measured rapidly and accurately by the software.

5.5.2 Using tunable focal plane to broaden sensing range of individual pressure sensors

The sensing range and sensitivity of the pressure detectors are strong functions of the membrane deformability. The deformability of the membrane can be tuned by two parameters: Young's modulus and the dimensions of the membrane. An additional attribute of our sensing method is that it is possible to perform pressure measurement at multiple focal planes using a single sensor for different pressure regimes: we can use large focal distances (or higher focal planes) for higher pressure ranges, and short focal

distances (or lower focal planes) for lower pressure ranges; Fig 5.3a, b illustrate such a scheme. To implement the scheme experimentally, we fabricated a device with a membrane 160 μm in diameter; images at two focal planes, 4-μm and 24-μm from the bottom surface of the membrane, were acquired and processed for pressures ranging from 0 to 10 psi. At the lower focal plane (4 μm), pressure in the lower operating range (0-1.6 psi) can be measured with a high degree of accuracy (Fig. 5.3c). Similarly, pressure measurement at the higher focal plane (24 μm) shows high sensitivity and the sensing range extends from 1.6 psi to 10 psi (Fig. 5.3d). For both sensing regimes, the measured values fit well empirically to exponential functions ($P = 0.8563 - 0.8377e^{-1.8042d}$ with R^2=0.9992 for the lower focal plane, and $P = 0.8327 - 1.5642e^{-0.4166d}$ with R^2=0.998 for the higher focal plane, with P being pressure (psi) and d being the normalized diameter of the deflected membrane). For this set of measurements, atmospheric pressure was used as a reference to measure absolute pressures in the microsystems. To further extend the sensing range, one can simply pressurize or depressurize the nanoparticle suspension channel. The results shown here demonstrate that broad ranges of pressure can be measured using a single sensor by tuning focal positions or a reference pressure without re-design or fabrication.

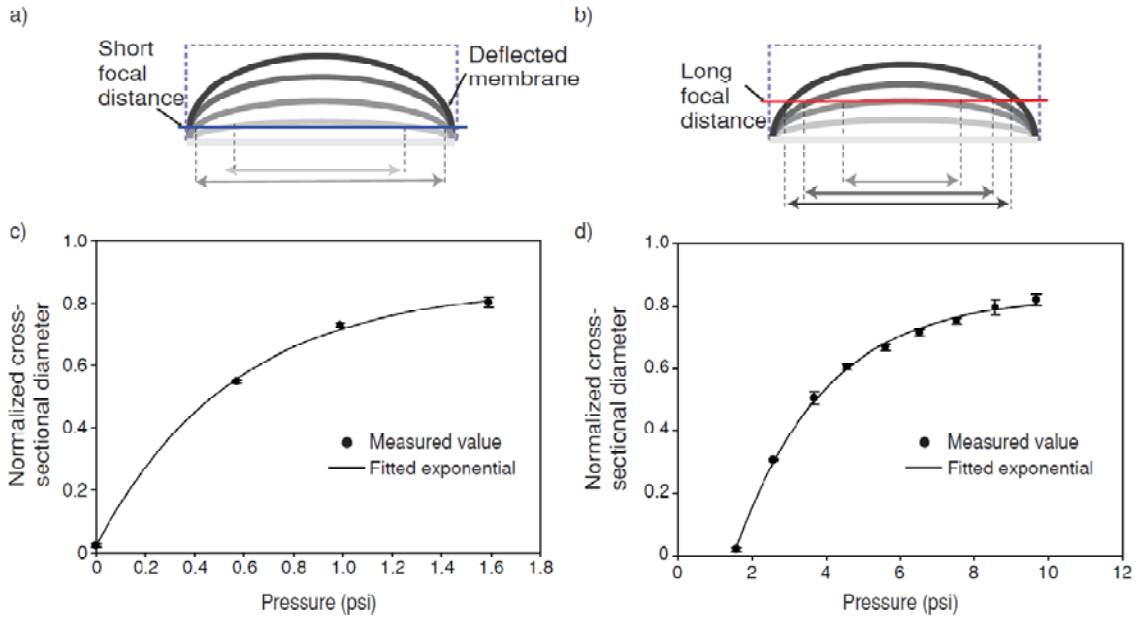

Figure 5.3. Tuning the focal position for different sensing ranges using a single sensor. (a-b) Schematic of the extent of the membrane deflections as a function of applied pressures at a short (a) and a long (b) focal distance. The lower focal point allows the accurate detection of lower pressures because it is sensitive enough to show differences in low pressures, but is likely to have large errors at higher pressures. In contrast, the higher focal point is better for higher pressures while it will not be able to detect very low pressures. c) The diameter of the area that is devoid of in-focus nanoparticles as a function of pressure 4 μm above the membrane surface. The error bars are standard deviations. The signal is a strong function of the applied pressure between 0 and 2 psi in microchannel, which can be fitted to $P = 0.8563 - 0.8377e^{-1.8042d}$. The sensor in this range has an excellent sensitivity. d) The diameter of the area devoid of focused-nanoparticles as a function of pressure at 24 μm above the membrane surface. The signal is highly dependent on the pressure in a range of 2 to 10 psi, which can be fitted to $P = 0.8327 - 1.5642e^{-0.4166d}$.

5.5.3 Remote pressure measurement

For applications that require pressure measurement outside of or far from flow channels, we developed a volume-displacement transduction method using a system with two connected chambers (Fig 5.4a, b). The two chambers - the sensing chamber on the flow channel and the detection chamber on the reference chamber - are connected to each other by a transduction channel, and all are filled with a nanoparticle suspension. An on-chip valve for the sensor layer is closed to keep the total volume of the nanoparticle

suspension constant (after the injection of the nanoparticle suspension). Both chambers have a thin membrane (diameter:thickness ~ 16:1). These membranes are made of PDMS mixture of A and B in 20:1 as before and therefore much more deformable, whereas the other parts of the chambers and the transferring channel are made of much stiffer PDMS of 4:1 mixing ratio. This difference in elastic modulus minimizes the deformation in the rest of the system other than the membrane. In our experiments, the focal plane where images were obtained is located in the reference chamber, 8 μm below the membrane of the detection chamber.

Before pressure in the flow channel is applied, both membranes are flat (Fig. 5.4a) and, therefore particles are not visible in the field of view (Fig. 5.4c, e). As pressure increases in the flow channel, the membrane of the detection chamber deflects upward and displaces a volume of particle suspension (Fig. 5.4b). This volume displacement is transferred to the detection chamber through the transferring channel and leads to the deflection of the detection membrane. The deformation of the detection membrane is then quantified as described previously (Fig 5.4f). In an ideal sensor, one would like to have no loss of the pressure in the transduction process, so the pressure measured at the detection region is the same as the one in the sample fluid channel. Deformation of the chamber walls and the transferring channel could be sources of concern; this capacitance may reduce the transferred volume and therefore reduce the deflection of the detection membrane, which leads to lowering of the sensitivity.

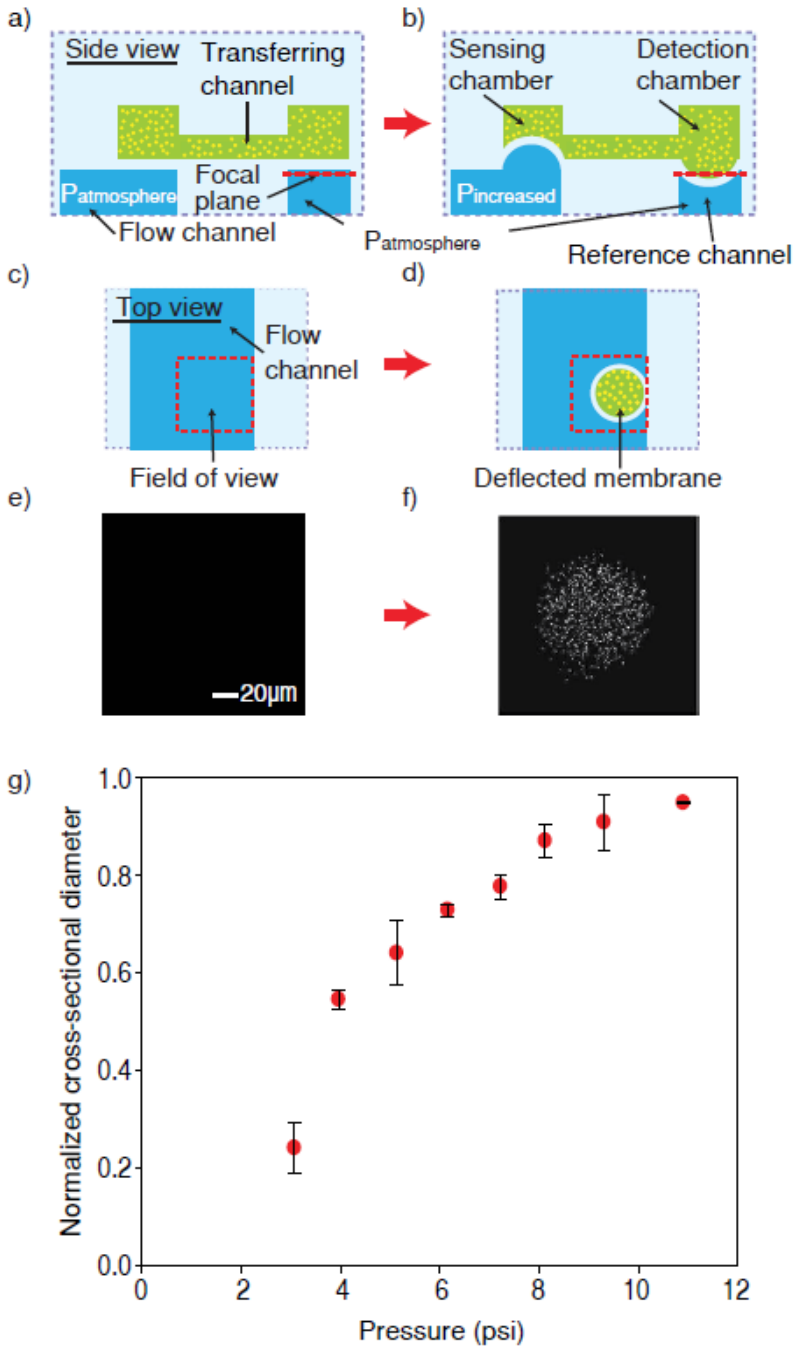

Figure 5.4. Method for remote pressure measurements. (a-b) Schematics of the cross-sectional views before (a) and after (b) applying pressure in the flow channel, showing the membrane deflection and transferring volumetric displacement of nanoparticle suspension. (c-d) Schematics of the top views showing the focal plane before (c) and after (d) the applied pressure. (e-f) Processed images of in-focus fluorescent particles before (e) and after (f) applying pressures. g) The normalized diameter of the area that is

in-focus nanoparticles as a function of pressure in a microchannel, showing that pressures in a range of 3-10 psi can be measured accurately using this method.

By using much more rigid material for the rest of the device other than the membrane as we have done in our experiments, however, we observed that the loss of signal in our setup is negligible. Using this method we measured pressures remotely, in contrast to the direct sensing methods in Fig. 1-3, ranging from 3 to 10 psi with good accuracy (Fig. 5.4g). We note that the sensing range of the remote pressure sensor narrows somewhat at the low pressure end as compared to that of the direct detection method. This is because deflecting two serially connected membranes requires slightly higher pressure. However, as described previously, the sensing range can be extended by using multiple focal planes or depressurizing or pressurizing the reference chamber should there be a need.

5.5.4 Multiple-pressure measurement

Using the remote pressure measurement method, pressures in various parts of the flow channel can be transduced and the signals transferred to a single location, allowing us to detect pressures in multiple locations simultaneously. To demonstrate the potential application for measuring pressure in various parts of a chip, we performed a multiplex pressure measurement using a microdevice shown in Fig. 5.5a. The flow channel consists of large chambers connected by serpentine-shaped long and narrow channels (Fig. 5.5a). Each sensing chamber is located on a large chamber in the fluid path, and all detection chambers are assembled in one location on a reference channel (Fig. 5.5a). The field of view shows a quarter of each detection chamber (Fig. 5.5b); because of the symmetry of the circular membrane it provides all the necessary information for calculating four pressure values.

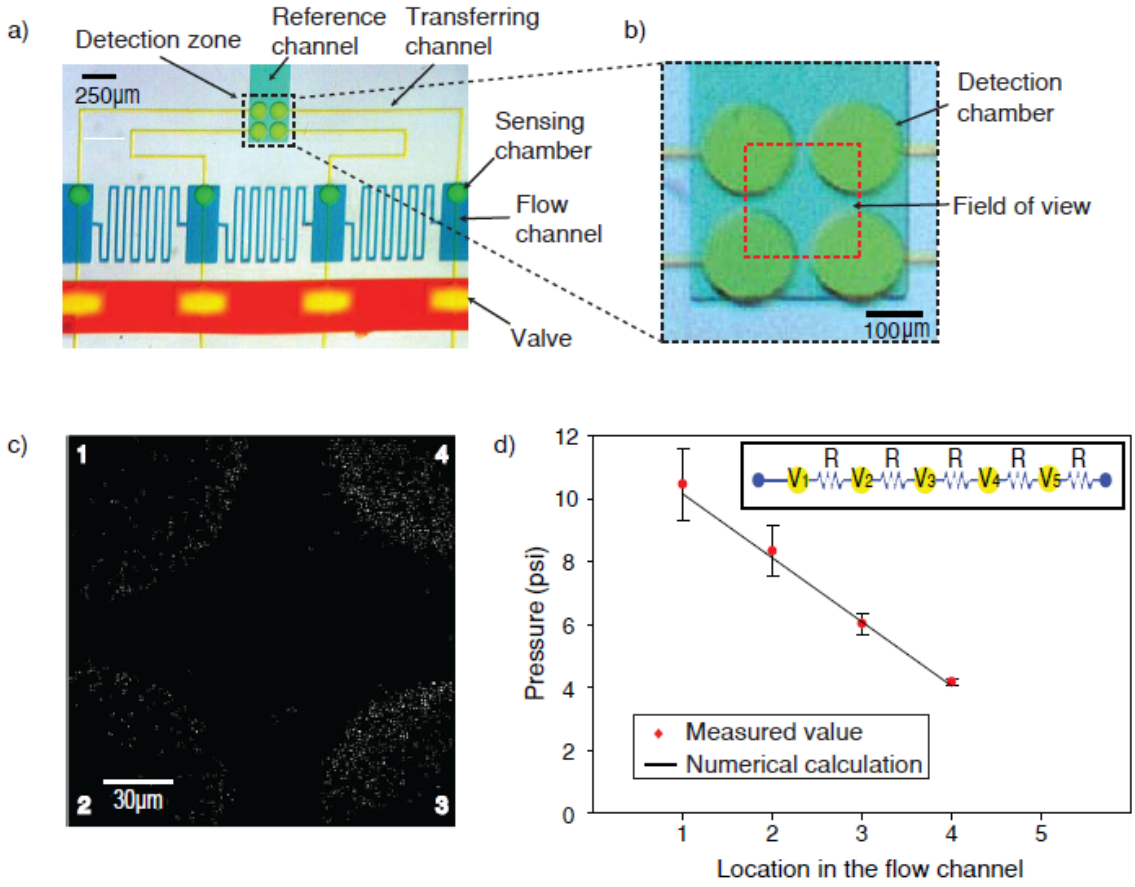

Figure 5.5. Method of multiplex pressure measurements. a) Optical micrograph of the microdevice fabricated using multilayer soft lithography: yellow, detection channel filled with nanoparticles in top layer; blue, flow channel; red, valve for closing detection channel; green, reference channel where four detection chambers are collected in a single location. The zoom-in view shows the detection chambers and field of view where the image is captured. The flow is from left to the right in the fluid channel when multiple pressures are measured. b) Zoomed-in view of the detection chambers. c) Processed image showing four areas of in-focus particles correlated to the pressure at various locations in the flow channel. Chamber 1 is most upstream and chamber 4 is most downstream. d) Pressure measured by the diameter of the area containing in-focus particles, as a function of positions in the flow channel. The inset figure shows a resistive circuit model corresponding to the microchannel network. Experimentally measured pressure is in good agreement with the numerical calculations based on the resistive circuit model.

We first calibrated the four sensors as a function of the applied pressure in the flow channel with its outlet closed so that the pressures we measured are static pressures. After the calibration, the outlet was opened and a flow was driven through the channel by

a constant back-pressure (P = 10.48 psi). A raw image showing a quarter of each of the four sensors was then obtained and processed to calculate the pressure values at the detection regions. As expected, the processed image shows that the area enclosing in-focus particles decreases as pressure of the flow decreases along the channel (Fig. 5.5c). To validate the measurement, we compared the experimental data with theoretically predicted values (Fig. 5.5d). The theoretical pressure values are numerically calculated by a resistive circuit model[144-146]. Calculated resistance of the serpentine-shape channel is over 2,000 times bigger than that of the 50 cm long tubing connecting the pressure source and the microfluidic chip, and over 800 times bigger than that of the large chambers in the flow channel. Hence the hydrodynamic resistances of the tubing and the large chambers are neglected, and we can simplify the circuit as shown in the inset of Fig. 5.5d. The theoretical calculations show excellent agreement with the measured values. In this multiplex measurement, image acquisition and processing were automated and took only a few seconds to readout the four pressure values. Thus, we believe this simple and fast detection scheme will improve the throughput of microfluidic devices especially for multi-functional or highly integrated devices.

5.6 Conclusions

We developed an on-chip pressure measurement method, which uses volume displacement of fluorescent particle suspension to detect membrane deflection. Unlike other mechanical methods, our system does not require expensive off-chip equipment or a complicated fabrication process, and is simple to use. The image analysis to measure the diameter of the area containing in-focus particles was sufficient as a readout of pressure. This image processing is easy to use and produces readily readable data that can be simply interpreted. Via simulation and experimental analysis, we observe that there are three simple ways to modulate the sensing range and sensitivity of the pressure

sensor: changing the membrane deformability by varying its Young's modulus and aspect ratio (diameter : thickness), tuning focal planes, and using different reference pressures. We show that it is possible to obtain highly accurate pressure measurements that are also predictable from simple models. These advantages of our pressure sensor allow it to be integrated with various microfluidic components for different applications. Moreover, the most unique advantage of this method over conventional methods lies in the ability to measure pressures at multiple locations simultaneously in a microsystem with a single readout, which enhances the throughput of microsystem operation. One application area of our method is simultaneously monitoring dynamics of biological or chemical processes depending on pressure changes in multiple channels, which can effectively decrease the detection time for analyzing a large number of samples.

CHAPTER 6

CONCLUSIONS AND RECOMMENDATIONS FOR WORK

6.1 Thesis contributions

The goal of this research was to develop integrated and automated microsystems for high-resolution imaging and high-throughput sorting/laser ablation of *C. elegans*. For these major experimental methods, the ability to process large number of samples with minimal human intervention can greatly facilitate study of many fundamental biological mechanisms. Novel technologies developed in this thesis to achieve this goal include microfluidic components for handling animals, processing algorithms for automating the microsystems, and numerical/experimental tools for characterizing the devices. Through these technological achievements we demonstrated automated and high-throughput imaging/sorting and laser ablation of *C. elegans*.

This thesis is the first to develop microfluidic machineries that make the entire animal handling process automatable in a robust and high-throughput manner. The novel microfluidic components, loading regulator, positioning channels, and cooling, systematically operate to manipulate a large number of animals. The loading regulator that is self-controlled by worms allows single worm loading without any additional off-chip control. The positioning channels enable consistent positioning of the animals in the field of view to minimize the processing time. These two crucial components are implemented by using partially closable valves and robustness of the components is proved through performing many biological applications. Additionally, this thesis introduces simple on-chip cooling methods and demonstrates that cooling can rapidly and reversibly immobilize worms for high-resolution imaging and laser ablation. We believe that the basic design rules and concept of the microfluidic components will establish the basis for future development of devices for handling live multi-cellular organism.

Secondly, to allow the microsystems to operate free from the need for any human intervention, Matthew Crane and I developed software systems that not only orchestrate operation of the microfluidic components but also automate image processing / phenotyping (developed by Matthew Crane), and laser ablation (developed by myself). The algorithms comprise control, acquisition and processing modules. Each module consists of several subroutines that can be easily modified for other experiments, such as long-term imaging, repetitive imaging, and drug screening. This modular nature of the software and its customizability will make it useful for a wide range of applications.

By automating sample handling and image analysis, the microsystems greatly improve the throughput and data quality. The microsystem for imaging/phenotyping has the ability to perform sorting based on cellular and subcellular phenotype with high accuracy at a rate of several hundred animals per hour. Compared to manual phenotyping and screening experiments that typically require many months to complete, our system can perform such experiments without human intervention in a few days to a few weeks. For cell laser ablation, although it requires additional processes, such as aiming at the target neurons and laser firing, the multiplex processing of worms enables ablation of hundreds of worms per hour, which is at least one order of magnitude higher than that of manual method (a few worms per hour). Moreover, the success rate and the throughput do not suffer as the number of the neurons required to be ablated increases because of complete automation of the entire process. This microfluidics-enabled computer-automated approach provides the means for many high-throughput discovery and fundamental studies.

Another notable contribution of the thesis is to develop the numerical models and the experimental methods to characterize the microdevices. The models developed to explore fluidic motion, pressure distribution, and heat transfer successfully facilitated the understanding of the devices and aided the design of the devices. Moreover, to further aid optimization of the devices in the future, we developed novel temperature and

pressure measurement methods in microsystems. In collaboration with Jaekyu Cho in Dr. Victor Breedveld's group, we demonstrated for the first time that tracking Brownian motion of nanoparticles can be used for 3-D *in situ* thermometry in microfluidic devices. This method is easy to use and offers accurate temperature measurements with superior reproducibility. In collaboration with Hyewon Lee, I also developed an on-chip pressure measurement method using volume displacement of fluorescent particle suspension. This method does not require expensive off-chip equipment or a complicated fabrication process, and is simple to use. These measurement methods with the numerical models will greatly assist future development of microsystems.

Overall, this thesis shows how microfluidics can be coupled with computer automation as powerful tools for a wide range of biological research. We envision that the technological development conceived in this thesis will establish a solid basis for continuous improvement of the microsystems.

6.2 Recommendations for future work

The work presented in this dissertation serves as a proof of concepts and provides a foundation for continued development of the microsystems. Although we demonstrated the capability of the microsystems to perform high-throughput imaging, phenotyping, and laser cell ablation of *C. elegans*, further efforts on improvement of the microsystems will greatly enhance the performance of the systems and enable this technology to impact a broader range of biological study. Proposed future work includes systematic study of the effect of cooling on *C. elegans*, optimizing the microsystems to improve throughput, improving user-friendliness of the microsystems, and adapting the systems for other organisms and applications.

This thesis is the first to demonstrate the use of on-chip cooling to completely immobilize *C. elegans* for high-resolution microscopy and laser ablation. We also

proved brief cooling does not affect animal's overall viability and the phenotypes that we were interested. However, long term or repeated cooling may affect the development of younger animals. Therefore, better understanding of cooling is necessary to expand the repertoire of the microsystem's application. Systematic study for cooling should include characterization of the critical temperature where the animal stops its movement. The critical temperature could vary depending on the developmental stage of the worms. For example, young adults with large motility may need a lower temperature to be immobilized than early larva stages. Therefore, the temperature should be characterized for each stage of animals. Also, physiological effects of cooling on the animals need to be investigated in detail. Many indicators, such as time to egg-laying, number of progeny, and pharyngeal pumping rates could be measured and compared. This study will provide guide lines for proper immobilization using cooling while minimizing its potential side effects.

In regards to rapid immobilization by cooling, the novel microfluidic components, and the first-generation processing algorithm, the existing hardware and software already achieved high-throughput that is at least one order of magnitude higher than that of conventional methods. However, the throughput of the microsystems can be further improved to process larger quantity of samples. This thesis demonstrated the possibility of improving throughput by using a multiplex device for laser ablation. Advanced multiplexing, such as simultaneous loading of worms in a larger channel array and simultaneous imaging of multiple worms with one image acquisition step, could further increase throughput. Additionally, the imaging and processing algorithm can be optimized and eventually written in other computer languages (e.g. Visual C) to reduce the processing time.

For the microsystems to make a large impact on biological research, they must be usable by non-engineers. In other words, these systems need to be easy to operate and robust. To improve the usability of the microsystems, three components of the systems

need to be addressed. First, the device design and fabrication method could be simplified to improve the robustness of the device. For instance, reducing the number of layers of the devices while including all the necessary features will drastically reduce device failure rate. Second, off-chip components for supporting the microdevices including the Peltier cooling and the pressure driven injection system can be further optimized to improve system robustness. The current cooling system, in particular, often malfunctions because the temperature of the coolant in the device varies depending on many factors, such as flow rate and surrounding temperature. Development of temperature feed-back control could potentially address this issue. Lastly, easy-to-use and robust interfaces that connect the microdevices and off-chip components will significantly improve usability of the systems. Currently, the devices are connected to the off-chip components through metal pins and tubings. Connecting off-chip components to the device and setting up the device on the x-y-z-stage requires careful handling and undermines robustness of the system. Better packaging technology will greatly improve usability of the microsystems.

Lastly, applications in many biological areas can be demonstrated to expand the application portfolio of the technology developed in this thesis. As a proof-of-concept set of experiments, this thesis work developed the microsystems for imaging, sorting, and laser ablation of *C. elegans*. However, this technology is not limited to *C.elegans*. It should be useful for other model organisms with some modifications, because the concepts and design rules of the microsystems can also be applicable for other small organisms. For example, the embryo trap device can be modified to trap *Drosophilia* embryos with desired orientation for fluorescence imaging and laser ablation. In addition, the device can be combined with other microfluidic devices to perform complicated tasks, such as long-term imaging and drug screening. Therefore, the microsystems and methodologies conceived in the thesis work could have broader implications in many other biological research areas.

APPENDIX A

EQUIPMENTS UTILIZED DURING IMAGING AND PHENOTYPING EXPERIMENTS

- Photolithograph tools: a spin coater, a profilometer, an alignment and UV exposure tool.
- Peltier cooler: PJT-5 30 mm square and PJT-6 40 mm square peltier coolers.
- Aluminum tubing: Aluminum alloy 3003 tubing with .0345" ID and .063" OD.
- Digital I/O Card: USB 6501 digital I/O card purchased from National Instruments.
- Solenoid Valves: Solenoid valves from Hargraves Fluidics.
- Valve Manifold: Custom designed.
- Air Pressure Manifold: Custom designed.
- Amplifier Card: Custom designed to amplify signal from the 6501 I/O card.
- Microscope: Leica DM4500 or equivalent.
- Camera: Hamamatsu C9100-13 EM CCD or equivalent.
- Light Source: Mercury arc lamp.
- Lenses: 10 X (air, NA = 0.3) and 100 X (oil, NA = 1.4), or any microscope lens suitable for the application

APPENDIX B

AUTOCAD DESIGN OF THE IMAGING AND PHENOTYPING DEVICE

a) Flow channel layer - SU8

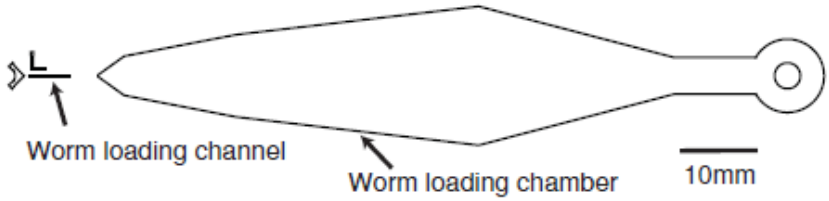

b) Flow channel layer - AZ

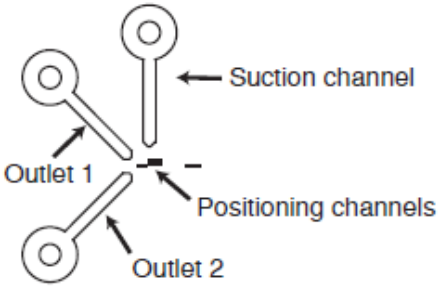

c) Control layer

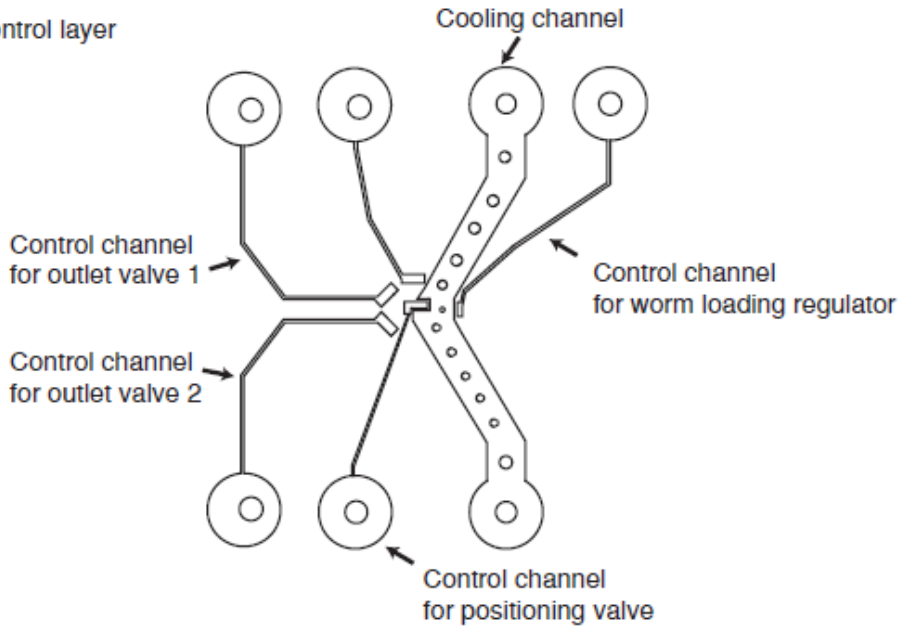

APPENDIX C

AUTOCAD DESIGN OF THE FILTERING DEVICE

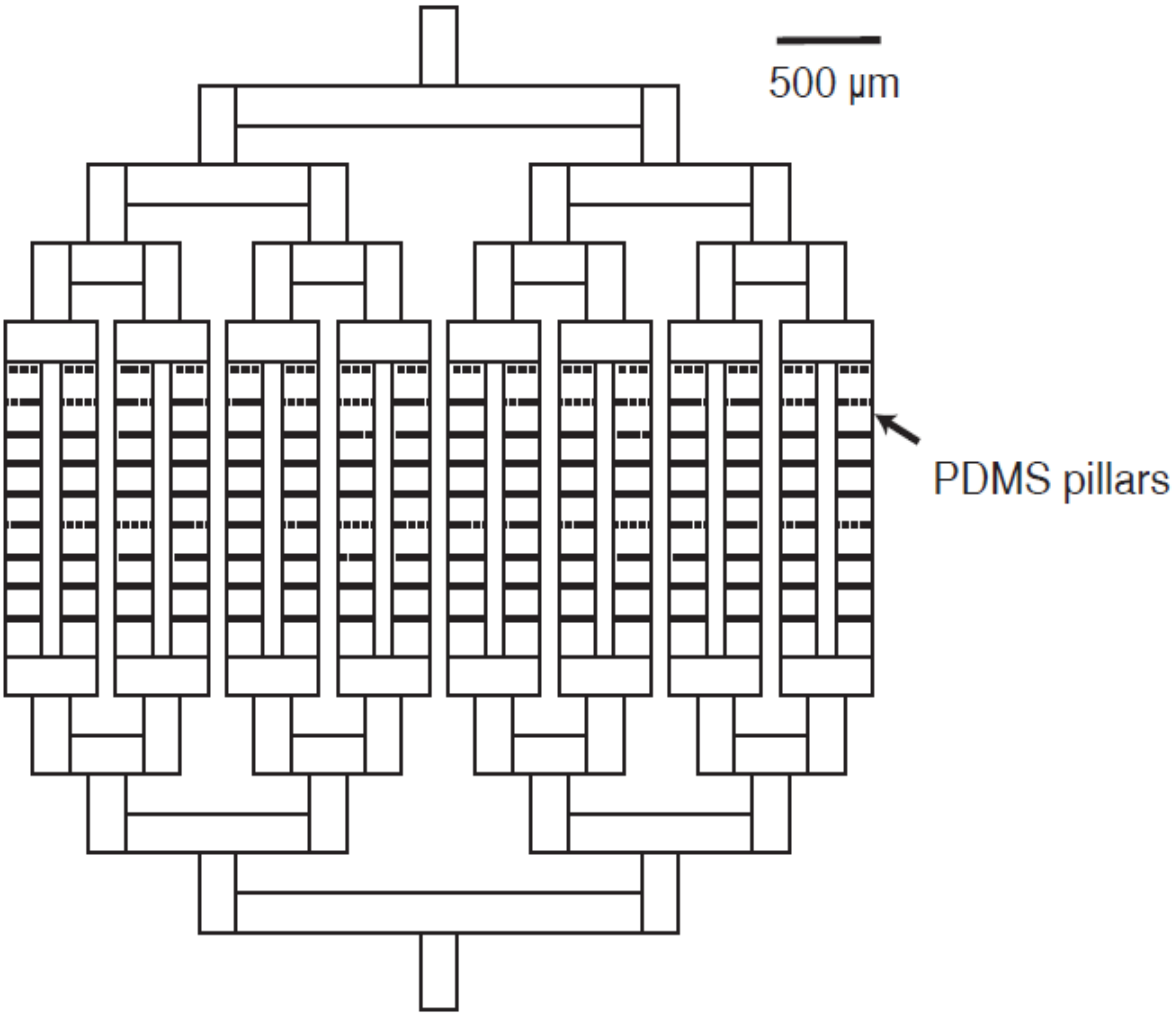

APPENDIX D

MATLAB CODE FOR CELL LASER ABLATION

```
%==========================================================
%Date:          2009-2-15
%Author:        Kwanghun Chung
%Description:   Image processing for laser ablation
%Requires:      bypass.m
%==========================================================

clear y rgLabeled rgObject sorted_Area_two matrix_Area_two matrix_Area sorted_Area
uiNumObj;
clear temp sorted_Distance Distance Avg_Distance z_1_std_z z_1_std_z_x z_1_std_z_y
z_2_std_z;
clear z_2_std_z_x z_2_std_z_y a b c d e Z_1_std_z Z_2_std_z b_max c_max d_max
e_max;
clear b_std c_std d_std e_std b_max c_max d_max e_max l l_z1 l_z1_max l_z2
l_z2_max;
clear Max_neuron1 Max_neuron2 max_neuron1 max_neuron2 Object1 Object2
c_max_1;
clear c_max_2 c_std_temp neuron1 neuron2 pks locs temp_1 temp_2 x_1_std_z_temp
y_1_std_z_temp x_2_std_z_temp y_2_std_z_temp;

uiStack = squeeze(uiStack);
%flattening z-stack
stdz=squeeze(std(double(uiStack(:,:,:)),[],3));
figure(1); imshow(stdz,[]);
```

```
%applying bypass filter and display the processed image
b=bpass(stdz,1,10);
figure(2); imshow(b,[]);
%applying a threshold
temp=max(b(:));
Temp=0.08;
BW = roicolor(b,Temp*temp,temp);
figure(3); imshow(BW,[]);
%identifying all the objects
[rgLabeled,uiNumObj] = bwlabel(BW,8);
rgObject = regionprops(rgLabeled,'all');

%eliminating fat-granules and other small fluorescent objects
if (length(rgObject) <= 2)
else
   if (length(rgObject)<=6) %eliminating by size
      for (i = 1 : length(rgObject))
         matrix_Area(i)=rgObject(i).Area;
         sorted_Area=sort(matrix_Area(:), 'descend');
      end
      for (i = 1 : length(rgObject))
         if(rgObject(i).Area <= sorted_Area(3))
            rgLabeled(rgObject(i).PixelIdxList) = 0;
         end
      end
   else
      for (i = 1 : length(rgObject)) %eliminating by distance
```

```
        clear Distance sorted_Distance Avg_Distance;
        for (j = 1 : length(rgObject))
            Distance(j)=((rgObject(i).Centroid(1)-
rgObject(j).Centroid(1))^2+(rgObject(i).Centroid(2)-rgObject(j).Centroid(2))^2)^0.5;
        end
        sorted_Distance=sort(Distance(:), 'ascend');
        Avg_Distance=mean(sorted_Distance(1 : 6));

        if(Avg_Distance < 35)
            rgLabeled(rgObject(i).PixelIdxList) = 0;
        end
    end

    clear rgObject uiNumObj;
    [rgLabeled,uiNumObj] = bwlabel(rgLabeled,8);
    rgObject = regionprops(rgLabeled,'all');
    if (uiNumObj >= 3)
        for (i = 1 : length(rgObject))
            matrix_Area_two(i)=rgObject(i).Area;
        end
        sorted_Area_two=sort(matrix_Area_two(:), 'descend');
        for (i = 1 : length(rgObject))
            if(rgObject(i).Area <= sorted_Area_two(3))
                rgLabeled(rgObject(i).PixelIdxList) = 0;
            end
        end
    else
```

```
        end
    end
    % display the identified neurons
    figure(4); imshow(rgLabeled);
    clear rgObject uiNumObj;
    [rgLabeled,uiNumObj] = bwlabel(rgLabeled,8);
    rgObject = regionprops(rgLabeled,'all');
end

after_area_f=bwlabel(rgLabeled,8);
stats=regionprops(after_area_f,'centroid');
position_std_z=[stats.Centroid];

% Identify two neurons in close x,y position.
if (uiNumObj <= 1 || ((position_std_z(1,1)-position_std_z(1,3))^2>1500))

    after_area_f=bwlabel(rgLabeled,8);
    stats=regionprops(after_area_f,'centroid');
    position_std_z=[stats.Centroid];
    x_1_std_z_temp=nearest(position_std_z(1,1));
    y_1_std_z_temp=nearest(position_std_z(1,2));

    c=zeros(30,N_stack2);
    for i=1:30
        for j=1:N_stack2
            c(i,j)=std(double(uiStack(y_1_std_z_temp-15+i,x_1_std_z_temp-
15:x_1_std_z_temp+15,j)));
```

```
    end
end
for (i=1:N_stack2)
    c_std_temp(i)=std(c(:,i));
end
y=smooth(c_std_temp);
[pks,locs]=findpeaks(y);
c_max_1=max(max(c(:,locs(1)-3:locs(1)+3)));
c_max_2=max(max(c(:,locs(2)-3:locs(2)+3)));
for (i=1:30)
    for(j=locs(1)-4:locs(1)+4)
        if (c(i,j)>=(c_max_1*0.6))
            c(i,j)=c_max_1*0.6;
        else
        end
    end
end
for (i=1:30)
    for(j=locs(2)-4:locs(2)+4)
        if (c(i,j)>=(c_max_2*0.6))
            c(i,j)=c_max_2*0.6;
        else
        end
    end
end
for (i=1:N_stack2)
    c_std(i)=std(c(:,i));
```

```
end
clear pks locs;
y=smooth(c_std);
[pks,locs]=findpeaks(y);
figure(7); imshow(c,[]);


temp_1=max(max(max(uiStack(y_1_std_z_temp-
20:y_1_std_z_temp+20,x_1_std_z_temp-20:x_1_std_z_temp+20,locs(1)))));
Temp=0.6;
BW = roicolor(uiStack(y_1_std_z_temp-20:y_1_std_z_temp+20,x_1_std_z_temp-
20:x_1_std_z_temp+20,locs(1)),Temp*temp_1,temp_1);

neuron1 = bwlabel(BW,8);
neuron1.stats = regionprops(neuron1,'centroid');
position_std_z=[neuron1.stats.Centroid];
x_1_std_z=nearest(position_std_z(1,1))+x_1_std_z_temp-20;
y_1_std_z=nearest(position_std_z(1,2))+y_1_std_z_temp-20;
z_1_std_z=locs(1);


temp_2=max(max(max(uiStack(y_1_std_z_temp-
20:y_1_std_z_temp+20,x_1_std_z_temp-20:x_1_std_z_temp+20,locs(2)))));
Temp=0.6;
BW = roicolor(uiStack(y_1_std_z_temp-20:y_1_std_z_temp+20,x_1_std_z_temp-
20:x_1_std_z_temp+20,locs(2)),Temp*temp_2,temp_2);
```

```
    neuron2 = bwlabel(BW,8);
    neuron2.stats = regionprops(neuron2,'centroid');
    position_std_z=[neuron2.stats.Centroid];
    x_2_std_z=nearest(position_std_z(1,1))+x_1_std_z_temp-20;
    y_2_std_z=nearest(position_std_z(1,2))+y_1_std_z_temp-20;
    z_2_std_z=locs(2);
else
    after_area_f=bwlabel(rgLabeled,8);
    stats=regionprops(after_area_f,'centroid');
    position_std_z=[stats.Centroid]; %[y,x]
    x_1_std_z_temp=nearest(position_std_z(1,1));
    y_1_std_z_temp=nearest(position_std_z(1,2));
    x_2_std_z_temp=nearest(position_std_z(1,3));
    y_2_std_z_temp=nearest(position_std_z(1,4));

    l=((x_1_std_z_temp-x_2_std_z_temp)^2+(y_1_std_z_temp-
y_2_std_z_temp)^2)^0.5/512*80;

    if (l > 10)
        Object1=sum(sum(stdz(y_1_std_z_temp-10:y_1_std_z_temp+10,x_1_std_z_temp-
10:x_1_std_z_temp+10)));
        Object2=sum(sum(stdz(y_2_std_z_temp-10:y_2_std_z_temp+10,x_2_std_z_temp-
10:x_2_std_z_temp+10)));
        if (Object1 > Object2)
            y_1_std_z_temp=y_1_std_z_temp;
            x_1_std_z_temp=x_1_std_z_temp;
        else
```

```
        y_1_std_z_temp=y_2_std_z_temp;
        x_1_std_z_temp=x_2_std_z_temp;
    end
    c=zeros(30,N_stack2);
    for i=1:30
        for j=1:N_stack2
            c(i,j)=std(double(uiStack(y_1_std_z_temp-15+i,x_1_std_z_temp-
15:x_1_std_z_temp+15,j)));
        end
    end
    for (i=1:N_stack2)
        c_std_temp(i)=std(c(:,i));
    end
    y=smooth(c_std_temp);
    [pks,locs]=findpeaks(y);
    c_max_1=max(max(c(:,locs(1)-3:locs(1)+3)));
    c_max_2=max(max(c(:,locs(2)-3:locs(2)+3)));
    for (i=1:30)
        for(j=locs(1)-4:locs(1)+4)
            if (c(i,j)>=(c_max_1*0.6))
                c(i,j)=c_max_1*0.6;
            else
            end
        end
    end
    for (i=1:30)
        for(j=locs(2)-4:locs(2)+4)
```

```
        if (c(i,j)>=(c_max_2*0.6))
            c(i,j)=c_max_2*0.6;
        else
        end
      end
    end
    for (i=1:N_stack2)
      c_std(i)=std(c(:,i));
    end
    clear pks locs;
    y=smooth(c_std);
    [pks,locs]=findpeaks(y);
    figure(7); imshow(c,[]);


    temp_1=max(max(max(uiStack(y_1_std_z_temp-
20:y_1_std_z_temp+20,x_1_std_z_temp-20:x_1_std_z_temp+20,locs(1)))));
    Temp=0.6;
    BW = roicolor(uiStack(y_1_std_z_temp-20:y_1_std_z_temp+20,x_1_std_z_temp-
20:x_1_std_z_temp+20,locs(1)),Temp*temp_1,temp_1);


    neuron1 = bwlabel(BW,8);
    neuron1.stats = regionprops(neuron1,'centroid');
    position_std_z=[neuron1.stats.Centroid];
    x_1_std_z=nearest(position_std_z(1,1))+x_1_std_z_temp-20;
    y_1_std_z=nearest(position_std_z(1,2))+y_1_std_z_temp-20;
    z_1_std_z=locs(1);
```

```
        temp_2=max(max(max(uiStack(y_1_std_z_temp-
20:y_1_std_z_temp+20,x_1_std_z_temp-20:x_1_std_z_temp+20,locs(2)))));
        Temp=0.6;
        BW = roicolor(uiStack(y_1_std_z_temp-20:y_1_std_z_temp+20,x_1_std_z_temp-
20:x_1_std_z_temp+20,locs(2)),Temp*temp_2,temp_2);

        neuron2 = bwlabel(BW,8);
        neuron2.stats = regionprops(neuron2,'centroid');
        position_std_z=[neuron2.stats.Centroid];
        x_2_std_z=nearest(position_std_z(1,1))+x_1_std_z_temp-20;
        y_2_std_z=nearest(position_std_z(1,2))+y_1_std_z_temp-20;
        z_2_std_z=locs(2);
    else
    x_1_std_z=x_1_std_z_temp;
    y_1_std_z=y_1_std_z_temp;
    x_2_std_z=x_2_std_z_temp;
    y_2_std_z=y_2_std_z_temp;
        if (l<=3.5)
            for i=5:50
                l_z1(i)=mean(mean(uiStack(y_1_std_z-5:y_1_std_z+5,x_1_std_z-
5:x_1_std_z+5,i)));
            end
            [Maxintensity,l_z1_max]=max(l_z1);
            for i=5:50
```

```
            l_z2(i)=mean(mean(uiStack(y_2_std_z-5:y_2_std_z+5,x_2_std_z-
5:x_2_std_z+5,i)));
        end
        [Maxintensity,l_z2_max]=max(l_z2);

        z_1_std_z=l_z1_max+2;
        z_2_std_z=l_z2_max+2;


    else

        c=zeros(30,N_stack2);
        for i=1:30
            for j=5:N_stack2
                c(i,j)=std(double(uiStack(y_1_std_z_temp-15+i,x_1_std_z_temp-
15:x_1_std_z_temp+15,j)));
            end
        end
        c_max=max(c(:));
        for (i=1:30)
            for(j=5:N_stack2)
                if (c(i,j)>=(c_max*0.6))
                    c(i,j)=c_max*0.6;
                else
                end
            end
        end
```

```
figure(6); imshow(c,[]);
for (i=5:N_stack2)
   c_std(i)=std(c(:,i));
end

[Maxintensity,z_1_std_z]=max(c_std);

e=zeros(30,N_stack2);
for i=1:30
   for j=5:N_stack2
      e(i,j)=std(double(uiStack(y_2_std_z_temp-15+i,x_2_std_z_temp-
15:x_2_std_z_temp+15,j)));
   end
end
e_max=max(e(:));
for (i=1:30)
   for(j=5:N_stack2)
      if (e(i,j)>=(e_max*0.6))
         e(i,j)=e_max*0.6;
      else
      end
   end
end
figure(7); imshow(e,[]);
for (i=5:N_stack2)
   e_std(i)=std(e(:,i));
end
```

```
            [Maxintensity,z_2_std_z]=max(e_std);
        end
    end
end

if (x_1_std_z<x_2_std_z)
    X_1_std_z=x_1_std_z;
    X_2_std_z=x_2_std_z;
    Y_1_std_z=y_1_std_z;
    Y_2_std_z=y_2_std_z;
    Z_1_std_z=z_1_std_z;
    Z_2_std_z=z_2_std_z;
else X_1_std_z=x_2_std_z;
    X_2_std_z=x_1_std_z;
    Y_1_std_z=y_2_std_z;
    Y_2_std_z=y_1_std_z;
    Z_1_std_z=z_2_std_z;
    Z_2_std_z=z_1_std_z;
end

% Move the motorized stage to aim the first neuron

delta_X=(-X_laser+X_1_std_z)/512*840*1;
delta_Y=(+Y_laser-Y_1_std_z)/512*855*1;
delta_Z=Z_1_std_z*z_stack_stepsize2-N_stack2*z_stack_stepsize2*0.75+Z_laser;
```

```
Temp_x=strcat('M x=',int2str(delta_X));
Temp_y=strcat('M y=',int2str(delta_Y));
Temp_z=strcat('M z=',int2str(delta_Z));
Temp=strcat(Temp_x, Temp_y, Temp_z);
fprintf(CDevices.pSerial,Temp);
pause(1.5);

% Check aiming
trigger(CDevices.pCamera);
before_laser =getdata(CDevices.pCamera);
imshow(before_laser);
Cross=uint16(cross);

imshow(before_laser*10+Cross);
results(:,:,7)=before_laser*10+Cross;
pause(0.5);

% Firing laser to ablate the 1st neuron
for i=1:40
    valve_states=getvalue(pDaq2);
    putvalue(pDaq2,0);
    putvalue(pDaq2,1);
end
pause(0.5);

% Check
trigger(CDevices.pCamera);
```

```
before_laser=getdata(CDevices.pCamera);
imshow(before_laser);
Cross=uint16(cross);
imshow(before_laser*5+Cross);
results(:,:,8)=before_laser*10+Cross;

% Move stage to aim the 2nd neuron
if (X_laser-X_2_std_z)>0
   X_factor=1.04-(Y_2_std_z-Y_laser)*0.00008;
   Y_factor=(Y_2_std_z-Y_laser)*0.00002+1;
else
   X_factor=0.95+(Y_2_std_z-Y_laser)*0.000005;
   Y_factor=(Y_2_std_z-Y_laser)*0.000004+0.99;
end
delta_X=(-X_laser+X_2_std_z)/512*840*X_factor;
delta_Y=(+Y_laser-Y_2_std_z)/512*855*Y_factor;
delta_Z=Z_2_std_z*z_stack_stepsize2-N_stack2*z_stack_stepsize2*0.75+Z_laser;

Temp_x=strcat('M x=',int2str(delta_X));
Temp_y=strcat('M y=',int2str(delta_Y));
Temp_z=strcat('M z=',int2str(delta_Z));
Temp=strcat(Temp_x, Temp_y, Temp_z);
fprintf(CDevices.pSerial,Temp);
pause(0.5);

% Check
trigger(CDevices.pCamera);
```

```
before_laser=getdata(CDevices.pCamera);
imshow(before_laser);
Cross=uint16(cross);
results(:,:,9)=before_laser*10+Cross;
imshow(before_laser*10+Cross);
pause(0.5);

% Firing laser to ablate the 2nd neuron
for i=1:40
    valve_states=getvalue(pDaq2);
    putvalue(pDaq2,0);
    putvalue(pDaq2,1);
end
pause(0.5);

% Check
trigger(CDevices.pCamera);
before_laser=getdata(CDevices.pCamera);
imshow(before_laser);
Cross=uint16(cross);
imshow(before_laser*5+Cross);
results(:,:,8)=before_laser*10+Cross;
```

APPENDIX E

AUTOCAD DESIGN OF THE LASER ABLATION DEVICE

a) Flow channel layer - mask #1

b) Flow channel layer - mask #2

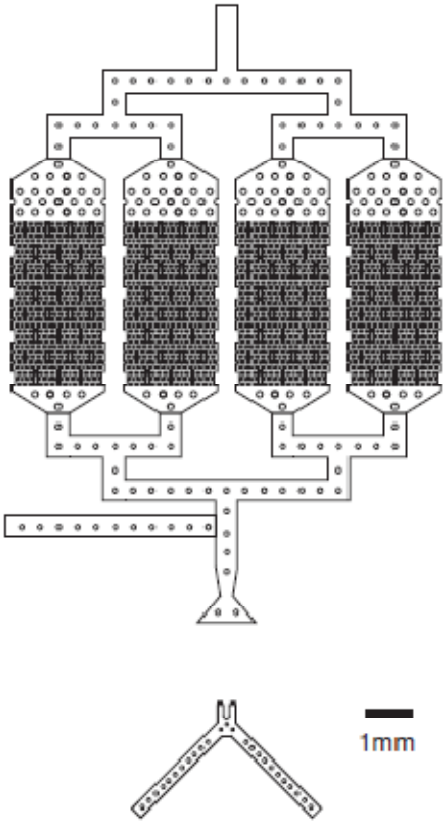

c) Control valve layer

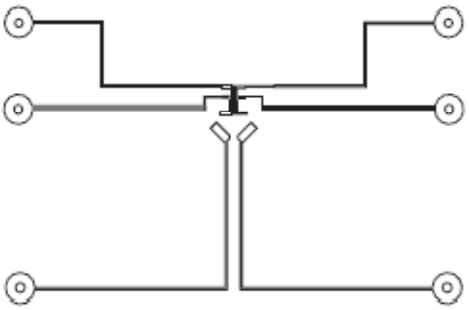

d) Cooling layer

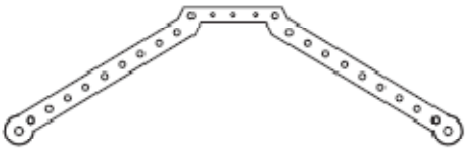

APPENDIX F

AUTOCAD DESIGN OF THE DEVICE FOR TEMPERATURE GRADIENT

a) The first layer - particle loading layer

b) The second layer - temperature control layer

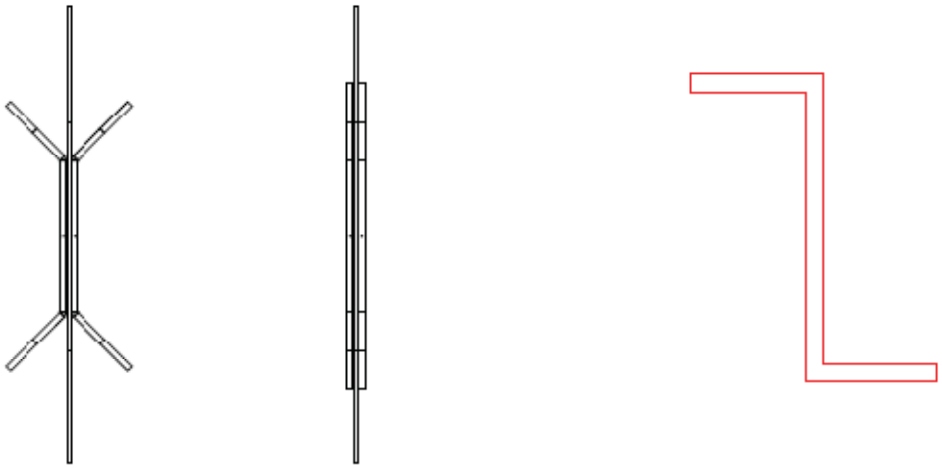

2 D temporaturo gradient device

3 D temporaturo gradient device

1mm

c) Overlay of two layers

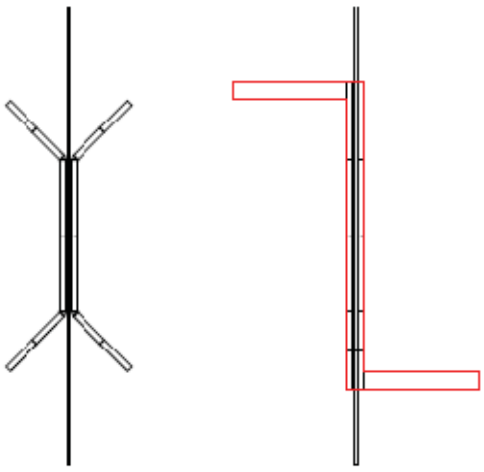

APPENDIX G

AUTOCAD DESIGN OF PRESSURE SENSOR DEVICES

a) The first layer - flow channel and valve layer (SU8-2025)

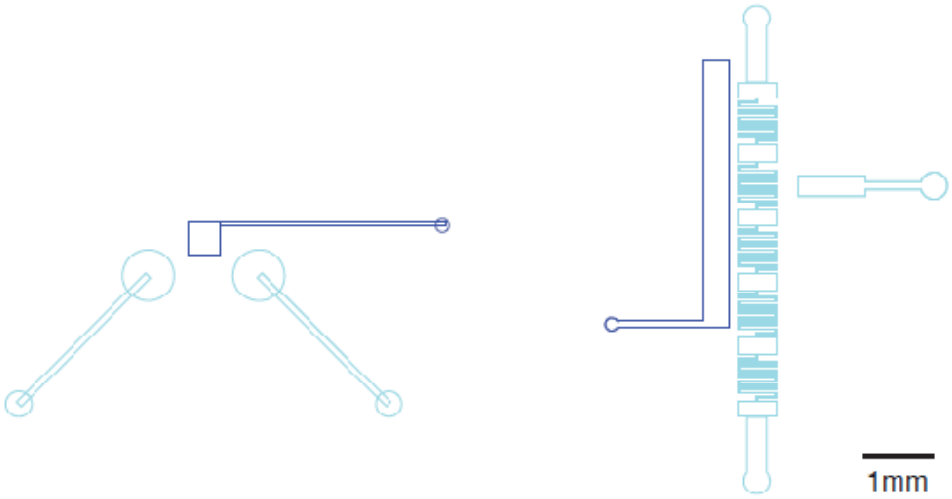

Direct, remote
pressure measurement device

Multiplex pressure
measurement device

b) The second layer (sensor layer) - transferring channel (SU8-2010)

c) The second layer (sensor layer) - circular sensor (SU8-2025)

d) The second layer (sensor layer) - AZ50XT

Direct, remote
pressure measurement device

Multiplex pressure
measurement device

e) Overlay of all the masks

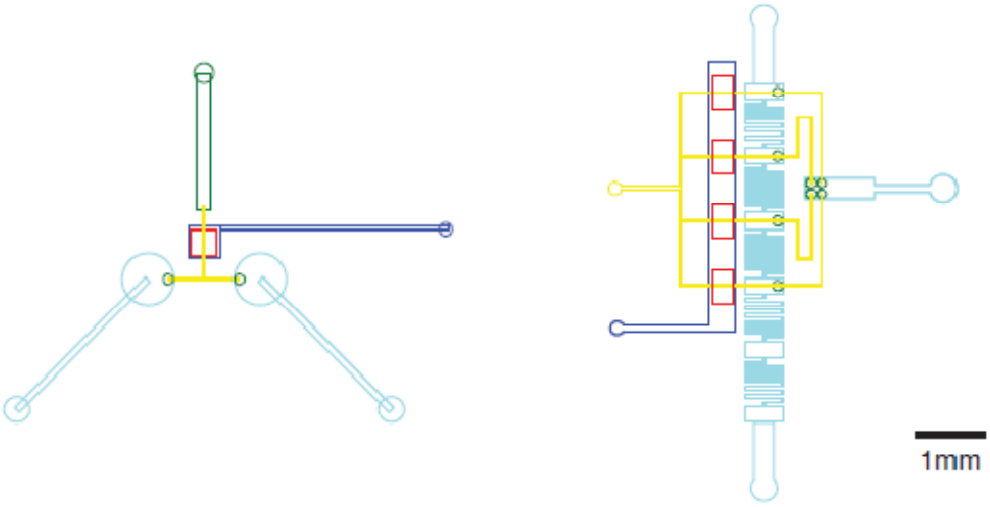

Direct, remote
pressure measurement device

Multiplex pressure
measurement device

APPENDIX H

MATLAB CODE FOR PRESSURE MEASUREMENT

```
%==========================================================================
% Date:          2009-1-15
% Author:        Kwanghun Chung
% Description: Image processing for pressure measurement
% Requires:     initialize.m, bypass.m, pkfnd.m
% Notes:         Initialize.m, bypass.m, and pkfnd.m are developed by David Grier, John
Crocker, and Eric Weeks. The codes can be found in the following website:
http://physics.georgetown.edu/matlab/code.html
%==========================================================================

clear all;

 %% Grab Z-stack
Date='010109';  % Date
pressure=5; % applied pressure (psi)
z_stack_stepsize=20 % 2μm

for k=1:3
   for(i=1:30)
      trigger(CDevices.pCamera);
      fscanf(CDevices.pSerial);
      CX3695ZStackImageA(:,:,:,i)= getdata(CDevices.pCamera);
      temp=z_stack_stepsize*i;
      Temp=strcat('M z=',int2str(temp));
```

```
        fprintf(CDevices.pSerial,Temp);
        pause(0.05);
    end

    fprintf(CDevices.pSerial,'M z=0');
    uiStack=CX3695ZStackImageA;
    strFile=cat(2,'C:\Kwanghun Chung\pressure
sensor\',Date,'_',int2str(pressure),'_',int2str(k),'.mat');
    save(strFile,'uiStack');
end

%% Image processing

temp_3D = squeeze(uiStack);

for l=1:20;
    clear L Stats position Distance_max Distance Distance Min_Distance x_Center
y_Center
    clear Min_Radius sort_SmallDistance sort_SmallDistance_descend SmallDistance
Afterpk ;
    c=255/65535;
    Temp=temp_3D(:,:,l);
    figure(1); imshow(Temp); % display a raw image
    temp_im=double(uint8(Temp*c/2));
    % applying bypass filter and display the processed image
    b = bpass(temp_im,1,2);
    colormap('gray'),figure(2);imshow(b);
```

```
% identify in-focus particles
d=max(b(:));
pk=pkfnd(b,d*0.3,2);
Afterpk=zeros(512);
length=size(pk);
  for (i=1:length(1))
    Afterpk(pk(i,2),pk(i,1))=1;
  end
figure(4);imshow(Afterpk); % display identified in-focus particles
% identify x,y position of the in-focus particles
L=bwlabel(Afterpk);
stats=regionprops(L,'centroid');
position=[stats.Centroid];
N_particle=size(position)/2;
% find the center of the sensor
for (j=1:60)
   for (k=1:60)
      x_center=256-30+j;
      y_center=256-30+k;
      for i=1:N_particle(1,2)
         p_1x=position(1,i*2-1); p_1y=position(1,i*2);
         Distance(i)=((x_center-p_1x)^2+(y_center-p_1y)^2)^0.5;
      end
      Distance_MAX(k)=max(Distance(:));
   end
   [Min_Distance,k_position]=min(Distance_MAX);
   Distance_Min(j)=Min_Distance;
```

```
    end
    [Min_Radius,j_position]=min(Distance_Min);
          %the identified center
         x_Center=256-30+j_position;
         y_Center=256-30+k_position;

    % find minimum diameter of a circle that encloses all the in-focus particles

    for i=1:N_particle(1,2)
       p_1x=position(1,i*2-1); p_1y=position(1,i*2);
       SmallDistance(i)=((x_Center-p_1x)^2+(y_Center-p_1y)^2)^0.5;
    end

    sort_SmallDistance_descend=sort(SmallDistance(:),'descend');

Diameter(l)=(sort_SmallDistance_descend(1)+sort_SmallDistance_descend(2)+sort_Sma
llDistance_descend(3))/3;

    % overlay of the circle on the in-focus particle image
    for (i=1:512)
       for (j=1:512)
          if (((i-x_Center)^2+(j-y_Center)^2)^0.5>(Diameter(l)-1)&&((i-x_Center)^2+(j-
y_Center)^2)^0.5<(Diameter(l)+1))
             Afterpk(j,i)=1;
          else
          end
       end
```

```
    end

    figure(5); imshow(Afterpk)
end
```

APPENDIX I

NUMBER OF ANIMALS IN INPUT AND OUTPUTS IN HIGH-THROUGHPUT AUTOMATED SORTING EXPERIMENTS

Table A.1. Number of animals in input and outputs in high-throughput automated sorting experiments. The rates of false positive, false negative and enrichment are calculated from these numbers.
PQR-on vs. PQR-off: sorting of PQR GFP-positive animals versus PQR GFP-negative animals
WT vs. *unc-16*: sorting based on synaptic features

PQR-on vs. PQR-off											
	total # input		**output 1**		**output 2**		**total # sorted**	**PQR-on in mix**	**false pos.**	**false neg.**	**enrichment**
			on as on	**off as on**	**off as off**	**on as off**					
trial 1	~2500		640	86	1601	119	2446	31.0%	11.8%	6.9%	284%
trial 2	~2100		629	62	1314	79	2084	34.0%	9.0%	5.7%	268%
trial 3	~2500		794	61	1541	104	2500	35.9%	7.1%	6.3%	259%
trial 4	~1800		508	39	1176	73	1796	32.3%	7.1%	5.8%	287%
Average									**8.8 ± 2.2%**	**6.2 ± 0.6%**	**274 ± 14%**
WT vs. *unc-16*											
	total # input	**% mutant**	**output 1**		**output 2**		**total # sorted**	***unc* in mix**	**false pos.**	**false neg.**	**enrichment**
			***unc* as unc**	**WT as *unc***	**WT as WT**	***unc* as WT**					
trial 1	~1400	~30%	410	2	930	29	1371	32.0%	0.5%	3.0%	311%
trial 2	~1400	~25%	308	32	971	21	1332	24.7%	9.4%	2.1%	367%
trial 3	~1400	~25%	309	37	1030	24	1400	23.8%	10.7%	2.3%	375%
Average									**6.9 ± 5.6%**	**2.5 ± 0.5%**	**350 ± 35%**

REFERENCES

1. Kaletta, T. & Hengartner, M.O. Finding function in novel targets: C-elegans as a model organism. *Nature Reviews Drug Discovery* **5**, 387-398 (2006).
2. Jones, A.K., Buckingham, S.D. & Sattelle, D.B. Chemistry-to-gene screens in Caenorhabditis elegans. *Nature Reviews Drug Discovery* **4**, 321-330 (2005).
3. Dove, A. Screening for content - the evolution of high throughput. *Nature Biotechnology* **21**, 859-864 (2003).
4. de Bono, M., Tobin, D.M., Davis, M.W., Avery, L. & Bargmann, C.I. Social feeding in Caenorhabditis elegans is induced by neurons that detect aversive stimuli. *Nature* **419**, 899-903 (2002).
5. Sulston, J.E. & Horvitz, H.R. Post-Embryonic Cell Lineages of Nematode, Caenorhabditis-Elegans. *Developmental Biology* **56**, 110-156 (1977).
6. Dupuy, D. *et al.* Genome-scale analysis of in vivo spatiotemporal promoter activity in Caenorhabditis elegans. *Nat Biotech* **25**, 663-668 (2007).
7. Kamath, R.S. *et al.* Systematic functional analysis of the Caenorhabditis elegans genome using RNAi. *Nature* **421**, 231-237 (2003).
8. Kamath, R.S. & Ahringer, J. Genorne-wide RNAi screening in Caenorhabditis elegans. *Methods* **30**, 313-321 (2003).
9. Genome sequence of the nematode C-elegans: A platform for investigating biology. *Science* **282**, 2012-2018 (1998).
10. Brenner, S. The genetics of *Caenorhabditis elegans*. *Genetics* **77**, 71-94 (1974).
11. White, J.G., Southgate, E., Thomson, J.N. & Brenner, S. The Structure of the Nervous-System of the Nematode Caenorhabditis-Elegans. *Philosophical Transactions of the Royal Society of London Series B-Biological Sciences* **314**, 1-340 (1986).
12. Maeda, I., Kohara, Y., Yamamoto, M. & Sugimoto, A. Large-scale analysis of gene function in Caenorhabditis elegans by high-throughput RNAi. *Current Biology* **11**, 171-176 (2001).
13. Dupuy, D. *et al.* Genome-scale analysis of in vivo spatiotemporal promoter activity in Caenorhabditis elegans. *Nature Biotechnology* **25**, 663-668 (2007).
14. Troemel, E.R., Kimmel, B.E. & Bargmann, C.I. Reprogramming chemotaxis responses: Sensory neurons define olfactory preferences in C. elegans. *Cell* **91**, 161-169 (1997).
15. Harbinder, S. *et al.* Genetically targeted cell disruption in Caenorhabditis elegans. *Proceedings of the National Academy of Sciences of the United States of America* **94**, 13128-13133 (1997).
16. Bargmann, C.I. & Avery, L. Laser killing of cells in Caenorhabditis elegans. *Methods in Cell Biology* **48**, 225-250 (1995).
17. Bargmann, C.I., Hartwieg, E. & Horvitz, H.R. Odorant-Selective Genes and Neurons Mediate Olfaction in C. elegans. *Cell* **74**, 515-527 (1993).
18. Avery, L. & Horvitz, R. Pharyngeal Pumping Continues after Laser Killing of the Pharyngeal Nervous-System of C-Elegans. *Neuron* **3**, 473-485 (1989).
19. Brenner, S. The genetics of Caenorhabditis elegans. *Genetics* **77**, 71-94 (1974).

20. Bargmann, C.I. High-throughput reverse genetics: RNAi screens in Caenorhabditis elegans. *Genome Biol* **2**, 1005 (2001).
21. Sonnichsen, B. *et al.* Full-genome RNAi profiling of early embryogenesis in Caenorhabditis elegans. *Nature* **434**, 462-469 (2005).
22. Bao, Z.R. *et al.* Automated cell lineage tracing in Caenorhabditis elegans. *Proceedings of the National Academy of Sciences of the United States of America* **103**, 2707-2712 (2006).
23. Ashrafi, K. *et al.* Genome-wide RNAi analysis of Caenorhabditis elegans fat regulatory genes. *Nature* **421**, 268-272 (2003).
24. de Bono, M. & Maricq, A.V. Neuronal substrates of complex behaviors in C. elegans. *Annu Rev Neurosci* **28**, 451-501 (2005).
25. Sieburth, D. *et al.* Systematic analysis of genes required for synapse structure and function. *Nature* **436**, 510-517 (2005).
26. Fire, A. *et al.* Potent and specific genetic interference by double-stranded RNA in Caenorhabditis elegans. *Nature* **391**, 806-811 (1998).
27. Chalfie, M. *et al.* The Neural Circuit for Touch Sensitivity in Caenorhabditis elegans. *Journal of Neuroscience* **5**, 956-964 (1985).
28. Crowder, C.M., Shebester, L.D. & Schedl, T. Behavioral effects of volatile anesthetics in Caenorhabditis elegans. *Anesthesiology* **85**, 901-912 (1996).
29. Whitesides, G.M. The origins and the future of microfluidics. *Nature* **442**, 368-373 (2006).
30. DeMello, A.J. Microfluidics - DNA amplification moves on. *Nature* **422**, 28-29 (2003).
31. El-Ali, J., Sorger, P.K. & Jensen, K.F. Cells on chips. *Nature* **442**, 403-411 (2006).
32. Janasek, D., Franzke, J. & Manz, A. Scaling and the design of miniaturized chemical-analysis systems. *Nature* **442**, 374-380 (2006).
33. Psaltis, D., Quake, S.R. & Yang, C.H. Developing optofluidic technology through the fusion of microfluidics and optics. *Nature* **442**, 381-386 (2006).
34. Squires, T.M. & Quake, S.R. Microfluidics: Fluid physics at the nanoliter scale. *Rev Mod Phys* **77**, 977-1026 (2005).
35. Stone, H.A., Stroock, A.D. & Ajdari, A. Engineering flows in small devices: Microfluidics toward a lab-on-a-chip. *Annu Rev Fluid Mech* **36**, 381-411 (2004).
36. Atencia, J. & Beebe, D.J. Controlled microfluidic interfaces. *Nature* **437**, 648-655 (2005).
37. Weigl, B.H. & Yager, P. Microfluidics - Microfluidic diffusion-based separation and detection. *Science* **283**, 346-347 (1999).
38. Lucchetta, E.M., Lee, J.H., Fu, L.A., Patel, N.H. & Ismagilov, R.F. Dynamics of Drosophila embryonic patterning network perturbed in space and time using microfluidics. *Nature* **434**, 1134-1138 (2005).
39. Fu, A.Y., Spence, C., Scherer, A., Arnold, F.H. & Quake, S.R. A microfabricated fluorescence-activated cell sorter. *Nature Biotechnology* **17**, 1109-1111 (1999).
40. Beebe, D.J., Mensing, G.A. & Walker, G.M. Physics and applications of microfluidics in biology. *Annu. Rev. Biomed. Eng.* **4**, 261-286 (2002).
41. Walker, G.M., Zeringue, H.C. & Beebe, D.J. Microenvironment design considerations for cellular scale studies. *Lab on a Chip* **4**, 91-97 (2004).

42. LaVan, D.A., McGuire, T. & Langer, R. Small-scale systems for in vivo drug delivery. *Nature Biotechnology* **21**, 1184-1191 (2003).
43. Huang, L.R., Cox, E.C., Austin, R.H. & Sturm, J.C. Continuous particle separation through deterministic lateral displacement. *Science* **304**, 987-990 (2004).
44. Pollack, M.G., Shenderov, A.D. & Fair, R.B. Electrowetting-based actuation of droplets for integrated microfluidics. *Lab on a Chip* **2**, 96-101 (2002).
45. Huber, D.L., Manginell, R.P., Samara, M.A., Kim, B.I. & Bunker, B.C. Programmed adsorption and release of proteins in a microfluidic device. *Science* **301**, 352-354 (2003).
46. Stroock, A.D., Dertinger, S.K., Whitesides, G.M. & Ajdari, A. Patterning flows using grooved surfaces. *Analytical Chemistry* **74**, 5306-5312 (2002).
47. Lucchetta, E.M., Munson, M.S. & Ismagilov, R.F. Characterization of the local temperature in space and time around a developing Drosophila embryo in a microfluidic device. *Lab on a Chip* **6**, 185-190 (2006).
48. Koh, C.G., Tan, W., Zhao, M.Q., Ricco, A.J. & Fan, Z.H. Integrating polymerase chain reaction, valving, and electrophoresis in a plastic device for bacterial detection. *Analytical Chemistry* **75**, 4591-4598 (2003).
49. Pal, R., Yang, M., Johnson, B.N., Burke, D.T. & Burns, M.A. Phase change microvalve for integrated devices. *Analytical Chemistry* **76**, 3740-3748 (2004).
50. Bruin, G.J.M. Recent developments in electrokinetically driven analysis on microfabricated devices. *Electrophoresis* **21**, 3931-3951 (2000).
51. Colyer, C.L., Tang, T., Chiem, N. & Harrison, D.J. Clinical potential of microchip capillary electrophoresis systems. *Electrophoresis* **18**, 1733-1741 (1997).
52. Karnik, R. *et al.* Electrostatic control of ions and molecules in nanofluidic transistors. *Nano Lett.* **5**, 943-948 (2005).
53. Lee, C.C. *et al.* Multistep synthesis of a radiolabeled imaging probe using integrated microfluidics. *Science* **310**, 1793-1796 (2005).
54. Thorsen, T., Maerkl, S.J. & Quake, S.R. Microfluidic large-scale integration. *Science* **298**, 580-584 (2002).
55. Unger, M.A., Chou, H.P., Thorsen, T., Scherer, A. & Quake, S.R. Monolithic microfabricated valves and pumps by multilayer soft lithography. *Science* **288**, 113-116 (2000).
56. Duffy, D.C., McDonald, J.C., Schueller, O.J.A. & Whitesides, G.M. Rapid prototyping of microfluidic systems in poly(dimethylsiloxane). *Analytical Chemistry* **70**, 4974-4984 (1998).
57. Whitesides, G.M., Ostuni, E., Takayama, S., Jiang, X.Y. & Ingber, D.E. Soft lithography in biology and biochemistry. *Annu. Rev. Biomed. Eng.* **3**, 335-373 (2001).
58. McDonald, J.C. *et al.* Fabrication of microfluidic systems in poly(dimethylsiloxane). *Electrophoresis* **21**, 27-40 (2000).
59. Ng, J.M.K., Gitlin, I., Stroock, A.D. & Whitesides, G.M. Components for integrated poly(dimethylsiloxane) microfluidic systems. *Electrophoresis* **23**, 3461-3473 (2002).
60. Quake, S.R. & Scherer, A. From micro- to nanofabrication with soft materials. *Science* **290**, 1536-1540 (2000).

61. Hong, J.W. & Quake, S.R. Integrated nanoliter systems. *Nature Biotechnology* **21**, 1179-1183 (2003).
62. Balagadde, F.K., You, L.C., Hansen, C.L., Arnold, F.H. & Quake, S.R. Long-term monitoring of bacteria undergoing programmed population control in a microchemostat. *Science* **309**, 137-140 (2005).
63. Khademhosseini, A., Langer, R., Borenstein, J. & Vacanti, J.P. Microscale technologies for tissue engineering and biology. *Proceedings of the National Academy of Sciences of the United States of America* **103**, 2480-2487 (2006).
64. Kikugawa, R. *et al.* Differentiation of COPAS-sorted non-endocrine pancreatic cells into insulin-positive cells in the mouse. *Diabetologia* **52**, 645-652 (2009).
65. Pulak, R. Large particle flow cytometry for study of cell clusters. *Cytometry Part A* **69A**, 405-406 (2006).
66. Pulak, R. Automated drug screening using zebrafish - Tutorial: COPAS XL allows for increased throughput. *Genetic Engineering News* **22**, 32 (2002).
67. Klassen, M.P. & Shen, K. Wnt Signaling Positions Neuromuscular Connectivity by Inhibiting Synapse Formation in C. elegans. *Cell* **130**, 704-716 (2007).
68. Hobert, O., Johnston, R.J. & Chang, S. Left-right asymmetry in the nervous system: The Caenorhabditis elegans model. *Nature Reviews Neuroscience* **3**, 629-640 (2002).
69. Zhao, H. A retrograde signal is involved in activity-dependent remodeling at a C. elegans neuromuscular junction. *Development* **127**, 1253-1266 (2000).
70. Zhen, M. & Jin, Y. The liprin protein SYD-2 regulates the differentiation of presynaptic termini in C. elegans. *Nature* **401**, 371-375 (1999).
71. Troemel, E.R., Sagasti, A. & Bargmann, C.I. Lateral signaling mediated by axon contact and calcium entry regulates asymmetric odorant receptor expression in C. elegans. *Cell* **99**, 387-398 (1999).
72. Shen, K. & Bargmann, C.I. The immunoglobulin superfamily protein SYG-1 determines the location of specific synapses in C-elegans. *Cell* **112**, 619-630 (2003).
73. Schaefer, A.M., Hadwiger, G.D. & Nonet, M.L. rpm-1, a conserved neuronal gene that regulates targeting and synaptogenesis in C-elegans. *Neuron* **26**, 345-356 (2000).
74. Funfak, A., Brösing, A., Brand, M. & Köhler, J.M. Micro fluid segment technique for screening and development studies on Danio rerio embryos. *Lab Chip* **7**, 1132 - 1138 (2007).
75. Zhang, Y., Lu, H. & Bargmann, C.I. Pathogenic bacteria induce aversive olfactory learning in Caenorhabditis elegans. *Nature* **438**, 179-184 (2005).
76. Gray, J.M. *et al.* Oxygen sensation and social feeding mediated by a C-elegans guanylate cyclase homologue. *Nature* **430**, 317-322 (2004).
77. Zeng, F., Rohde, C.B. & Yanik, M.F. Sub-cellular precision on-chip small-animal immobilization, multi-photon imaging and femtosecond-laser manipulation. *Lab on a Chip* **8**, 653-656 (2008).
78. Guo, S.X. *et al.* Femtosecond laser nanoaxotomy lab-on-achip for in vivo nerve regeneration studies. *Nat Methods* **5**, 531-533 (2008).
79. Chung, K.H., Crane, M.M. & Lu, H. Automated on-chip rapid microscopy, phenotyping and sorting of C. elegans. *Nat. Methods* **5**, 637-643 (2008).

80. Rohde, C.B., Zeng, F., Gonzalez-Rubio, R., Angel, M. & Yanik, M.F. Microfluidic system for on-chip high-throughput whole-animal sorting and screening at subcellular resolution. *PNAS* **104**, 13891-13895 (2007).
81. Hulme, S.E., Shevkoplyas, S.S., Apfeld, J., Fontana, W. & Whitesides, G.M. A microfabricated array of clamps for immobilizing and imaging C. elegans. *Lab on a Chip* **7**, 1515-1523 (2007).
82. Chronis, N., Zimmer, M. & Bargmann, C.I. Microfluidics for in vivo imaging of neuronal and behavioral activity in Caenorhabditis elegans. *Nat Methods* **4**, 727-731 (2007).
83. Heng, X. *et al.* Optofluidic microscopy - a method for implementing a high resolution optical microscope on a chip. *Lab on a Chip* **6**, 1274-1276 (2006).
84. Carrillo, F. *et al.* Nanoindentation of polydimethylsiloxane elastomers: Effect of crosslinking, work of adhesion, and fluid environment on elastic modulus. *Journal of Materials Research* **20**, 2820-2830 (2005).
85. Kim, D., Chesler, N.C. & Beebe, D.J. A method for dynamic system characterization using hydraulic series resistance. *Lab on a Chip* **6**, 639-644 (2006).
86. Jackman, R.J., Duffy, D.C., Cherniavskaya, O. & Whitesides, G.M. Using elastomeric membranes as dry resists and for dry lift-off. *Langmuir* **15**, 2973-2984 (1999).
87. Grill, B. *et al.* C. elegans RPM-1 Regulates Axon Termination and Synaptogenesis through the Rab GEF GLO-4 and the Rab GTPase GLO-1. *Neuron* **55**, 587-601 (2007).
88. Skelley, A.M., Kirak, O., Suh, H., Jaenisch, R. & Voldman, J. Microfluidic control of cell pairing and fusion. *Nat Methods* **6**, 147-152 (2009).
89. Di Carlo, D., Aghdam, N. & Lee, L.P. Single-cell enzyme concentrations, kinetics, and inhibition analysis using high-density hydrodynamic cell isolation arrays. *Analytical Chemistry* **78**, 4925-4930 (2006).
90. Chokshi, T.V., Ben-Yakar, A. & Chronis, N. CO2 and compressive immobilization of C. elegans on-chip. *Lab on a Chip* **9**, 151-157 (2009).
91. Crocker, J.C. & Grier, D.G. Methods of digital video microscopy for colloidal studies. *J. Colloid Interface Sci.* **179**, 298-310 (1996).
92. Hart, A.C., ed. Behavior. *WormBook, ed.* (2006).
93. Chung, K., Cho, J.K., Park, E.S., Breedveld, V. & Lu, H. Three-Dimensional in Situ Temperature Measurement in Microsystems Using Brownian Motion of Nanoparticles. *Analytical Chemistry* **81**, 991-999 (2009).
94. Cao, J., Hong, F.J. & Cheng, P. Numerical study of radial temperature gradient effect on separation efficiency in capillary electrophoresis. *International Communications in Heat and Mass Transfer* **34**, 1048-1055 (2007).
95. Ross, D. & Locascio, L.E. Microfluidic temperature gradient focusing. *Anal. Chem.* **74**, 2556-2564 (2002).
96. Rush, R.S., Cohen, A.S. & Karger, B.L. Influence of Column Temperature on the Electrophoretic Behavior of Myoglobin and Alpha-Lactalbumin in High-Performance Capillary Electrophoresis. *Anal. Chem.* **63**, 1346-1350 (1991).

97. Gobie, W.A. & Ivory, C.F. Thermal model of capillary electrophoresis and a method for counteracting thermal band broadening. *J. Chromatogr. A* **516**, 191-210 (1990).
98. Pearce, T.M., Wilson, J.A., Oakes, S.G., Chiu, S.Y. & Williams, J.C. Integrated microelectrode array and microfluidics for temperature clamp of sensory neurons in culture. *Lab on a Chip* **5**, 97-101 (2005).
99. Arata, H.F., Rondelez, Y., Noji, H. & Fujita, H. Temperature alternation by an on-chip microheater to reveal enzymatic activity of beta-galactosidase at high temperatures. *Anal. Chem.* **77**, 4810-4814 (2005).
100. Yamamoto, T., Nojima, T. & Fujii, T. PDMS-glass hybrid microreactor array with embedded temperature control device. Application to cell-free protein synthesis. *Lab on a Chip* **2**, 197-202 (2002).
101. Filevich, O. & Etchenique, R. 1D and 2D temperature imaging with a fluorescent ruthenium complex. *Anal. Chem.* **78**, 7499-7503 (2006).
102. Dowling, K., Hyde, S.C.W., Dainty, J.C., French, P.M.W. & Hares, J.D. 2-D fluorescence lifetime imaging using a time-gated image intensifier. *Optics Communications* **135**, 27-31 (1997).
103. Samy, R., Glawdel, T. & Ren, C.L. Method for Microfluidic Whole-Chip Temperature Measurement Using Thin-Film Poly(dimethylsiloxane)/Rhodamine B. *Anal. Chem.* **80**, 369-375 (2008).
104. Ross, D., Gaitan, M. & Locascio, L.E. Temperature measurement in microfluidic systems using a temperature-dependent fluorescent dye. *Anal. Chem.* **73**, 4117-4123 (2001).
105. Stasiek, J.A. & Kowalewski, T.A. Thermochromic liquid crystals applied for heat transfer research. *Opto-Electronics Review* **10**, 1-10 (2002).
106. Benninger, R.K.P. *et al.* Quantitative 3D mapping of fluidic temperatures within microchannel networks using fluorescence lifetime imaging. *Anal. Chem.* **78**, 2272-2278 (2006).
107. Jeon, S.M., Turner, J. & Granick, S. Noncontact temperature measurement in microliter-sized volumes using fluorescent-labeled DNA oligomers. *J. Am. Chem. Soc.* **125**, 9908-9909 (2003).
108. Hoang, V.N., Kaigala, G.V. & Backhouse, C.J. Dynamic temperature measurement in microfluidic devices using thermochromic liquid crystals. *Lab on a Chip* **8**, 484-487 (2008).
109. Ross, D. & Locascio, L.E. Effect of caged fluorescent dye on the electroosmotic mobility in microchannels. *Anal. Chem.* **75**, 1218-1220 (2003).
110. Sulabha Ranganathan, R.D.H. Effects of in vivo and in vitro exposure to rhodamine dyes on mitochondrial function of mouse embryos. *Teratog. Carcinog. Mutagen.* **9**, 29-37 (1989).
111. Kaji, T., Kawashima, T., Sakamoto, M., Kurashige, Y. & Koizumi, F. Inhibitory Effect of Rhodamine-B on the Proliferation of Human Lip Fibroblasts in Culture. *Toxicology* **68**, 11-20 (1991).
112. Pittman, J.L., Henry, C.S. & Gilman, S.D. Experimental studies of electroosmotic flow dynamics in microfabricated devices during current monitoring experiments. *Anal. Chem.* **75**, 361-370 (2003).

113. Seger, U., Panayiotou, M., Schnydrig, S., Jordan, M. & Renaud, P. Temperature measurements in microfluidic systems: Heat dissipation of negative dielectrophoresis barriers. *Electrophoresis* **26**, 2239-2246 (2005).
114. Dow corning. Sylgard 184 product data sheet.
115. Erickson, D., Sinton, D. & Li, D.Q. Joule heating and heat transfer in poly(dimethylsiloxane) microfluidic systems. *Lab on a Chip* **3**, 141-149 (2003).
116. Park, J.S., Choi, C.K. & Kihm, K.D. Temperature measurement for a nanoparticle suspension by detecting the Brownian motion using optical serial sectioning microscopy (OSSM). *Measurement Science & Technology* **16**, 1418-1429 (2005).
117. Hohreiter, V., Wereley, S.T., Olsen, M.G. & Chung, J.N. Cross-correlation analysis for temperature measurement. *Measurement Science & Technology* **13**, 1072-1078 (2002).
118. McDonald, J.C. & Whitesides, G.M. Poly(dimethylsiloxane) as a Material for Fabricating Microfluidic Devices. *Acc. Chem. Res.* **35**, 491-499 (2002).
119. Mao, H.B., Yang, T.L. & Cremer, P.S. A microfluidic device with a linear temperature gradient for parallel and combinatorial measurements. *J. Am. Chem. Soc.* **124**, 4432-4435 (2002).
120. Liepins, A. & Bustamante, J.O. CELL INJURY AND APOPTOSIS. *Scanning Microsc.* **8**, 631-643 (1994).
121. Davidson, J.F., Whyte, B., Bissinger, P.H. & Schiestl, R.H. Oxidative stress is involved in heat-induced cell death in Saccharomyces cerevisiae. *Proc. Natl. Acad. Sci. U. S. A.* **93**, 5116-5121 (1996).
122. Kubes, J., Svoboda, J., Rosina, J., Starec, M. & Fiserova, A. Immunological response in the mouse melanoma model after local hyperthermia. *Physiol. Res.* **57**, 459-465 (2008).
123. Zhu, J.K. Cell signaling under salt, water and cold stresses. *Curr. Opin. Plant Biol.* **4**, 401-406 (2001).
124. Sims, C.E. & Allbritton, N.L. Analysis of single mammalian cells on-chip. *Lab Chip* **7**, 423-440 (2007).
125. Matsunaga, T. *et al.* High-efficiency single-cell entrapment and fluorescence in situ hybridization analysis using a poly(dimethylsiloxane) microfluidic device integrated with a black poly(ethylene terephthalate) micromesh. *Anal Chem* **80**, 5139-5145 (2008).
126. Kleparnik, K. & Horky, M. Detection of DNA fragmentation in a single apoptotic cardiomyocyte by electrophoresis on a microfluidic device. *Electrophoresis* **24**, 3778-3783 (2003).
127. Crane, M.M., Chung, K. & Lu, H. Computer-enhanced high-throughput genetic screens of C. elegans in a microfluidic system. *Lab Chip* **9**, 38-40 (2009).
128. Shackman, J.G., Dahlgren, G.M., Peters, J.L. & Kennedy, R.T. Perfusion and chemical monitoring of living cells on a microfluidic chip. *Lab Chip* **5**, 56-63 (2005).
129. Lee, P.J., Gaige, T.A. & Hung, P.J. Dynamic cell culture: a microfluidic function generator for live cell microscopy. *Lab Chip* **9**, 164-166 (2009).
130. Abkarian, M., Faivre, M. & Stone, H.A. High-speed microfluidic differential manometer for cellular-scale hydrodynamics. *P Natl Acad Sci USA* **103**, 538-542 (2006).

131. Abkarian, M. *et al.* Cellular-scale hydrodynamics. *Biomedical Materials* **3** (2008).
132. Pal, R. *et al.* An integrated microfluidic device for influenza and other genetic analyses. *Lab Chip* **5**, 1024-1032 (2005).
133. Hibara, A. *et al.* Surface modification method of microchannels for gas-liquid two-phase flow in microchips. *Anal Chem* **77**, 943-947 (2005).
134. Hettiarachchi, K., Talu, E., Longo, M.L., Dayton, P.A. & Lee, A.P. On-chip generation of microbubbles as a practical technology for manufacturing contrast agents for ultrasonic imaging. *Lab Chip* **7**, 463-468 (2007).
135. Gunther, A. & Jensen, K.F. Multiphase microfluidics: from flow characteristics to chemical and materials synthesis. *Lab Chip* **6**, 1487-1503 (2006).
136. Garstecki, P. *et al.* Formation of monodisperse bubbles in a microfluidic flow-focusing device. *Appl Phys Lett* **85**, 2649-2651 (2004).
137. Srivastava, N. & Burns, M.A. Microfluidic pressure sensing using trapped air compression. *Lab Chip* **7**, 633-637 (2007).
138. Kuoni, A., Holzherr, R., Boillat, M. & de Rooij, N.F. Polyimide membrane with ZnO piezoelectric thin film pressure transducers as a differential pressure liquid flow sensor. *J Micromech Microeng* **13**, S103-S107 (2003).
139. Chang, W.Y., Chu, C.H. & Lin, Y.C. A flexible piezoelectric sensor for microfluidic applications using polyvinylidene fluoride. *IEEE Sensors Journal* **8**, 495-500 (2008).
140. Le, H.P., Shah, K., Singh, J. & Zayegh, A. Design and implementation of an optimised wireless pressure sensor for biomedical application. *Analog Integrated Circuits and Signal Processing* **48**, 21-31 (2006).
141. Kohl, M.J., Abdel-Khalik, S.I., Jeter, S.M. & Sadowski, D.L. A microfluidic experimental platform with internal pressure measurements. *Sensors and Actuators: A. Physical* **118**, 212-221 (2005).
142. Hosokawa, K., Hanada, K. & Maeda, R. A polydimethylsiloxane (PDMS) deformable diffraction grating for monitoring of local pressure in microfluidic devices. *J Micromech Microeng* **12**, 1-6 (2002).
143. Kartalov, E.P., Maltezos, G., Anderson, W.F., Taylor, C.R. & Scherer, A. Electrical microfluidic pressure gauge for elastomer microelectromechanical systems. *J Appl Phys* **102**, - (2007).
144. Kim, S.M., Burns, M.A. & Hasselbrink, E.F. Electrokinetic protein preconcentration using a simple glass/poly(dimethylsiloxane) microfluidic chip. *Analytical Chemistry* **78**, 4779-4785 (2006).
145. Yamada, M. & Seki, M. Microfluidic particle sorter employing flow splitting and recombining. *Anal Chem* **78**, 1357-1362 (2006).
146. Jeon, N.L. *et al.* Generation of solution and surface gradients using microfluidic systems. *Langmuir* **16**, 8311-8316 (2000).